NLO QCD corrections to tri-boson production in hadronic collisions

Zur Erlangung des akademischen Grades eines

DOKTORS DER NATURWISSENSCHAFTEN

von der Fakultät für Physik der Universität (TH)
Karlsruhe

genehmigte

DISSERTATION

von

Dipl. Phys. Vera Hankele
aus Stuttgart

Abstract

Multi-lepton signatures appear in many new physics searches at the CERN Large Hadron Collider LHC. In this thesis, WWZ as well as ZZW production with subsequent leptonic decay of the three vector bosons is considered as a Standard Model source of multi-lepton events. The next-to-leading order QCD corrections for the full $pp \rightarrow 6$ lepton production cross sections in hadronic collisions have been computed. Results are implemented in a fully flexible parton-level Monte Carlo program which allows to calculate the QCD corrections for arbitrary distributions and acceptance cuts. With K-factors as large as K = 2 at the LHC and a strong phase space dependence, these next-to-leading order calculations need to be taken into account for every phenomenological study involving the production of three weak bosons at the LHC.

Zusammenfassung

Bei der Suche nach neuer Physik mit dem großem Hadronen-Beschleuniger LHC am CERN, treten häufig Signaturen mit vielen Leptonen auf. In dieser Doktorarbeit, werden die WWZ sowie die ZZW Produktion mit anschließendem Zerfall der drei Eichbosonen in Leptonen als Mechanismen zur Produktion mehrerer Leptonen im Standard Model betrachtet. Der volle Wirkungsquerschnitt für die Produktion von sechs Leptonen in Hadron-Hadron Kollisionen inklusive der nächst-höheren Terme in der QCD Störungsreihe wurde berechnet. Die Ergebnisse sind in ein flexibles Monte Carlo Programm, das auf partonischen Reaktionen basiert, implementiert. Es erlaubt die Bestimmung von QCD Korrekturen für beliebige Verteilungen und Akzeptanz-Kriterien an die auslaufenden Teilchen. Am LHC können die K-Faktoren Werte im Bereich K = 2 annehmen. Überdies sind die QCD Korrekturen sehr stark vom betrachteten Phasenraum-Bereich abhängig. Deshalb sollten die Rechnungen der nächst-höheren Terme in der QCD Störungsreihe in allen phänomenologischen Studien für den LHC, die die Produktion von drei schwachen Eichbosonen beinhalten, berücksichtigt werden.

Contents

Chapter 1:

Introduction

Throughout the last decade, our understanding of the fundamental building blocks of the world surrounding us and the forces between them has constantly increased. This knowledge has been collected in the Standard Model of elementary particles (SM), which comprises Quantum Chromodynamics (QCD), describing the theory of strong interactions on the one hand, and the unified theory of electromagnetism and the weak force on the other hand. Thus, three of the fundamental forces known by now, the electromagnetic, the weak, and the strong force, are elaborated in a standardized form. So far, an analogous treatment of the fourth force, gravitation, has not been achieved. Therefore gravitation is not included in the SM. However, gravitational effects, being really important on astrophysical scales, are supposed to be tiny enough to safely neglect them in most calculations dealing with interactions of elementary particles.

Nonetheless, from a more rigorous point of view, a final theory describing nature, should, of course, contain gravitation. Moreover, experimental evidence for dark matter and dark energy also questions the reliability of the SM, since it does not offer a satisfactory explanation. These are just two examples for the limits of the Standard Model and the reasons for the general belief among physicists, that the SM is only a low energy effective theory, which describes physics within the reach of nowadays collider experiments very well, but will break down at higher energies. On the other side, experiments at various accelerators, such as the Large Electron Positron collider (LEP) located at CERN near Geneva, and the Tevatron proton-antiproton collider at Fermilab to just mention the most recent ones, have measured the properties of SM particles with an incredible accuracy and confirm SM predictions extraordinarily well. These experimental results laid the foundations of the success of the Standard Model albeit the known insufficiencies. Therefore, no matter how the underlying theory describing nature might look like, in the limit of low energies, it has to imitate the SM at least in some way.

The two opposing features of the Standard Model, being well tested but in any case not a valid theory up to arbitrary scales, can be translated into two goals for future

collider experiments. First, they have to measure with very high accuracy as many properties of particles and couplings predicted by the SM as possible in order to find even tiny deviations. Second, new theories, which have emerged over the years, have to be tested carefully.

The Large Hadron Collider (LHC) at CERN, slated to take data soon, provides from the experimental point of view an excellent tool to meet these demands. With center of mass energies as large as 14 TeV, physics beyond the SM, as for instance a supersymmetric extension, is probably in the reach of this proton-proton accelerator. Moreover, the last particle in the SM, which has not been experimentally confirmed yet, the Higgs boson, should, if it exists, be accessible.

The opportunity of penetrating so far unexplored territory of the SM or even beyond, can only be utilized, if theoretical predictions with the same accuracy as the experimental errors are available. In most of the cases, this requires at least calculations of the next-to-leading order terms in the QCD perturbation series. Since, at the LHC, one has to deal with various background processes, in part with cross sections larger than the actual signal cross section, also backgrounds have to be calculated with high accuracy. Furthermore, in order to account for geometrical specifications of the detectors or to isolate specific phase space regions, these calculations are handed to experimentalists preferably in the form of fully flexible Monte Carlo programs.

The importance of higher order calculations for the LHC is reflected in the wishlist, formulated at the Les Houches workshop in 2005 [1]. It contains the most important processes, for which next-to-leading order (NLO) QCD corrections were still needed at that time. In the meantime, most of them have been attacked or even been completely calculated [2–15]. Among the ones, which have been evaluated quite recently is the production of three vector bosons in proton-proton collisions, $pp \to \text{VVV} + \text{X}$. The results, which have originated in the course of this thesis are collected in Refs. [9, 14]. In addition, two other groups have presented results on this topic in Refs [5] and [11].

Triple vector boson production processes are of particular interest because they are sensitive to quartic electroweak couplings and they are a Standard Model background for many new-physics searches, characterized by several leptons in the final state. Concerning quartic couplings in the electroweak sector, some constraints have been derived from LEP data and are combined in Ref. [16]. Analogous measurements have been suggested for tri-boson production at hadron colliders [17–22]. However, proton-antiproton collisions at Tevatron center of mass energies of $\sqrt{s} = 1.96$ TeV yield very small production rates for three massive vector bosons in the final states. The LHC on the other hand, might have the potential to directly measure quartic

electroweak self-interactions in $pp \rightarrow \text{VVV} + \text{X}$ production, with three leptonically decaying vector bosons.

With K-factors ranging from 1.5 to 2 at the LHC and a strong phase space dependence, tri-boson production shows a behavior which is similar to that found in di-boson production in hadronic collisions, where QCD corrections have been known for a long time [23–30]. Thus, these NLO calculations need to be taken into account for every phenomenological study involving triple vector boson production processes at the LHC. However, since vector bosons are identified via their leptonic decay products, the calculations should include the leptonic decays. Furthermore, intermediate Higgs contributions are not negligible since they can enhance cross sections significantly and lead to dramatic changes in the shapes of distributions for certain observables.

In this thesis, the next-to-leading order QCD corrections to the three processes $pp \rightarrow \text{ZZW}^- + \text{X}$, $pp \rightarrow \text{ZZW}^+ + \text{X}$, and $pp \rightarrow \text{W}^+\text{W}^-\text{Z} + \text{X}$, with subsequent decay of the vector bosons into final-state leptons are computed. All spin correlations involved in vector boson decays as well as the effects due to intermediate Higgs boson exchange and off-shell contributions have correctly been taken into account. Two of the four processes, namely $pp \rightarrow \text{ZZW}^- + \text{X}$ and $pp \rightarrow \text{W}^+\text{W}^-\text{Z} + \text{X}$ have been computed for the first time in the course of this work. The third process $pp \rightarrow \text{ZZW}^+ + \text{X}$, has first been presented in Ref. [11], albeit without leptonic decays and without Higgs boson exchange contributions.

Results of the calculations have been implemented in a fully flexible parton-level Monte Carlo program VBFNLO [31]. The program allows for the computation of cross sections and distributions in either pp, $p\bar{p}$ or $\bar{p}\bar{p}$ collisions of arbitrary center of mass energies. However, in this thesis, we will restrict ourselves to proton-proton collisions, having LHC in mind.

The organization of the thesis is the following: Chapter 2 is devoted to an introduction into the particle content of the SM as well as some basics about perturbative QCD and hadronic collisions. The third chapter describes in detail the calculation of the different contributions to the leading order (LO) and NLO cross section. Chapter 4 contains the checks and comparisons performed. In Chapter 5 results are presented for triple boson production at the LHC. The renormalization- and factorization-scale dependence is discussed and further some sample distributions with strongly phase space dependent K-factors are shown. Finally, in the last chapter, the work presented here is summarized and discussed.

Chapter 2:

Basics

This chapter serves as an introduction into the theory of perturbative Quantum Chromodynamics and hadronic collisions. In the first section, the particle content of the Standard Model is introduced. Next, special features of QCD, the theory relevant for nucleon-nucleon interactions, is presented. The third section is devoted to the theoretical description of hadronic collisions involving the concept of factorization. In the last section of this chapter, next-to-leading order corrections in the QCD perturbation series and the divergencies arising thereby are treated. All of these topics are only discussed very briefly. A more detailed discussion of QCD and hadronic collisions can be found in various standard text books as for example Refs. [32–36].

2.1 The particle content of the standard model

During the last century almost all particles predicted by the Standard Model of elementary particle physics have been found and their properties have been measured with high accuracy. Thus, the SM is an extremely important and well tested theory for the description of elementary particles and their interactions. According to this $SU(3) \times SU(2) \times U(1)$ gauge theory, all matter is composed of two kinds of fermions. These fundamental spin-$\frac{1}{2}$ particles consist of leptons with the electron as the most prominent representative and quarks, which are the basic constituents of hadrons. Today, six different types of leptons and six different flavors of quarks are known. They fall into three different generations or families and each of them can be characterized by a special set of quantum numbers.

In the case of the leptons, every family consists of a charged lepton (e, μ, τ) and a neutrino (ν_e, ν_μ, ν_τ). In Table 2.1, all of these leptons are listed together with their conserved quantum numbers, electron number L_e, muon number L_μ, and tau number L_τ. In addition, electric charge, Q, and the central values of the masses of the charged leptons as well as upper limits on the neutrino masses are given.

lepton	L_e	L_μ	L_τ	Q	mass
ν_e	1	0	0	0	< 2 eV
e	1	0	0	-1	511.00 keV
ν_μ	0	1	0	0	< 0.19 MeV
μ	0	1	0	-1	105.66 MeV
ν_τ	0	0	1	0	< 18.2 MeV
τ	0	0	1	-1	1.7768 GeV

Table 2.1: *Leptons and their quantum numbers in the SM. The masses listed here are only central values according to Ref. [37]. For neutrinos only upper bounds exist.*

A complete overview on the properties of charged leptons and neutrinos, determined in experiment, is given in Ref. [37].

In the case of the quarks, every family consists of an up-type quark up (u), charm (c), or top (t) and a down-type quark down (d), strange (s), or bottom (b). Flavor quantum numbers are strong isospin (I, I_z), strangeness S, charm C, bottomness B, and topness T. These additive quantum numbers are preserved in all strong and electromagnetic interactions but can be violated in weak interactions. Moreover, all quarks carry baryon number $\mathcal{B} = \frac{1}{3}$, which is conserved in all interactions observed until now. The electric charge, Q, of quarks can be calculated using the generalized Gell-Mann-Nichijima formula,

$$Q = I_z + \frac{\mathcal{B} + S + C + B + T}{2}. \tag{2.1}$$

In Table 2.2, the additive quantum numbers, describing the various quarks, together with their electric charge, and the central value of their masses are summarized.

It is quite remarkable that in contrast to all other fundamental particles, up- and down-type quarks carry electric charge $+\frac{2}{3}$ and $-\frac{1}{3}$ of the charge of the electron, respectively. Furthermore, all quarks come in three colors, sometimes called, red, blue and green. "Real" particles measured in experiment, however, are colorless and have integer electric charge. The nucleons, neutrons and protons, for instance, are two representatives of baryons, which are three-quark bound states, whereas pions, being composed of a quark and an antiquark are examples for mesons. Together, baryons and mesons form the hadrons.

quark flavor	el. charge Q	isospin I	I_z	strangeness S	charm C	bottomness B	topness T	mass
u	$\frac{2}{3}$	$\frac{1}{2}$	$\frac{1}{2}$	0	0	0	0	2.55 MeV
d	$-\frac{1}{3}$	$\frac{1}{2}$	$-\frac{1}{2}$	0	0	0	0	5.04 MeV
c	$\frac{2}{3}$	0	0	0	+1	0	0	1.27 GeV
s	$-\frac{1}{3}$	0	0	-1	0	0	0	104 MeV
t	$\frac{2}{3}$	0	0	0	0	0	+1	172.4 GeV
b	$-\frac{1}{3}$	0	0	0	0	-1	0	4.68 GeV

Table 2.2: *Quarks and their quantum numbers in the SM. The masses given here, only give the central values according to Ref. [37] for up, down, charm, strange and bottom quarks. The most recent value for the top quark mass is taken from Ref. [38].*

Usually the quarks are defined as flavor or mass eigenstates of the strong force. Unfortunately, the electromagnetic and the weak interaction do not conserve the quantum numbers of the strong interaction, hence the eigenstates in the electroweak sector are different from the ones in the strong sector. This feature results in the so-called Cabibbo-Kobayashi-Maskawa (CKM) quark-mixing matrix $\mathbf{V}_{CKM}$ which gives the transformation between the mass eigenstates q and the eigenstates of the quarks with respect to the weak interaction q',

$$\begin{pmatrix} d' \\ s' \\ b' \end{pmatrix} = \begin{pmatrix} V_{ud} & V_{us} & V_{ub} \\ V_{cd} & V_{cs} & V_{cb} \\ V_{td} & V_{ts} & V_{tb} \end{pmatrix} \begin{pmatrix} d \\ s \\ b \end{pmatrix}. \tag{2.2}$$

For three different quark families, this unitary 3×3 matrix can be parameterized by three rotation angles and one phase. If the number of quark generations is restricted to two, the matrix is a 2×2 matrix and can be parameterized by the so-called Cabibbo-angle θ_C,

$$\mathbf{V}_C = \begin{pmatrix} \cos\theta_C & \sin\theta_C \\ -\sin\theta_C & \cos\theta_C \end{pmatrix}. \tag{2.3}$$

The entries of the CKM matrix appear in the Feynman rules and lead for instance in W-quark-couplings to the possibility of transitions of quarks from the first family to quarks of the second or third family.

Concerning the masses, there are four rather light quarks up, down, charm, and strange, often treated as massless particles and the quarks of the third family, top and bottom, which are quite heavy. In the calculation presented here, only the light quarks in the massless approximation are considered, which is a reasonable approximation. The relevant quark-mixing matrix thus is the Cabibbo matrix $\mathbf{V}_C$ given in Eq. (2.3). Some more details on this topic with respect to the specific processes computed in this thesis will be given in the next chapter.
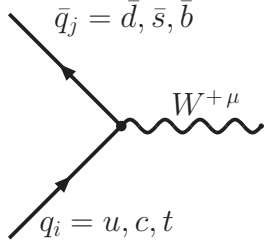
In addition to the particles mentioned until now, each of the quarks and leptons has its own antiparticle with the same mass but opposite quantum numbers.

The interactions between the fundamental fermions are dictated by three fundamental forces: the electromagnetic force, the weak force, which is responsible for radioactive beta-decay and the strong force, binding the protons inside the nucleus. In the Standard Model these forces are mediated via the exchange of vector bosons, which are particles of spin 1. The mediator in the case of the electromagnetic force is the massless photon, the gauge bosons for the strong force are the eight massless gluons and in the case of the weak interactions the mediators are the W^+-, W^-- and the Z-boson with masses,
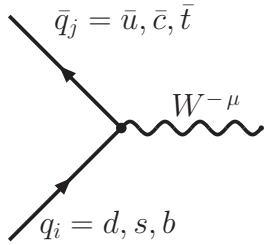
$$m_Z = 91.1876 \pm 0.0021 \text{ GeV}, \qquad m_W = 80.398 \pm 0.025 \text{ GeV}, \tag{2.4}$$

according to the latest analysis of the particle data group [37]. For each of these forces a charge exists and particles only interact strongly, weakly, or electromagnetically if they carry the corresponding charge.

Quarks, for example, carry the electromagnetic and the weak charge as well as color, the charge of the strong force. Thus, they couple to photons, W- and Z-bosons, and gluons. Specifically, the Feynman rules for the coupling of quarks to W-bosons are given by:

$$\bar{q}_j = \bar{d}, \bar{s}, \bar{b}$$

$$W^{+\mu}$$

$$q_i = u, c, t$$

$$= -\frac{i\,g}{\sqrt{2}}\,\gamma^\mu\,\frac{1}{2}\,(1 - \gamma^5)\,V_{q_i q_j}$$

$$\bar{q}_j = \bar{u}, \bar{c}, \bar{t}$$

$$W^{-\mu}$$

$$q_i = d, s, b$$
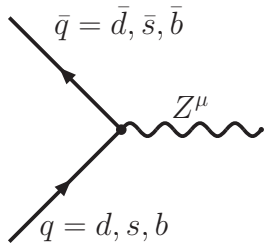
$$= -\frac{i\,g}{\sqrt{2}}\,\gamma^\mu\,\frac{1}{2}\,(1 - \gamma^5)\,V^*_{q_j q_i}$$

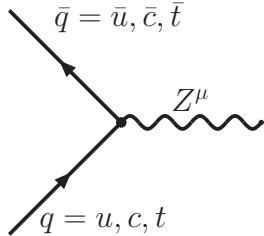Here, $V_{q_i q_j}$ and $V^*_{q_j q_i}$ are the (complex conjugated) CKM matrix elements as given in Eq. (2.2). They lead to transitions of quarks of one family to quarks of another family, as has been pointed out above.

In the case of the neutral Z-bosons on the other hand, the Feynman rules describing the interactions with the quarks are given by:

$$\bar{q} = \bar{u}, \bar{c}, \bar{t}$$

$$Z^\mu$$

$$q = u, c, t$$

$$= -\frac{i\,g\gamma^\mu}{\cos\theta_w}\left(\frac{1}{4} - \frac{2}{3}\sin^2\theta_w - \frac{1}{4}\gamma^5\right).$$

$$\bar{q} = \bar{d}, \bar{s}, \bar{b}$$

$$Z^\mu$$

$$q = d, s, b$$

$$= -\frac{i\,g\gamma^\mu}{\cos\theta_w}\left(-\frac{1}{4} + \frac{1}{3}\sin^2\theta_w + \frac{1}{4}\gamma^5\right).$$

In this case, charge conservation prohibits couplings between up- and down-type quarks. Furthermore, unitarity of the CKM-matrix then only allows interactions between quarks of the same flavor as for instance, $u\bar{u}Z$ and $d\bar{d}Z$ couplings.

In the bosonic sector, the photon is not charged, while gluons themselves carry the charge of the strong force. Therefore gluons couple to each other. This is one major difference between Quantum Electrodynamics (QED), the theory describing electromagnetic interactions and Quantum Chromodynamics, the gauge theory describing strong interactions between quarks and gluons.

In addition to the fermions and gauge bosons described above, another particle, called the Higgs boson, is predicted by the SM. This particle has been introduced into the theory in order to account for the masses of the heavy gauge bosons and of the fermions. However, up to now the existence of the Higgs boson has not been verified by experiment. Thus, its mass is still an unknown parameter of the theory.

2.2 QCD and asymptotic freedom

Quantum Chromodynamics is the non-abelian $SU(3)$ gauge theory describing the strong interactions of fundamental particles. The QCD Lagrangian is given by

$$\mathcal{L}_{QCD} = \sum_q \bar{q}_i (i\gamma^\mu D_\mu - m_q)_{ij} q_j - \frac{1}{4} F^a_{\mu\nu} F^{a\mu\nu} + \mathcal{L}_{ghost} + \mathcal{L}_{gauge-fix} \tag{2.5}$$

with the field strength tensor

$$F^a_{\mu\nu} = \partial_\mu A^a_\nu - \partial_\nu A^a_\mu - g_s f^{abc} A^b_\mu A^c_\nu \tag{2.6}$$

and the covariant derivative

$$(D_\mu)_{ij} = \delta_{ij} \partial_\mu + i g_s T^a_{ij} A^a_\mu. \tag{2.7}$$

Here g_s is the strong coupling constant, A^a_μ and q_i are the gluon and quarks fields, f^{abc} are the structure constants, T^a_{ij} are the generators of the Lie group which defines the gauge symmetry and m_q are the quark masses with $(m_q)_{ij} = m_q \delta_{ij}$. In the calculation presented here, the so-called Feynman-t'Hooft gauge has been chosen, i.e. the gauge-fixing term in the lagrangian is given by:

$$\mathcal{L}_{gauge-fix} = -\frac{1}{2}(\partial^\mu A_\mu^a)^2. \tag{2.8}$$

Being not relevant for the discussion given here, the ghost term $\mathcal{L}_{ghost}$ in Eq. (2.5) is not discussed any further. Readers interested in a complete description of QCD are referred to standard text books as for instance the book by Peskin and Schroeder [33]. In the QCD lagrangian, the first term contains the mass and kinetic terms of the quarks as well as the quark-gluon interactions. Here, the latter enters via the gluon fields in the covariant derivative D_μ given in Eq. (2.7). The second term in Eq. (2.5) describes the kinetic term of the gluons. Unlike QED, this term also leads to three-gluon and four-gluon self-interaction terms. These vertices are due to the last term in Eq. (2.6), which does not appear at all in QED. The reason for these self-interaction terms being of such fundamental importance is that they have a profound impact on the running of the strong coupling constant $\alpha_s(\mu)$ and lead to a completely different behavior compared to the running coupling constant in the electromagnetic theory.

In QED, the coupling constant at some characteristic scale Q^2 of the process under investigation is given by:

$$\alpha(Q^2) = \frac{\alpha(\mu^2)}{1 - \frac{\alpha(\mu^2)}{3\pi} \log\left(\frac{Q^2}{\mu^2}\right)}, \tag{2.9}$$

with $\alpha(\mu^2)$ being the value of the coupling constant at some reference scale μ^2, e.g. $\alpha(m_e^2) = \frac{e^2}{4\pi} \simeq (137.036)^{-1}$. In Eq. (2.9), vacuum polarization diagrams enter. These graphs lead to screening effects just as in the case of a charge in a dielectric medium. Thus, for large distances, the effective coupling is smaller and it grows for smaller distances becoming more and more the bare charge.

In the case of QCD not only the vacuum diagrams already appearing in QED, but also loop diagrams with gluon self vertices appear. An example for each of these loop diagrams is given in Fig. 2.1. Substituting the gluons in Fig. 2.1a by photons, this diagram looks exactly as the vacuum polarization diagrams in QED. The diagram in Fig. 2.1b in contrast, is one example for loop induced graphs, which only appear for gauge bosons with self interaction terms. These kind of graphs lead to an opposite sign in the determination of the running coupling constant at one
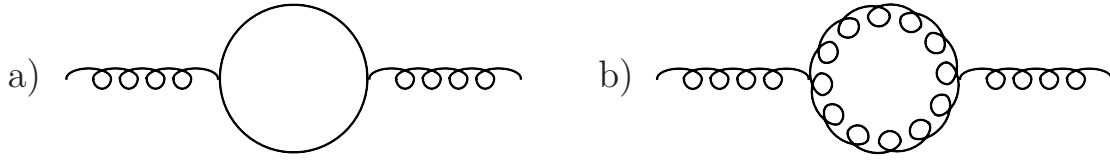
Figure 2.1: *Feynman graphs appearing in the one-loop calculation of the running coupling constant in QCD.*

specific scale compared to the diagrams with a fermion loop and therefore to anti-screening effects. In total, the effective strong coupling constant at one-loop is given by:

$$\alpha_s(Q^2) = \frac{g_s^2(Q^2)}{4\pi} = \frac{\alpha_s(\mu^2)}{1 + \frac{\alpha_s(\mu^2)}{12\pi}(33 - 2n_f)\ln(\frac{Q^2}{\mu^2})} \tag{2.10}$$

where Q^2 gives the scale of the momentum transfer, μ is the reference scale at which α_s is known and n_f is the number of quark flavors with masses less than the energy scale μ.

For $n_f < \frac{33}{2}$, which is certainly the case in QCD, the opposite behavior of QED is found. That means, for large values of Q^2, the effective coupling becomes small whereas for small momentum transfers, $\alpha_s(Q^2)$ becomes large. This property of $\alpha_S(Q^2) \to 0$ as $Q^2 \to \infty$ is known as asymptotic freedom and has been discovered by Gross, Wilczek and Politzer in 1973 [42,43]. It implies that in the regime of small-distance interactions quarks and gluons appear as almost free particles. Moreover, since in those cases the coupling is small, it is safe to use perturbative QCD.

On the other hand, for small momentum transfers the coupling becomes large, which is a property of QCD called confinement, and is the reason, why no isolated quarks or gluons can be observed. The scale where $\alpha_s(Q^2)$ becomes infinite is usually denoted by Λ_{QCD} and defined as

$$\Lambda_{QCD}^2 = \mu^2 \exp \frac{-12\pi}{(33 - 2n_f)\alpha_s(\mu^2)}. \tag{2.11}$$

This leads to the well known formula for the running coupling up to one-loop order,

12

$$\alpha_s(Q^2) = \frac{12\pi}{(33 - 2n_f) \ \ln(\frac{Q^2}{\Lambda_{QCD}^2})}. \tag{2.12}$$

In the calculations of NLO QCD corrections described in this thesis, the running coupling up to two-loop order is needed. The formula used in the code is given by:

$$\alpha_s(Q^2) = \frac{4\,\pi}{\beta_0 \ \ln\left(Q^2/\Lambda_{QCD}^2\right)} \left[1 - \frac{2\beta_1}{\beta_0^2} \ \frac{\ln\left[\ln(Q^2/\Lambda_{QCD}^2)\right]}{\ln\left(Q^2/\Lambda_{QCD}^2\right)} \right], \tag{2.13}$$

with $\beta_0 = 11 - \frac{2}{3}\,n_f$ and $\beta_1 = 51 - \frac{19}{3}\,n_f$.

The value of Λ_{QCD} has been measured in various experiments and is of the order of 200 MeV [39–41], which is then consistent with the size of a proton of about 1 fm.

2.3   Hadronic collisions

At hadron colliders as the LHC the scattering processes can be divided into soft and hard contributions. Soft processes, meaning processes with small momentum transfer, are dominated by non-perturbative QCD. These effects are not very well understood and can not be calculated by the usual approach with Feynman rules. For hard processes, the running coupling constant $\alpha_s(\mu)$ is small as explained in the previous section, and therefore perturbative QCD can be applied. Nonetheless, hadronic collisions are collisions between hadrons, perturbative QCD on the other hand deals with quarks and gluons. Therefore a description how to get valid predictions for hadronic collisions on the basis of the fundamental constituents, the partons, is needed.

In deep inelastic lepton-nucleon scattering, as pictured in Fig. 2.2, it was found that the nucleons were made of a collection of point-like constituents with almost no mass. These were identified as the quarks. Subsequently the so-called naïve parton model was formulated. In this model, the main idea is that for hard processes, the nucleon can be viewed as a loose collection of free partons and the total four-momentum of the nucleon P^μ, is shared between these partons. More specifically, a parton i inside the nucleon carries momentum $p_i^\mu = x_i\,P^\mu$ with probability density $f_{i/N}(x_i)$. Thus, the probability to find parton i with momentum fraction between x_i and $x_i + dx_i$
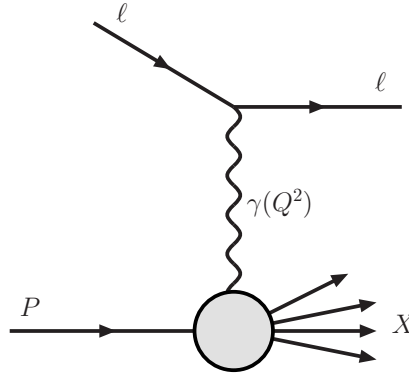
Figure 2.2: *Sketch of Feynman-graph for lepton-proton scattering, via the exchange of one virtual photon. X represents any number of unobserved final-state hadrons.*

inside the nucleon is given by $f_{i/N}(x_i)\, dx_i$. The total lepton-nucleon cross section can then be calculated by

$$\sigma = \sum_{i=q,\bar{q},g} \int_0^1 dx_i \; f_{i/N}(x_i)\; \hat{\sigma}_i. \tag{2.14}$$

That means, all partonic cross sections $\hat{\sigma}_i$ multiplied with the corresponding weight $f_{i/N}(x_i)$ and integrated over all possible momentum fractions are added up.

The partonic cross sections for the hard-scattering events can be calculated with the help of Feynman rules, the parton density functions (pdfs) on the other hand, include QCD of the non-perturbative regime and can not be calculated from first principles but need experimental input. However, the pdfs needed in the calculations are process-independent. Therefore, once measured in deep inelastic lepton-nucleon scattering experiments, they also give the probability to find parton i with momentum fraction x_i in any other interaction involving hadrons.

Thus, this naïve parton model can not only be used in the calculation of lepton-nucleon scattering, where it has been invented, but can also be applied to other processes with hadrons in the initial state. The fundamental principle allowing people to calculate arbitrary processes with this method is called factorization. It is the ability to factorize short-range QCD and long-range QCD from each other.

The strongest evidence for the sub-nuclear structure was the so-called scaling behavior, i.e. the fact that cross sections only depend on x, the momentum fraction
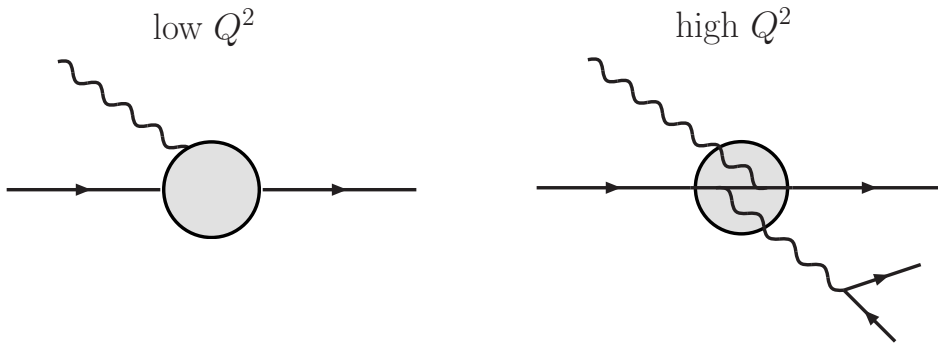
low Q^2 high Q^2

Figure 2.3: *Pictorial representation of vacuum fluctuations as they are resolved for low and high momentum transfer Q^2 according to Ref. [35].*

of the parton inside the nucleon actually struck by the intermediate gauge boson. This feature is directly related to scattering centers being point-like, dimensionless and non-interacting. However, improved measurements revealed that scaling is only approximately true. In general, with increasing energy, the point-like constituents inside the nucleon are not so point-like any more. Besides the expected constituents of the hadrons, so-called sea-quarks were found. Moreover, it was detected that the charged partons inside the hadron, i.e. the valence quarks and the sea-quarks together, only carry about one half of the total momentum of the nucleon. Thus, other neutral components, identified as the gluons, are also present inside the hadrons. These additional particles inside the nucleons are due to vacuum fluctuations, which simply cannot be resolved at low energies. At higher energies, on the other hand, more and more particles can be resolved and the average momentum fraction $\langle x \rangle$ of each parton is decreased. To illustrate these effects, pictures for both cases, with low and high momentum transfer are given in Fig. 2.3.

The experimental discovery of scaling violation hence made it necessary to introduce parton density functions (pdfs) $f_{p/N}(x_p; Q^2)$, which depend on the characteristic scale Q^2 of the process and thus the resolution. The Q^2-dependence of the pdfs is determined by the DGLAP evolution equations, named after Dokshitzer, Gribov and Lipatov and Altarelli and Parisi, who first derived them [44–46]. The phenomenological Q^2-dependent pdfs used nowadays have extracted the structure of these evolution equations and fitted free parameters in their approach by data, giving thereby reliable pdf-weights at almost arbitrary momentum fraction x and scale Q^2 for the partons.

However, the factorization of short- and long distance parts of the hadronic cross section is not unique. Although, the singular pieces have to be divided in a way, that the partonic cross section is infrared safe, i.e. no singular terms due to soft

and collinear partons are included and the pdfs contain all of the universal singular pieces which are left-over, the finite pieces can be shifted from one piece to the other. Therefore, a specific factorization scheme has to be chosen. Examples are the $\overline{\text{MS}}$ and the DIS scheme.

The renormalized pdfs including all divergencies, which do not cancel in the partonic cross sections, depend in these schemes on the momentum fraction of the parton x and a so-called factorization scale μ_F, which defines the point, where short-distance physics goes into long-distance QCD. This scale does not appear in the final results for the cross section if all orders of the perturbation series are taken into account. For a fixed-order calculation as described in this thesis, however, physical observables depend on the factorization scale. In principle, μ_F can be chosen arbitrarily, but if set to a characteristic scale of the process under investigation, higher-order effects are reduced.

The generalized cross section for the production of n partons in hadron-hadron interactions including these scheme dependent pdfs is then given by:

$$\sigma^n = \sum_{i,j,k_1,\ldots,k_n=q,\bar{q},g} \int dx_1 \; dx_2 \; f_{i/N}\left(x_1;\mu_F^2\right) f_{j/N}\left(x_2;\mu_F^2\right) \hat{\sigma}^{ij\to k_1,\ldots,k_n}. \tag{2.15}$$

Thus, the cross section is factorized into the parton density functions $f_{i/N}\left(x_1;\mu_F^2\right)$, $f_{j/N}\left(x_2;\mu_F^2\right)$ and the partonic cross section $\hat{\sigma}^{ij\to k_1,\ldots,k_n}$. The latter can be computed perturbatively up to a given order in α_s by evaluating matrix elements squared according to the Feynman rules, multiply them with the flux factor of the incoming partons and integrate over the whole phase space of the final-state particles,

$$
\begin{aligned}
\hat{\sigma}^{ij\to k_1,\ldots,k_n} = \int & \frac{1}{4\sqrt{(p_1\,p_2)^2 - M_1^2\,M_2^2}} \; |M(p_1 + p_2 \to k_1,\ldots,k_n)|^2 \\
& (2\,\pi)^4 \; \delta^{(4)}\!\left(p_1 + p_2 - \sum_{i=1}^{n} k_i\right) \frac{d^3\boldsymbol{k}_1}{(2\,\pi)^3\,2\,E_1} \cdots \frac{d^3\boldsymbol{k}_n}{(2\,\pi)^3\,2\,E_n}.
\end{aligned}
\tag{2.16}
$$

2.4 Next-to-leading order corrections in QCD

At hadron colliders, the LO cross section unfortunately only gives a rough estimate of the real cross section. The reasons are twofold. First, the unphysical factorization

scale (μ_F) in the parton distribution functions $f_{i/N}(x_i; \mu_F^2)$ and the renormalization scale dependence of $\alpha_S(\mu_R)$ appear in the final result. The physical cross section, on the other hand, is independent of the choice of these scales. Second, at NLO often new production modes appear, which are not allowed at LO. These can increase the cross section dramatically, but can also have a major impact on the shape of distributions. Thus NLO corrections are of special importance in this kind of calculations.

As has been pointed out in the previous section, the cross section consists of the process-independent parton distribution functions and a partonic part, which can be calculated perturbatively at high energies, i.e. order by order in the strong coupling constant $\alpha_s(\mu)$,

$$\hat{\sigma} = A_1 + A_2\,\alpha_s + A_3\,\alpha_s^2 + ... \tag{2.17}$$

The first term in this series, A_1, only appears in the calculation of purely electroweak processes, such as the Drell-Yan process $q\bar{q} \to \ell^+\ell^-$ and can be calculated from tree-level diagrams by applying the usual Feynman rules. In fact, concerning its QCD structure, triple vector boson production also can be regarded as a Drell-Yan type process. Thus, in the following discussion we will restrict ourselves to this type of processes.

The second term of the series in Eq. (2.17) comprises virtual contributions and real emission contributions. Loop diagrams as sketched in Fig. 2.4 give rise to the former. They interfere with the LO matrix elements resulting in contributions to the cross section of order α_s. The matrix elements squared of one-loop diagrams, however, are already of order α_s^2 and therefore do not contribute at NLO.

In the virtual contributions, two different types of divergencies arise. The so-called ultraviolet divergencies disappear upon renormalizations, i.e. by multiplying the bare masses and couplings by renormalization constants. The resulting renormalized masses and couplings are physical observables which are finite and can be measured in experiment. In actual calculations one common procedure is to add suitable counter terms to the Lagrangian which take care of these divergencies.

The infrared or soft divergencies on the other hand, are due to virtual massless particles in the loop integrals which become soft, i.e. with momentum $k^\mu \to 0$. These divergencies can not be renormalized, but their pole structure can be extracted by using for example the technique of dimensional regularization in $D = 4 - 2\epsilon$ dimensions.

The other type of diagrams contributing to the NLO cross section are real emission
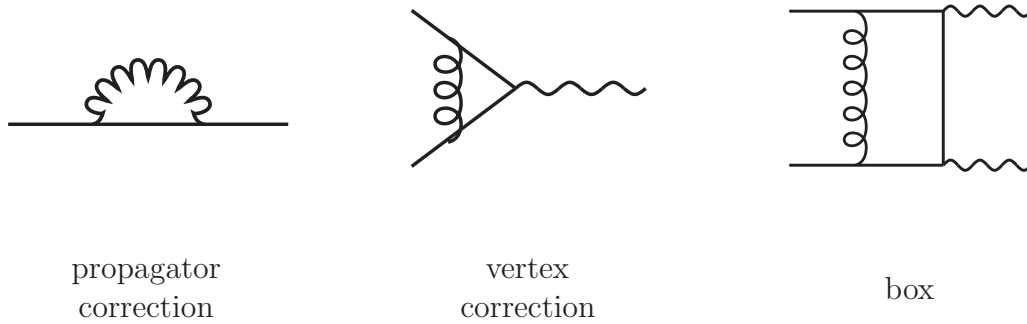
propagator
correction

vertex
correction

box

Figure 2.4: *Sample one-loop graphs with two external legs, three external legs and four external legs.*

gluon emission of an
external quark

gluon emission of an
internal quark

$g \to q\bar{q}$ splitting
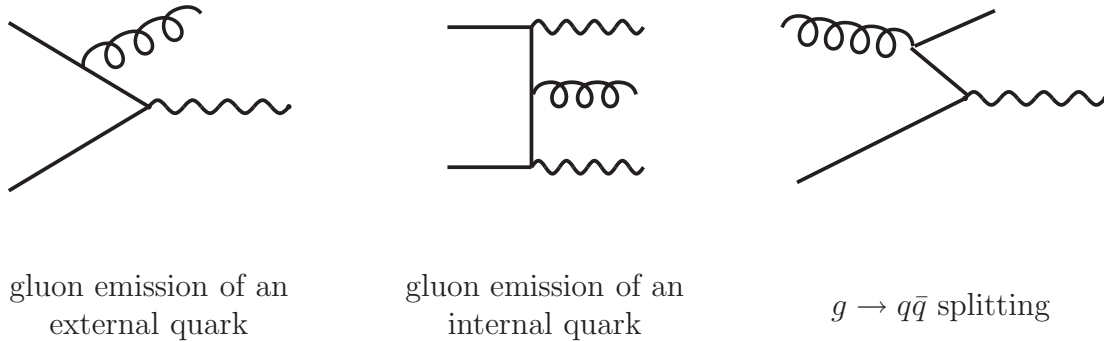
Figure 2.5: *Sample Feynman diagrams for the real emission contribution in a Drell-Yan type process such as $pp \to V$ or $pp \to VV$.*

graphs. They contain all diagrams with an additional parton in the final state. Here, gluon emission from an internal or external quark line as well as $g \to q\bar{q}$ splitting is possible in the case of Drell-Yan type processes. Both types are illustrated in Fig. 2.5.

In the case of the real emission, infrared divergencies arise for soft gluons, $p_g \to 0$ and collinear divergencies come from $q \to qg$ and $g \to q\bar{q}$ splittings, if the angle between the outgoing parton and the initial-state parton becomes too small.

Adding up all contributions to the partonic cross section at NLO, only initial-state collinear divergencies are left, whereas the soft divergencies cancel between the real emission and the virtual contributions. However, these collinear divergencies are identical to those found in the computations of NLO corrections to deep-inelastic

lepton-nucleon scattering. They can thus be absorbed into the pdfs resulting in renormalized pdfs. That means, the parton distribution functions are process-independent at NLO, in the sense, that the structure of divergencies is unique for any NLO calculation. In fact, the factorization theorem even states that collinear singularities can be absorbed into the pdfs at every order in perturbation theory. The finite remainders of this factorization of collinear singularities into the parton distribution functions depend on the factorization scheme and differ from process to process.

Therefore, the total NLO cross section is given by:

$$\sigma^{NLO} = \sigma^{LO} + \sigma^{VIRT} + \sigma^{REAL} + \sigma^{COLL}. \tag{2.18}$$

Only the LO contribution σ^{LO} and the collinear remainder after factorization of collinear singularities into the parton distribution functions σ^{COLL}, are finite in this formula. The other two contributions are separately infrared divergent. Since in the real emission calculation an additional parton in the final state appears, this part of the total NLO cross section involves an integration over an (m+1)-particle phase space whereas all other parts only need to be integrated over an m-particle phase space. The obvious difficulties in performing these integrations numerically in spite of the divergencies appearing thereby, have been overcome in this thesis by applying the Catani-Seymour dipole subtraction formalism [47,48]. A detailed description of this method will be given in the next chapter as well as in Appendix A.

Chapter 3:

Elements of the calculation

In this chapter the calculation of the NLO QCD corrections for ZZW^+, ZZW^-, and W^+W^-Z production at hadron colliders will be presented in detail.

The first section of this chapter covers the calculation and implementation at tree-level as well as an error estimate of the assumed approximations. In detail, the calculated matrix elements are given, and it is discussed, which contributions can be neglected. Moreover, a feature of our implementation in the Fortran program VBFNLO is explained, which speeds up the program dramatically.

In the second section the calculation at next-to-leading order in the QCD perturbation series, that is up to order α_s, is outlined. At first, the formalism of Catani and Seymour is presented [47, 48]. Subsequently, some details on the evaluation of the real emission terms as well as the finite collinear terms are given. The last two paragraphs deal with the different contributions to the virtual corrections in general and with various aspects of the implementation of the pentagon contribution.

3.1 Tree-level contributions

For each of the different final states,

$$W^+W^-Z: \quad pp \to \nu_{\ell_1}\, \ell_1^+\, \ell_2^-\, \bar{\nu}_{\ell_2}\, \ell_3^-\, \ell_3^+ + X, \tag{3.1}$$

$$ZZW^+: \quad pp \to \ell_1^-\, \ell_1^+\, \ell_2^-\, \ell_2^+\, \nu_{\ell_3}\, \ell_3^+ + X, \tag{3.2}$$

$$ZZW^-: \quad pp \to \ell_1^-\, \ell_1^+\, \ell_2^-\, \ell_2^+\, \ell_3^-\, \bar{\nu}_{\ell_3} + X, \tag{3.3}$$

the full set of Feynman graphs up to order $(\alpha_s^0)\,\alpha^6$ has been considered in the calculation. This includes the Higgs contribution and all off-shell diagrams. Details on the calculation and implementation of partonic cross sections are given in the first part of this section.

In order to simplify the computations and to improve the performance of the numerical implementation, a number of approximations and assumptions have been made. First, interference terms due to identical particles in the final state have not been taken into account. In addition, any fermion mass effects are neglected. Furthermore the CKM matrix is approximated by a unit matrix. A discussion to what extent these assumptions are justified and some estimates on the resulting errors on the total cross section are given in the second part of this section.

3.1.1 Calculation and implementation

The partonic cross section at LO can be split into four different types of subprocesses in the case of W^+W^-Z production and into two different classes of subprocesses in the case of ZZW^+ and ZZW^- production. In the W^+W^-Z case they are specifically,

$$
\begin{aligned}
u\bar{u} &\to \nu_{\ell_1}\, \ell_1^+\; \ell_2^-\, \bar{\nu}_{\ell_2}\; \ell_3^-\, \ell_3^+, \\
\bar{u}u &\to \nu_{\ell_1}\, \ell_1^+\; \ell_2^-\, \bar{\nu}_{\ell_2}\; \ell_3^-\, \ell_3^+, \\
d\bar{d} &\to \nu_{\ell_1}\, \ell_1^+\; \ell_2^-\, \bar{\nu}_{\ell_2}\; \ell_3^-\, \ell_3^+, \\
\bar{d}d &\to \nu_{\ell_1}\, \ell_1^+\; \ell_2^-\, \bar{\nu}_{\ell_2}\; \ell_3^-\, \ell_3^+,
\end{aligned}
\tag{3.4}
$$

where u stands for an up-type quark and d for a down-type quark. In the calculation they can be up or charm and down or strange, respectively. The matrix elements for the $\bar{q}q$ - initiated contributions are obtained in the program from the $q\bar{q}$ - initiated processes by a simple crossing, i.e., they are calculated with the same subroutine but with the momenta of the initial-state partons interchanged.

The same is true for the two subprocesses for the ZZW^+ production,

$$
\begin{aligned}
u\bar{d} &\to \ell_1^-\, \ell_1^+\; \ell_2^-\, \ell_2^+\; \nu_{\ell_3}\, \ell_3^+, \\
\bar{d}u &\to \ell_1^-\, \ell_1^+\; \ell_2^-\, \ell_2^+\; \nu_{\ell_3}\, \ell_3^+,
\end{aligned}
\tag{3.5}
$$

and the ones for the ZZW^- production,

$$
\begin{aligned}
d\bar{u} &\to \ell_1^-\, \ell_1^+\; \ell_2^-\, \ell_2^+\; \ell_3^-\, \bar{\nu}_{\ell_3}, \\
\bar{u}d &\to \ell_1^-\, \ell_1^+\; \ell_2^-\, \ell_2^+\; \ell_3^-\, \bar{\nu}_{\ell_3}.
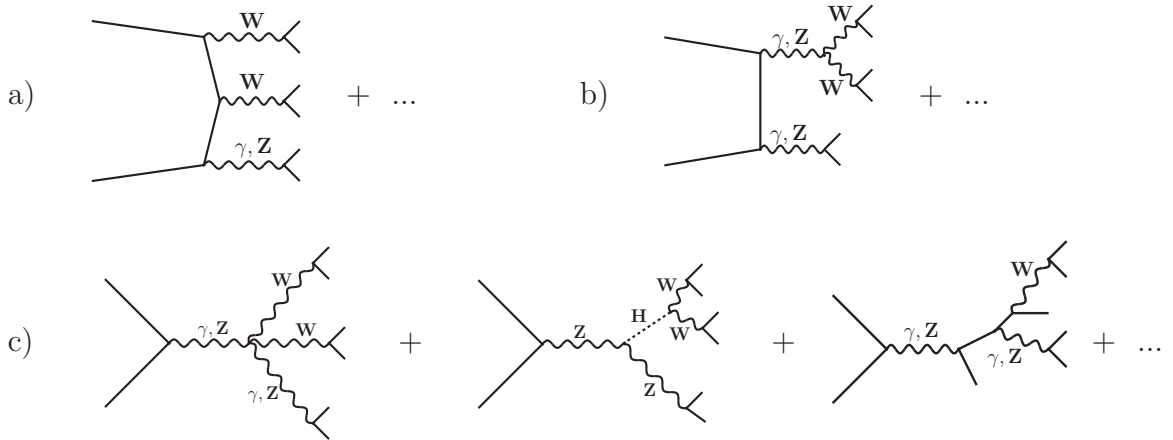\end{aligned}
\tag{3.6}
$$

Figure 3.1: *Some representative tree-level Feynman diagrams of the process* $pp \to 4\,\ell + 2\,\nu$. *They show the three different topologies appearing in this calculation.*

Here, different quark flavors are required in the initial state. Again, u stands for an up-type quark, whereas d refers to a down-type quark.

In total there are 209 diagrams for each subprocess of ZZW production and 180 diagrams for each subprocess of WWZ production. Because of the large number of Feynman diagrams the helicity method of Refs. [49,50] is used for the evaluation of matrix elements. However, for each of the subprocesses in the various triple vector boson production processes, the general structure of the matrix elements is the same.

For all processes the tree-level graphs can be grouped into three distinct topologies. These topologies give rise to different one-loop contributions, as discussed later in this chapter. Moreover, the topologies are also used to optimize the calculation of matrix elements by extracting leptonic tensors which appear several times in the evaluation of matrix elements. Some sample diagrams for the three topologies are given in Fig. 3.1 for the case of the W^+W^-Z production. As indicated by the labels, virtual Z-bosons as well as photons are taken into account. Both of them are assumed to decay leptonically, $V \to \ell^+\ell^-$, thus leading to the same final state with two charged leptons.

In the calculation of leptonic tensors, special care has to be taken in the treatment of finite-width effects in massive vector boson propagators. In the code, the modified complex-mass scheme as implemented in MADGRAPH is used, that is m_V^2 is globally replaced with $m_V^2 - i\,m_V\Gamma_V$, while a real value is kept for $\sin^2\theta_W$ [51–53].

In Fig. 3.1a three vector bosons with subsequent decay are emitted from the quark line. In order to account for the decay of these vector bosons, the polarization vectors $\epsilon^\mu_{W^+}(p_{W^+})$, $\epsilon^\nu_{W^-}(p_{W^-})$, and $\epsilon^\rho_Z(p_Z)$ are replaced by leptonic tensors $\Gamma^\mu_{W^+}$, $\Gamma^\nu_{W^-}$, and Γ^ρ_Z. These are the effective decay currents together with a propagator factor for the intermediate vector boson. The decay $W^+ \to \nu_e\, e^+$ together with the propagator factor $\frac{1}{p^2_{W^+} - m^2_W + i m_W \Gamma}$, for instance, is then given by the leptonic tensor $\Gamma^\mu_{W^+}$. The effective polarization vectors for the decay of the vector bosons into two leptons appear in many different Feynman graphs. In order to speed up the calculation, they are determined numerically at the beginning of the evaluation of the matrix elements for a given phase space point and reused wherever they appear.

In Fig. 3.1b two vector bosons are attached to a quark line and then decay into two or four leptons. All Feynman graphs for a four-lepton decay can again be combined to an effective polarization vector. For all subprocesses such as $u\bar{d} \to 5\,\ell + \nu$, $d\bar{u} \to 5\,\ell + \nu$ for ZZW and $u\bar{u} \to 4\,\ell + 2\,\nu$, $\bar{d}d \to 4\,\ell + 2\,\nu$ for WWZ, these polarization vectors are identical for one specific phase space point and do not depend on the quark polarization. Furthermore, they appear in several Feynman diagrams. In our code these polarization vectors are therefore calculated once per phase space point, stored and reused wherever possible.

The last topology is the one in which only one vector boson is attached to the quark line. The polarization vector corresponding to the "decay" of this virtual vector boson can be calculated once per phase space point, stored and reused. The method of precalculating effective polarization vectors renders our code for the WWZ Born process about four times faster and our code for the ZZW Born processes about two times faster than a direct evaluation with MADGRAPH [51–53].

An additional increase in speed has been achieved by performing the helicity summation for the final-state leptons stemming from the Z-bosons and photons randomly. In detail, for every phase space point one helicity configuration of the final-state leptons is selected. Since only left-handed leptons couple to W-bosons, this selection only affects the Z-bosons and the virtual photons. The matrix element squared for this special configuration of helicities is subsequently calculated and multiplied by the number of actual helicity configurations, i.e. by a factor of two in the WWZ case and by a factor of four in the ZZW case. For the next phase space point one of the other helicity configurations is selected and the matrix element is computed. This procedure is then repeated for all the phase space points. Thus, only the matrix elements of one helicity configuration have to be calculated per phase space point.

3.1.2 Assumptions and approximations

In the calculation of LO cross sections as described in the previous paragraph, interference terms due to identical particles in the final state have been neglected. Including such effects at LO in the calculation of the W^+W^-Z production, it can be confirmed, that this is an excellent approximation: LO cross sections change by less than 0.1% when interference terms are integrated over the Breit-Wigner peaks. This small effect is due to modest cancellations between contributions below and above the Breit Wigner peaks. However, even the integration over the absolute values of the interference terms yields contributions at the few percent level only, which is below the scale variation of the final NLO cross sections.

An estimate on the validity of results when neglecting any effects of fermion masses in the calculations is more involved. In the leptonic sector, the heaviest leptons are the tau leptons. However, at LO cross sections with zero tau mass and with $m_\tau = 1.7768$ GeV have been computed with Helac [54–56] and only deviations of the order of 1% have been found. The leptons of the third family can then safely be neglected in the calculation. Thus, we are left with the almost massless leptons of the first two families only. In particular, this assumption implies that all graphs with Higgs Yukawa couplings to leptons can be set to zero.

In the quark sector, we have to deal with four almost massless quarks (u, d, c, s) and the quarks of the third family, top and bottom. Since the possibility to find a top quark inside a proton is virtually zero, the contribution of top quarks in the initial state can safely be neglected. Moreover, in the case of ZZW production always one W-boson couples to the quark line. Thus, the flavor changes once along the quark line. Since the CKM matrix element giving the transition probability from bottom quarks to top quarks and vice versa

$$V_{tb} = 0.999133\,^{+0.000044}_{-0.000043}, \tag{3.7}$$

is close to one [37], a bottom quark in the initial state would thus be accompanied by a top quark in the initial state. Therefore, for this type of processes, the exclusion of the latter also excludes bottom quarks in the initial state.

In the WWZ production, either two or zero W-bosons are attached to the quark line. Hence, the quark flavor changes either twice along the quark line or not at all. Taking into account that bottom quarks, with a very high degree of probability transfer to top quarks and vice versa, mixing of quarks of the third family with
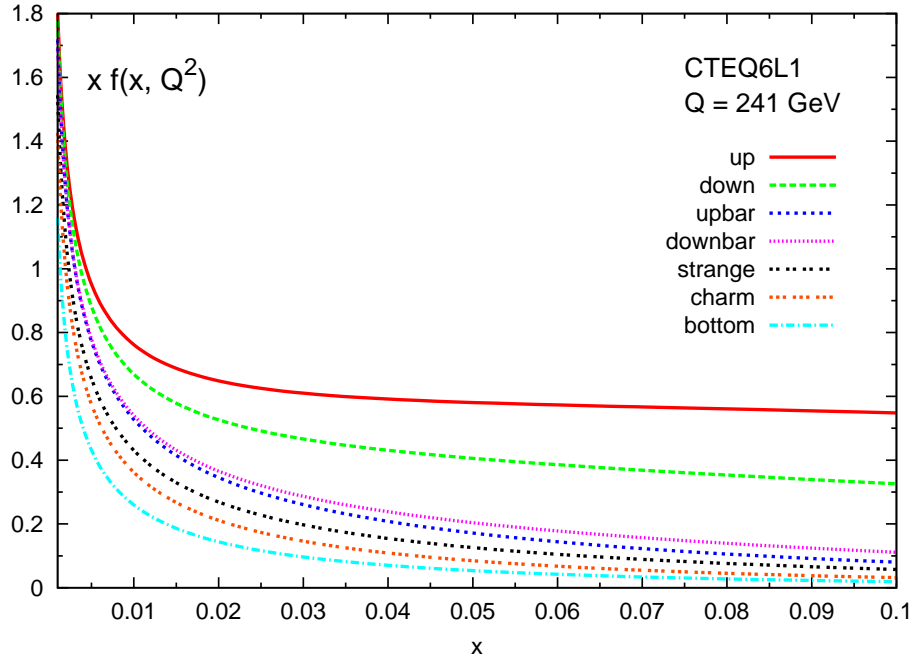
Figure 3.2: *Typical values for the LO parton distribution functions needed in the tri-boson production at the LHC.*

quarks of the other two families are very rare. Thus, either both initial-state quarks are assumed to be bottom quarks or none of them. However, the corresponding bottom quark pdf weights are suppressed compared to the other sea quark pdfs. For instance, for a typical Feynman-x value in tri-boson processes of $x = 0.03$, the probability to find a b quark inside a proton is suppressed by a factor two to four compared to the other sea quarks as shown in Fig. 3.2 for the CTEQ6L1 pdf set. Therefore, the heavy quarks of the third family can be neglected in the initial state, and because they usually do not couple to the quarks of the other two families, they can also be neglected in the intermediate states. In total that leaves us with the four light quarks of the first two families with negligible masses.

The impact on the cross section by setting the CKM matrix to the unit matrix needs to be considered separately for the WWZ and ZZW cases. Since only up, down, charm, and strange quarks are taken into account, the CKM matrix is reduced to the Cabibbo matrix $\mathbf{V}_C$ given in Eq. (2.3).

In the WWZ production mode, the two topologies depicted in Figs. 3.1b and 3.1c are independent of the CKM matrix since they do not contain a W-quark coupling. For the topology, where two W-bosons couple to the quark line on the other hand,
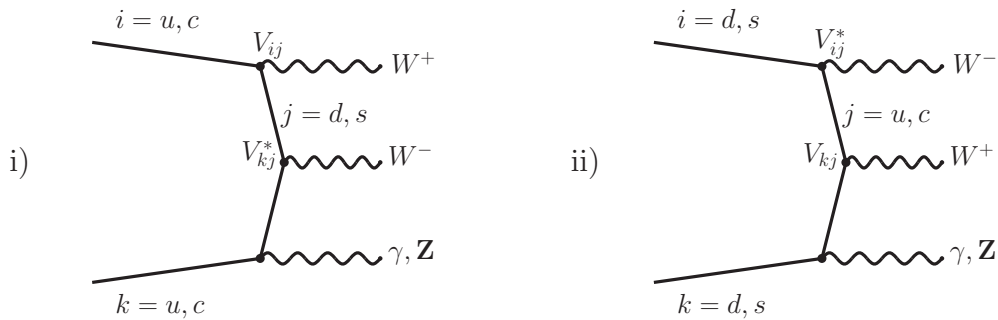
Figure 3.3: *Sketch of the flavors in W^+W^-Z production.*

one needs to argue differently. This case is sketched in Fig. 3.3 for i) up-type quarks in the initial state and ii) down-type quarks in the initial state. The labels i, j, and k in this figure are labeling the different quark flavors and at the W-quark vertices the two W-bosons couple to the quark line yielding matrix elements proportional to $V_{ij}V_{kj}^*$, where V_{ij} and V_{kj}^* are CKM matrix elements. The labels i and k denote the quark flavors of the initial-state quarks, whereas j stands for the flavor of the intermediate quark. Since all flavors can appear in the intermediate state, one has to sum over j. Taking into account unitarity of the quark mixing matrix, one obtains in the approximation of massless quarks:

$$\sum_j V_{ij}V_{kj}^* = \delta_{ik}. \tag{3.8}$$

Therefore, for massless quarks, the flavor of initial- and final-state quarks is always the same in the WWZ production and effects of the CKM matrix vanish at LO. Including mass effects would lead to an additional contribution $m_{ik}(j)$ in Eq. (3.8). In the case of the ZZW production, approximating the CKM matrix by a unit matrix leads to an error on the cross section, which will be estimated in the following. In each of the different topologies depicted in Fig. 3.4 exactly one W-boson couples to the quark line. Therefore, the transition matrix elements are proportional to the CKM matrix element V_{ij} entering via the coupling of initial-state quark i and initial-state quark j to the W-boson. Bearing in mind that the calculation of the matrix elements does not depend on the quark flavors except for this factorizable CKM matrix element, on obtains for the matrix elements convoluted with the pdfs:
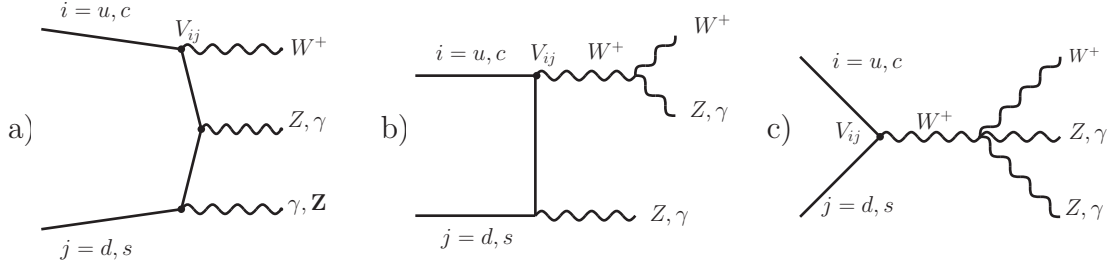
Figure 3.4: *Sketch of the quark flavors in the different topologies of ZZW^+ production.*

$$|\mathcal{M}(q\,(p_a) + \bar{Q}\,(p_b) \rightarrow \mathrm{ZZW})|^2 \times \mathrm{PDFs}$$

$$= |M_{Born}|^2 \cdot \Big[\ |V_{ud}|^2 \ f_{u/p}\,(x_a) \ f_{\bar{d}/p}\,(x_b) + |V_{us}|^2 \ f_{u/p}\,(x_a) \ f_{\bar{s}/p}\,(x_b)$$

$$+ |V_{cs}|^2 \ f_{c/p}\,(x_a) \ f_{\bar{s}/p}\,(x_b) + |V_{cd}|^2 \ f_{c/p}\,(x_a) \ f_{\bar{d}/p}\,(x_b) \ \Big]$$

$$= |M_{Born}|^2 \cdot \Big[\ \cos^2\theta_C \ f_{u/p}\,(x_a) \ f_{\bar{d}/p}\,(x_b) + \sin^2\theta_C \ f_{u/p}\,(x_a) \ f_{\bar{s}/p}\,(x_b)$$

$$+ \cos^2\theta_C \ f_{c/p}\,(x_a) \ f_{\bar{s}/p}\,(x_b) + \sin^2\theta_C \ f_{c/p}\,(x_a) \ f_{\bar{d}/p}\,(x_b) \ \Big]$$

$$= |M_{Born}|^2 \cdot \Big[\ \Big(1 + \sin^2\theta_C \ \Big(\frac{f_{\bar{s}/p}\,(x_b)}{f_{\bar{d}/p}\,(x_b)} - 1 \Big) \Big) f_{u/p}\,(x_a) \ f_{\bar{d}/p}\,(x_b) \quad\quad (3.9)$$

$$+ \Big(1 + \sin^2\theta_C \ \Big(\frac{f_{\bar{d}/p}\,(x_b)}{f_{\bar{s}/p}\,(x_b)} - 1 \Big) \Big) f_{c/p}\,(x_a) \ f_{\bar{s}/p}\,(x_b) \ \Big]$$

$$= |M_{Born}|^2 \cdot \Big[\ f_{u/p}\,(x_a) \ f_{\bar{d}/p}\,(x_b) + f_{c/p}\,(x_a) \ f_{\bar{s}/p}\,(x_b)$$

$$+ f_{u/p}\,(x_a) \ f_{\bar{d}/p}\,(x_b) \ \sin^2\theta_C$$

$$\cdot \Big(1 - \frac{f_{c/p}\,(x_a)}{f_{u/p}\,(x_a)} \Big) \Big(\frac{f_{\bar{s}/p}\,(x_b)}{f_{\bar{d}/p}\,(x_b)} - 1 \Big) \ \Big].$$

Measurements of V_{uc} and hence the Cabibbo angle appearing in this formula yield $|V_{ud}| = |\cos\theta_C| = 0.97419 \pm 0.00022$, according to Ref. [37]. The ratios of the pdfs depend on the momentum fraction of the incoming partons and the factorization scale. Setting the former to $x = 0.03$ and choosing the latter as $Q^2 = (3\,m_W)^2$, the neglected terms for this special set of values are:

$$\underbrace{\sin^2 \theta_C}_{\simeq\, 0.05} \cdot \underbrace{\left(1 - \frac{f_{c/p}\,(x_a)}{f_{u/p}\,(x_a)} \right)}_{\simeq\, 0.83} \cdot \underbrace{\left(\frac{f_{\bar{s}/p}\,(x_b)}{f_{\bar{d}/p}\,(x_b)} - 1 \right)}_{\simeq\, -0.31} \cdot \sigma^{LO}\,(u\bar{d} \to \text{ZZW})$$

$$\simeq -0.013 \cdot \sigma^{LO}\,(u\bar{d} \to \text{ZZW}). \tag{3.10}$$

In total, the error on the total LO cross section for the ZZW production at the LHC induced by setting the CKM matrix to the unit matrix is anticipated to be of the order of 1-2 percent. However, an explicit test of this expectation with HELAC [54–56] demonstrates that for the specific set of input variables chosen, the error for the ZZW$^+$ production is about 2%. As will be shown in Chapter 5, this effect is thus slightly below the size of the uncertainties on the pdfs and well below the scale uncertainty of the NLO cross section.

3.2 Next-to-leading order contributions

The full NLO cross section for hadronic collisions consists of real emission contributions, virtual contributions and a finite collinear remnant, after the initial-state collinear singularities are absorbed into the parton distribution functions. The real emission contributions have to be integrated over an (m+1)-particle phase space with m = 6 leptons, and the other two contributions only involve an m-particle phase space,

$$\sigma^{NLO} = \int d\sigma^{NLO} = \int_{m+1} d\sigma^R + \int_m d\sigma^V + \int_m d\sigma^C. \tag{3.11}$$

The real emission contribution $\int_{m+1} d\sigma^R$ and the virtual contributions $\int_m d\sigma^V$ are separately infrared divergent in $D = 4$ dimensions and only their sum gives a well defined finite result. Since in a numerical calculation it is impossible to calculate these divergent pieces separately, another solution is needed to overcome this problem. The finite collinear term $\int_m d\sigma^C$ on the other hand, can be evaluated directly in $D = 4$ dimensions.

3.2.1 Catani-Seymour dipole subtraction

One common method to overcome the problem with divergencies in real emission and virtual contributions is to regularize the divergencies using dimensional reduction

$(D = 4 - 2\epsilon)$, and apply the dipole subtraction algorithm proposed by Catani and Seymour [47, 48]. In this algorithm, terms $d\sigma^A$, which match the singular behavior of $d\sigma^R$, are introduced. This means that the difference of these two terms can be integrated numerically in four dimensions over the whole phase space. In order to leave the total result unchanged, the additional subtraction terms have to be added again and need to be integrated together with the virtual contributions.

However, the virtual contributions only have to be integrated over an m-particle phase space, whereas the counter terms have to be integrated over an (m+1)-particle phase space. Thus, first the integration over the one-particle phase space $\int_1 d\sigma^A$ is carried out and the poles are extracted. These can be canceled analytically against the poles from the virtual contributions. Finally, the finite result can be integrated numerically.

The still missing contribution to the next-to-leading order cross section comes from the absorption of collinear singularities into the pdfs. Since it is a finite remainder by definition, it can be integrated in four dimensions without any alteration and in total we get:

$$\sigma^{NLO} = \underbrace{\int_{m+1} \left[\left(d\sigma^R \right)_{\epsilon=0} - \left(d\sigma^A \right)_{\epsilon=0} \right]}_{\substack{\text{Can be integrated} \\ \text{numerically in 4} \\ \text{dimensions}}} + \underbrace{\int_m \left[d\sigma^V + \int_1 d\sigma^A \right]_{\epsilon=0}}_{\substack{\text{Poles are} \\ \text{canceled} \\ \text{analytically}}} + \underbrace{\int_m d\sigma^C}_{\substack{\text{Finite} \\ \text{collinear} \\ \text{remainder}}}.$$

The general formulas for $d\sigma^A$, $\int_1 d\sigma^A$ and $d\sigma^C$ given in Ref. [47, 48] have been evaluated for the special case of triple vector boson production in hadronic collisions, $pp \rightarrow \text{VVV} + \text{X}$. Expressions for the dipoles, integrated dipoles and the finite collinear terms are given explicitly in the following paragraphs and in Appendix A.

3.2.2 Real emission

The real emission matrix elements can be divided into two different sets of Feynman graphs. The first class contains all diagrams where the emitted particle is a final-state gluon. This case is shown in Fig. 3.5a, where the crosses represent possible gluon vertex insertions. The other type of diagrams comprises Feynman graphs where the emitted particle is a final-state quark and a gluon is present in the initial state. These diagrams can be obtained by a simple crossing of the diagrams of the previous class. Some sample diagrams are given in Fig. 3.5b. The second class is
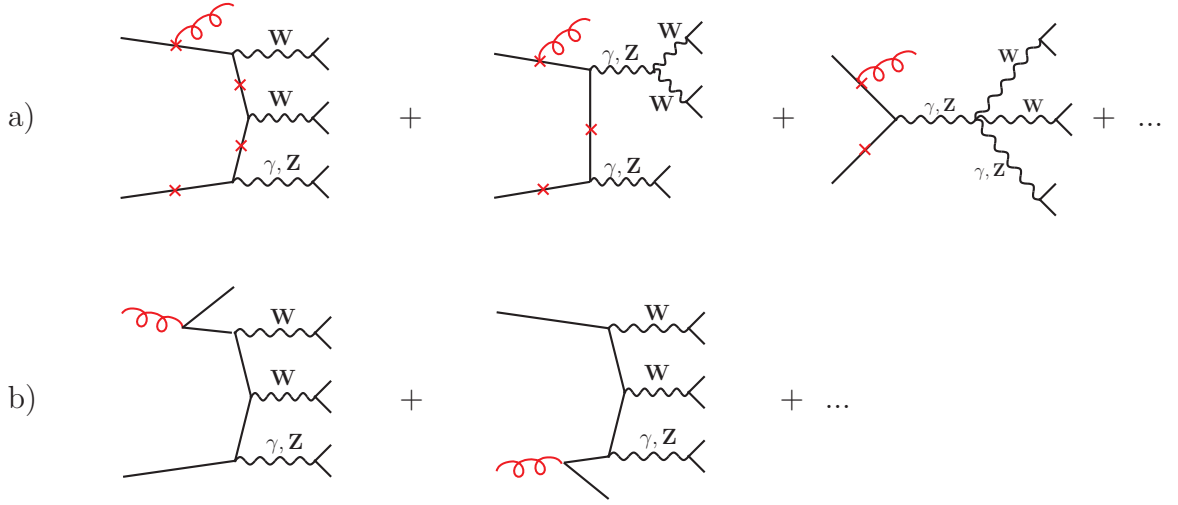
Figure 3.5: *Sample diagrams, appearing in the calculation of the real emission terms of the W^+W^-Z production.*

a completely new channel, which appears only at NLO. As we will see later in this thesis, this new channel dominates the scale dependence of the total NLO cross section and also gives a large contribution to the K-factor.

The method of precalculating effective polarization vectors for leptonic decays, described above for the tree-level diagrams, has also been used for the more complicated real emission diagrams. In the calculation of the LO cross sections with an additional jet, that is

$$W^+W^-Zj: \quad pp \to \nu_{\ell_1}\, \ell_1^+\, \ell_2^-\, \bar{\nu}_{\ell_2}\, \ell_3^-\, \ell_3^+\, j + X, \tag{3.12}$$

$$ZZW^+j: \quad pp \to \ell_1^-\, \ell_1^+\, \ell_2^-\, \ell_2^+\, \nu_{\ell_3}\, \ell_3^+\, j + X, \tag{3.13}$$

$$ZZW^-j: \quad pp \to \ell_1^-\, \ell_1^+\, \ell_2^-\, \ell_2^+\, \ell_3^-\, \bar{\nu}_{\ell_3}\, j + X, \tag{3.14}$$

it leads to an increase in computational speed of a factor of almost 20 for the WWZ production and even more for the ZZW production.

Concerning the real emission matrix elements, two different types of divergencies appear. On the one hand, there are the so-called soft divergencies, where the energy of the emitted gluon is too small to be identified experimentally as an isolated jet. On the other hand, collinear divergencies emerge if the angle between the additional
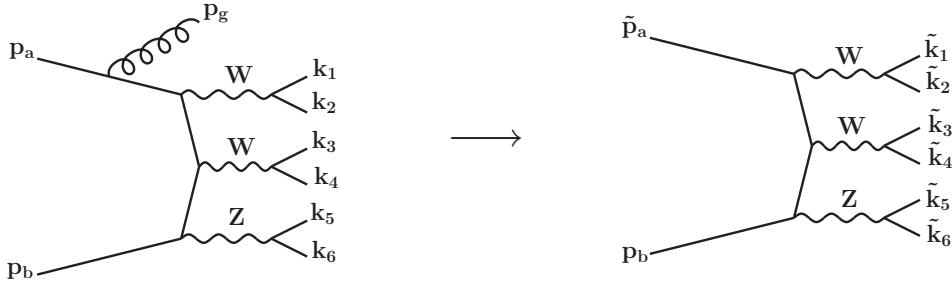
Figure 3.6: *Schematic illustration of the transformation from the (m+1)-particle kinematic to the m-particle tilde kinematic as utilized in the dipole subtraction formulas given by Catani and Seymour in Ref. [47, 48].*

parton in the real emission diagrams and the parton which emits this parton is too small to separate these two particles from each other. For both kinds of divergencies the additional dipole $d\sigma^A$ in the Catani Seymour algorithm works as a counter term. An example of a Feynman graph, where infrared divergencies might appear, is depicted on the left side of Fig. 3.6. In this case, a gluon is emitted from the upper incoming quark. It can therefore either be soft or collinear to the incoming parton. The corresponding counter term according to Catani and Seymour is given by:

$$
\begin{aligned}
d\sigma^A = & \frac{1}{2\,x\,p_a \cdot p_g}\,8\pi\alpha_s\,C_F\,\left[\frac{2}{1-x} - (1+x)\right] \\
& \cdot \left|\,M_B\left(\tilde{k}_1, ..., \tilde{k}_6;\,\tilde{p}_a, p_b\right)\,\right|^2 + \mathcal{O}(\epsilon).
\end{aligned}
\tag{3.15}
$$

Here $C_F = \frac{4}{3}$ is the color factor, p_a and p_b are the momenta of the incoming quarks. The gluon momentum is denoted by p_g, and the parameter x is defined as

$$
x = 1 - \frac{p_g \cdot (p_a + p_b)}{p_a \cdot p_b}.
\tag{3.16}
$$

The dipole $d\sigma^A$ in Eq. (3.15) is proportional to the squared Born matrix element $|M_B(\tilde{k}_1, ..., \tilde{k}_6;\,\tilde{p}_a, p_b)|^2$ with a so-called tilde kinematic. This kinematic can be obtained by a special transformation of the (m+1)-particle kinematic in such a way,

that the momentum of the additional final-state parton p_g vanishes, thus transforming to an effective m-particle kinematic. For the example at hand, this transformation from an (m+1)-particle kinematic to an m-particle kinematic is sketched in Fig. 3.6. In this special case the momentum of the upper incoming quark is only shifted, $\tilde{p}_a = x p_a$, whereas the second incoming parton momentum $\tilde{p}_b = p_b$ remains unchanged.

Similar expressions for the counter terms are obtained for the Feynman graphs with emission of a gluon from the lower incoming parton and also for the gluon induced subprocesses. Exact transformation rules as well as dipoles for all cases occurring in the triple vector boson production are given in Appendix A.

3.2.3 Finite collinear terms

The additional finite collinear terms $d\sigma^C$ in Eq. (3.11) stem from the factorization of collinear singularities into the parton distribution functions. The contributions to the $q\bar{Q}$-initiated subprocesses for instance, can be written in the compact form,

$$
\sigma_{coll}^{NLO} \left(q\bar{Q} \to 6\,\ell \right) = \int_0^1 dx_a \int_0^1 dx_b \int d\Phi_6 \left(k_1, ..., k_6; p_a + p_b \right) \frac{1}{\hat{s}}
$$
$$
\cdot \left[f_{q/p}^c \left(x_a; \mu_F^2 \right) \, f_{\bar{Q}/p} \left(x_b; \mu_F^2 \right) + f_{q/p} \left(x_a; \mu_F^2 \right) \, f_{\bar{Q}/p}^c \left(x_b; \mu_F^2 \right) \right] \qquad (3.17)
$$
$$
\cdot \left| M_{Born}^{q\bar{Q}}(k_1, ..., k_6; p_a, p_b) \right|^2 .
$$

Here, $\hat{s}$ denotes the square of the partonic center of mass energy, $|M_{Born}^{q\bar{Q}}|^2$ gives the Born matrix element squared with initial-state quark flavors q and $\bar{Q}$, and $d\Phi_6 \left(k_1, ..., k_6; p_a + p_b \right)$ represents the integration over the six-lepton final state. The two different contributions with modified pdfs $f_{q/p}^c \left(x_a; \mu_F^2 \right)$ and $f_{\bar{Q}/p}^c \left(x_b; \mu_F^2 \right)$ arising thereby are given by:

$$
f_{Q_i/p}^c \left(x_i; \mu_F^2 \right) = \frac{\alpha_s}{2\,\pi} \int_{x_i}^1 \frac{dx}{x} \left\{ f_{g/p} \left(\frac{x_i}{x}; \mu_F^2 \right) \, A(x) \right.
$$
$$
+ \left[f_{Q_i/p} \left(\frac{x_i}{x}; \mu_F^2 \right) - x \, f_{Q_i/p} \left(x_i, \mu_F^2 \right) \right] \, B(x) \qquad (3.18)
$$
$$
\left. + f_{Q_i/p} \left(\frac{x_i}{x}; \mu_F^2 \right) \, C(x) \right\} + \frac{\alpha_s}{2\,\pi} \, f_{Q_i/p} \left(x_i; \mu_F^2 \right) \, D(x_i)
$$

with the (anti) quark flavor Q_i and the corresponding Feynman-x parameter x_i. The gluonic parton distribution functions appearing in Eq. (3.18) are due to $g \to q\bar{q}$ splittings of initial-state gluons. All other contributions come from the emission of collinear gluons from the initial-state (anti) quarks. The integration kernels, $A(x)$, $B(x)$, $C(x)$, and $D(x_i)$ are universal, i.e. they do not depend on the specific $q\bar{q}$ - annihilation subprocess and they are given by:

$$A(x) = T_R \left[2\, x\, (1-x) + \left(x^2 + (1-x)^2 \right) \cdot \ln \left(\frac{(1-x)^2\, Q^2}{x\, \mu_F^2} \right) \right] \tag{3.19}$$

$$B(x) = C_F \left[\frac{2}{1-x}\ \ln \left(\frac{Q^2\, (1-x)^2}{\mu_F^2} \right) \right] \tag{3.20}$$

$$C(x) = C_F \left[1 - x - \frac{2}{1-x}\ \ln(x) - (1+x)\ \ln \left(\frac{Q^2\, (1-x)^2}{x\, \mu_F^2} \right) \right] \tag{3.21}$$

$$\begin{aligned} D(x_i) = C_F \Bigg[\frac{3}{2}\ \ln \left(\frac{Q^2}{\mu_F^2} \right) &+ 2\ \ln(1 - x_i)\ \ln \left(\frac{Q^2}{\mu_F^2} \right) \\ &+ 2\ \ln^2 (1 - x_i) \Bigg] + C_F\, \texttt{creal}. \end{aligned} \tag{3.22}$$

Here Q^2 is defined as $Q^2 = 2\ p_a \cdot p_b$, μ_F represents the factorization scale, and $C_F = \frac{4}{3}, T_R = \frac{1}{2}$ are color factors. In dimensional regularization, the finite term $\texttt{creal}$ appearing in Eq. (3.22) has the value $\texttt{creal} = \frac{\pi^2}{3} - 5$. More details on the derivation of these formulae as well as a complete summary of the finite collinear terms for all subprocesses are given in Appendix A.

In order to speed up the calculation, it is reasonable to evaluate the finite collinear terms at the same time as the real emission contribution. Thus, they are integrated over an (m+1)-particle phase space. This is possible because the two necessary phase spaces are correlated,

$$\begin{aligned} \frac{1}{2\ p_a \cdot p_b}\ &d\phi_7\, (p_g, k_1, ..., k_6; p_a + p_b) = \\ &\int_0^1 dx \int_0^{1-x} dv\ \frac{1}{2\ \tilde{p}_a \cdot p_b}\ \frac{Q^2}{8\ \pi^2}\ d\phi_6\, (\tilde{k}_1, ..., \tilde{k}_6; \tilde{p}_a + p_b). \end{aligned} \tag{3.23}$$

The parameter x, given in this formula is the one already defined in Eq. (3.16) and

$$v = \frac{p_a \cdot p_g}{p_a \cdot p_b}. \tag{3.24}$$

Relation (3.23) can then be used to rewrite Eq. (3.17) in the form, which is actually implemented in the Fortran program VBFNLO,

$$
\begin{aligned}
\sigma_{coll}^{NLO}(q\bar{Q} \to 6\,\ell) = &\int_0^1 dx_a \int_0^1 dx_b \; \frac{1}{2\,p_a \cdot p_b} \; d\Phi_7\,(k_1, ..., k_6, p_g; p_a + p_b) \\
&\frac{4\,\pi\,\alpha_s}{Q^2} \; f_{\bar{Q}/p}\,(x_b; \mu_F^2) \; \left| \; M_{Born}^{q\bar{Q}}\,(\tilde{k}_1, ... \tilde{k}_6; \tilde{p}_a, p_b) \; \right|^2 \\
&\cdot \left[f_{g/p}\,(x_a; \mu_F^2) \; A(x) + f_{q/p}\,(x_a; \mu_F^2) \; (B(x) + C(x)) \right. \\
&\left. + x\,f_{q/p}\,(xx_a; \mu_F^2) \left\{ \frac{D(xx_a)}{1 - xx_a} - B(x) \right\} \right] \cdot \frac{1}{1-x} \\
&+ (a \leftrightarrow b),\,(q \leftrightarrow \bar{Q}).
\end{aligned}
\tag{3.25}
$$

The functions $A(x)$, $B(x)$, $C(x)$ and $D(xx_a)$ are the integration kernels, already defined in Eqs. (3.19)-(3.22) and the factor $\frac{1}{1-x}$ compensates the integration $\int_0^{1-x} dv$ in Eq. (3.23).

3.2.4 Virtual contributions

The virtual contributions consist of the square of tree-level diagrams and the interference between tree-level diagrams and the virtual one-loop diagrams. In the calculation of the one-loop diagrams, three different types of contributions, corresponding to the three topologies in the tree-level calculation appear. They are schematically depicted in Fig. 3.7.

For the simplest topology (Fig. 3.7a) with one vector boson attached to the quark line, only vertex corrections appear. In this case, the one-loop contribution is proportional to the corresponding Born matrix element. The second topology Fig. 3.7b leads to propagator corrections, vertex corrections and 4-point loop integrals. In the calculation, the sum of the four virtual contributions to one specific tree-level subamplitude is grouped together and will be called a boxline contribution in the following. The most challenging topology, illustrated in Fig. 3.7c, leads to quark propagator corrections, vertex corrections, boxes and pentagons. As in the previous
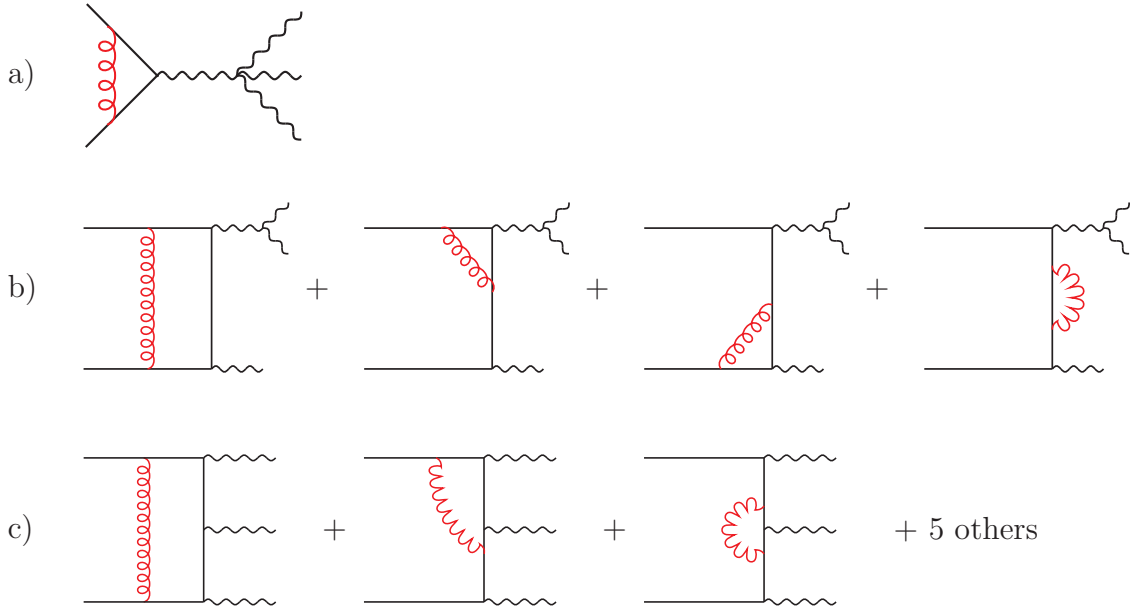
Figure 3.7: *Schematic picture of the three one-loop topologies appearing in the calculations.*

case the sum of all these corrections to one specific tree-level Feynman graph is grouped together and called pentline contribution in the following.

The singular pieces of all of these three types of virtual contributions are proportional to the corresponding Born matrix element and the complete virtual one-loop contribution for the three topologies is given by:

$$M_V = \tilde{M}_V + \frac{\alpha_S}{4\pi} C_F \left(\frac{4\pi\mu^2}{s}\right)^\epsilon \Gamma(1+\epsilon) \left[-\frac{2}{\epsilon^2} - \frac{3}{\epsilon} - 8 + \frac{4\pi^2}{3}\right] M_B, \quad (3.26)$$

where M_B denotes the full Born amplitude, s is the square of the partonic center of mass energy, i.e. it corresponds to the invariant mass of the six-lepton system, and $\tilde{M}_V$ is the finite part of the virtual boxline and pentline amplitudes. The interference term between the Born and the one-loop amplitudes is therefore

$$2 \, \mathrm{Re} \left[M_V \, M_B^* \right] = 2 \, \mathrm{Re} \left[\tilde{M}_V \, M_B^* \right]$$

$$+ \frac{\alpha_S}{2\pi} C_F \left(\frac{4\pi\mu^2}{s}\right)^\epsilon \Gamma(1+\epsilon) \left[-\frac{2}{\epsilon^2} - \frac{3}{\epsilon} - 8 + \frac{4\pi^2}{3}\right] |M_B|^2. \quad (3.27)$$

As already mentioned in the description of the algorithm by Catani and Seymour, it is possible to cancel the singular parts from the virtual contributions analytically against ϵ poles appearing in the integrated dipole $\int_1 d\sigma^A$. In the notation of Catani and Seymour the corresponding term is given by:

$$\langle\, p_a, p_b \mid \mathbf{I}(\epsilon) \mid p_a, p_b \,\rangle = \frac{\alpha_S}{2\,\pi}\, C_F\, \left(\frac{4\,\pi\,\mu^2}{s}\right)^{\epsilon}\, \Gamma(1+\epsilon)\, |M_B|^2$$
$$\cdot \left[\frac{2}{\epsilon^2} + \frac{3}{\epsilon} + 8 - \frac{4\,\pi^2}{3} + \texttt{cvirt}\right]. \tag{3.28}$$

Hence, the ϵ-poles in the virtual contributions of Eq. (3.27) and in the integrated dipole, given in Eq. (3.28), cancel exactly. In doing so only a finite rest proportional to $\texttt{cvirt} = 2$ remains. This can be integrated numerically in four dimensions.

Apart from crossing a final-state quark to the initial state, and performing an analytic continuation, the boxline and the pentline contribution have essentially the same analytic expressions found in the calculation of NLO QCD corrections in vector boson fusion processes, $qq \to Vqq$ and $qq \to VVqq$, discussed in Refs. [57] and [2–4] respectively.

To deal with the finite boxline contribution, results have been obtained by using a slightly modified version of the boxline routine presented in Ref. [57]. This routine implements the Passarino-Veltman tensor reduction [58] and leads to quite stable results.

For the pentline routine on the other hand this method still leads to serious numerical instabilities. Thus, the pentline reduction needs a more stable reduction procedure. In the calculation of tensor coefficients for the processes described here, the method proposed by Denner and Dittmaier [59, 60] has been implemented. The results have been checked with the pentline routines computed in Refs. [2–4], after crossing and analytic continuation. The new numerical tensor reduction subroutine turns out to be 4.5 times faster and numerically more stable than the old code. A detailed comparison of the two different ways to calculate pentline contributions is given in the next section.

However, even with this increase in speed of the pentagon calculation, this part of the calculation is still quite slow. Therefore, a method suggested in Refs. [2–4] has been employed to reduce the magnitude of the true pentagon contribution. In

fact, it is possible to split the effective polarization vector ϵ_V^μ of a vector boson of momentum q_V into a term proportional to the momentum itself and a remainder $\tilde{\epsilon}_V^\mu$,

$$\epsilon_V^\mu = x_V \, q_V^\mu + \tilde{\epsilon}_V^\mu. \tag{3.29}$$

The pentline contributions with an external momentum instead of the polarization vector (terms proportional to x_V) can then be expressed in terms of boxline contributions via Ward identities for the loop integrals. Therefore it is possible to shift parts of the pentline contribution to the less time consuming boxline contributions and calculate the remaining smaller true pentline contribution (the one obtained with the contraction with $\tilde{\epsilon}_V^\mu$) with less statistics, without changing the overall Monte Carlo statistical error on the total NLO result.

In practice several different possibilities have been tested for all three processes under investigation. It turned out that the best choice for the W^+W^-Z production, meaning the smallest true pentagon cross section, is obtained, when the shifted polarization vectors have zero time component in the center of mass system of the W-pair:

$$\tilde{\epsilon}_V \cdot (q_{W^+} + q_{W^-}) = 0 \qquad \Rightarrow \qquad x_V = \frac{\epsilon_V \cdot (q_{W^+} + q_{W^-})}{q_V \cdot (q_{W^+} + q_{W^-})}. \tag{3.30}$$

In performing this shift, a reduction of the magnitude of the pentline contribution by a factor of eight could be achieved. In the case of the ZZW^+ and the ZZW^- production a similar shift of the polarization vectors has been chosen:

$$\tilde{\epsilon}_V \cdot (q_{Z_1} + q_{Z_2}) = 0 \qquad \Rightarrow \qquad x_V = \frac{\epsilon_V \cdot (q_{Z_1} + q_{Z_2})}{q_V \cdot (q_{Z_1} + q_{Z_2})}. \tag{3.31}$$

In doing so, the pentline contribution could be reduced by a factor of 2.5.

3.2.5 Numerical stability and speed

For the calculation of the true pentline contributions, two different routines exist, as already mentioned in the previous section. One of them has been obtained by
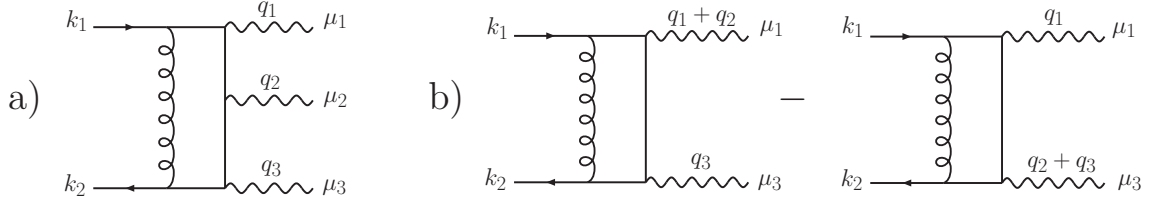
Figure 3.8: *a) Example for a pentagon graph and b) the result after contraction of this graph with external momentum $q_2^{\mu_2}$.*

crossing and analytic continuation of the subroutine described in Ref. [2–4]. The other one has been programmed from scratch in the calculation of the virtual contributions for $W^+W^-\gamma$ production [61]. The existence of two completely independent routines for the calculation of pentline contributions provides an excellent test for the correctness of the results. In the triple vector boson production processes, both codes have been implemented and for non-exceptional phase space points, agreement at the level of 10^{-8} has been found for the two different codes. Besides this test, we have seen in previous sections, that speed and numerical stability is an issue. Therefore a careful comparison of the two computer codes under this aspects is reasonable and necessary.

Both routines use the tensor reduction proposed by Denner and Dittmaier in order to avoid numerical instabilities as much as possible. Nonetheless, there are phase space points with too low numerical precision, which can lead to unnaturally large contributions to the total cross section, thus changing the cross section significantly. In order to extract these points, Ward identities for loop integrals are exploited. These identities predict, that pentline contributions contracted with an external momentum instead of a polarization vector can be expressed in terms of a difference of two boxline contributions. This property can be illustrated by means of the easier example of only one pentagon.

The formula of the pentagon, depicted in Fig. 3.8a, is given by:

$$\mathcal{P}_{\mu_1\mu_2\mu_3} = \int \frac{d^D l}{(2\,\pi)^D} \frac{\gamma^\rho (\slashed{l} + \slashed{k}_1 - \slashed{q}_{123})\gamma_{\mu_3}(\slashed{l} + \slashed{k}_1 - \slashed{q}_{12})\gamma_{\mu_2}(\slashed{l} + \slashed{k}_1 - \slashed{q}_1)\gamma_{\mu_1}(\slashed{l} + \slashed{k}_1)\gamma_\rho}{l^2\,(l + k_1)^2\,(l + k_1 - q_1)^2\,(l + k_1 - q_{12})^2\,(l + k_1 - q_{123})^2},$$

where the notation, $q_{12} = q_1 + q_2$ and $q_{123} = q_1 + q_2 + q_3$ is used for the sum of momenta and the integral over the loop momentum l has to be performed. Contracting this

expression for example with $q_2^{\mu_2}$ results in

$$
q_2^{\mu_2}\,\mathcal{P}_{\mu_1\mu_2\mu_3} = \int \frac{d^D l}{(2\,\pi)^D}\,\frac{\gamma^\rho\,(\slashed{l} + \slashed{k}_1 - \slashed{q}_{123})\,\gamma_{\mu_3}\,(\slashed{l} + \slashed{k}_1 - \slashed{q}_{12})\,\gamma_{\mu_1}\,(\slashed{l} + \slashed{k}_1)\,\gamma_\rho}{l^2\,(l+k_1)^2\,(l+k_1-q_{12})^2\,(l+k_1-q_{123})^2}
$$

$$
- \int \frac{d^D l}{(2\,\pi)^D}\,\frac{\gamma^\rho\,(\slashed{l} + \slashed{k}_1 - \slashed{q}_{123})\,\gamma_{\mu_3}\,(\slashed{l} + \slashed{k}_1 - \slashed{q}_1)\,\gamma_{\mu_1}\,(\slashed{l} + \slashed{k}_1)\,\gamma_\rho}{l^2\,(l+k_1)^2\,(l+k_1-q_1)^2\,(l+k_1-q_{123})^2}.
$$

This corresponds to the difference of two boxes, as given in Fig. 3.8b. Similar results are achieved by contraction with the other two momenta and also for the full pentline contribution. Thus, the difference of the contracted pentagon and the two box-type integrals, $q_\mu\,\mathcal{P}^\mu - Boxes$, is analytically zero and this property can be utilized to test the numerical precision of the results of the pentline contribution.

In order to ensure, that Ward identity tests only neglect terms, which contribute very little to the cross section, the difference of the contracted pentagon and the boxes is compared to the Born matrix element. Since in the actual program the polarization vectors are decay currents with an additional propagator, these additional factors have to be taken into account. This is done by weighting the difference between contracted pentline and box contributions with the zero component of the effective polarization vector ϵ_0, divided by the zero component of the corresponding momentum q_0. Furthermore, in the Born matrix element, the coupling factors of the weak bosons to the quarks are taken into account, whereas at this stage of the Pentagon calculation, they are not yet included. Therefore, an additional factor of the size of these couplings, $\texttt{couplfac} = 0.01$, is multiplied. Finally, the factor $\alpha_s/2\pi$ of Eq. (3.27) has to be included. The absolute value of the weighted difference between the contracted pentagon and the boxes compared to the Born matrix element,

$$
\Delta P = \left|\;\frac{q^\mu\,\mathcal{P}_\mu - Boxes}{M_{Born}}\;\underbrace{\frac{|\epsilon_0|}{q_0}}_{eff.pol.vector}\cdot\underbrace{\texttt{couplfac}}_{Vq\bar q-coupl.}\cdot\frac{\alpha_s}{2\,\pi}\;\right|, \tag{3.32}
$$

is then calculated for all three possible contractions of the pentline contribution with one of the external momenta. If the largest weighted difference ΔP_{max}, is smaller than a tiny number δ,

$$
\Delta P_{max} < \delta, \tag{3.33}
$$

the Ward identity test is passed. Otherwise, this pentagon contribution is discarded.

For both codes the full Pentagon contribution $\sigma_{\mathrm{Pentagon}}$ and corresponding error bars are plotted in Fig. 3.9 for various values of δ. The colored region in this figure gives the 0.1% error on the total NLO cross section, as reference. Varying δ between 10^{-2} and 10^2, the cross sections stay almost constant and there is virtually no difference between the two codes neither in the central value nor in the error bars. For larger values, $\delta = 10^3$ and $\delta = 10^4$ the error bars become larger and so does the difference between the two routines. Thus numerical stability breaks down in this region. For low values of δ, the cross section gets smaller, which means, that in this case, too many points are discarded.

In Fig. 3.10 the fraction of discarded points is plotted for both routines. For $\delta > 10^{-4}$ less than 1% of the points are neglected and for higher values of δ hardly any points do not pass this Ward identity test. The curves for the two routines lie almost on top of each other. Thus, concerning numerical stability, they are equivalent in practise. However, the number of points that do not pass the test, described above, is a little bit less for the new routine (corresponding to the the blue curve in Figs. 3.9 and 3.10). From that point of view it is then the better routine.

In the program a standard value of $\delta = 0.001$, which means a deviation of 0.1 %, has been chosen. This choice of δ ensures, that all neglected contributions to the NLO cross section account for less than 0.1% of the Born cross section and can therefore be discarded.

In the previous section it has already been mentioned that the new routine for the determination of true pentline contributions is 4.5 times faster that the old one. Moreover, as shown above, it is numerically slightly more stable. Consequently, this new routine has been chosen as default routine to calculate the pentline contribution in the program. Nonetheless, it is still possible to switch to the other code for testing purposes.
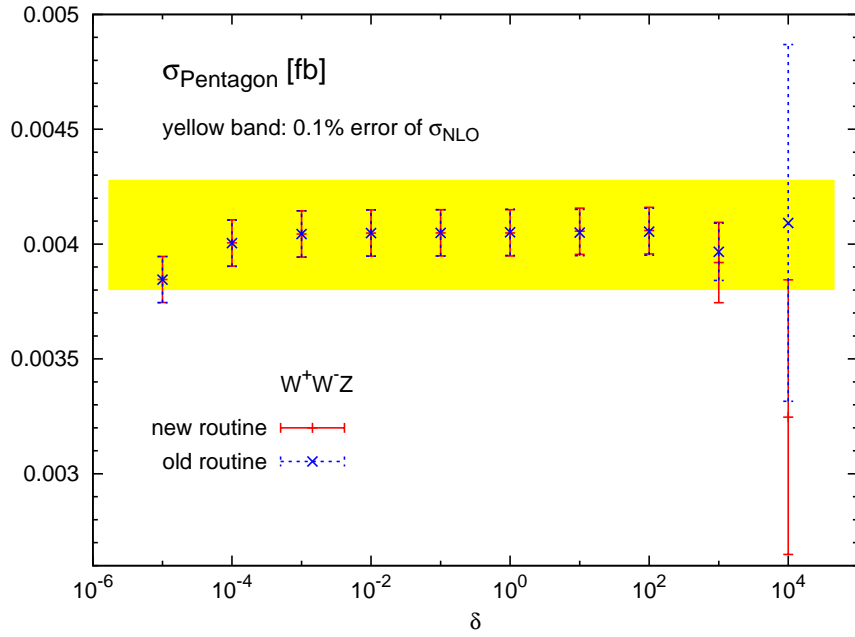
Figure 3.9: *Dependence of the pentagon cross section from the parameter δ, which reflects the numerical precision.*

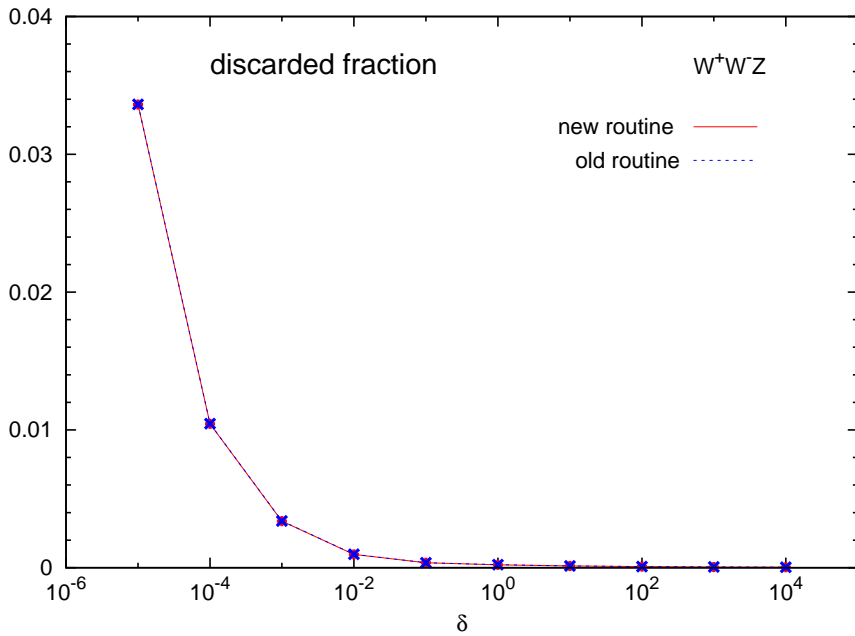

Figure 3.10: *Ratio of phase space points, which do not pass the Ward identity test and points, which pass this test, depending on the parameter δ.*

Chapter 4:

Tests and comparisons

The complete next-to-leading order calculation, as described in the previous chapter, has been implemented in the Fortran program VBFNLO [31]. In order to check the results of the various parts of the code and in order to exclude possible error sources, numerous tests have been performed.

Among them are the comparisons with HELAC [54–56] and MADEVENT [51–53] for the LO processes, which are presented in the first section of this chapter. Furthermore, ward identity tests as well as checks of the finite collinear terms and the real emission are described in subsequent sections.

The most important tests are the comparisons with the NLO results for on-shell W^+W^-Z and ZZW^+ production, recently published by T. Binoth, C. Papadopoulos, G. Ossola and R. Pittau [11]. The results of these comparisons are summarized in the last section of this chapter.

4.1 Comparisons with MadGraph, MadEvent and Helac

Concerning the LO calculations, all matrix elements have been checked against MADGRAPH [51–53]. For individual matrix elements agreement at the 10^{-15} level is found. Furthermore, this comparison has also been performed for all diagrams with an additional parton in the final state as for instance $q\bar{q} \to 4\ell + 2\nu + g$ and $qg \to 4\ell + 2\nu + q$ in the case of the WWZ production. Moreover, for each helicity configuration the squared matrix elements have been checked against MADGRAPH output for more than one million phase space points. Here, results agree at least at the 10^{-3} level but for the vast majority of points the agreement is at the 10^{-10} level or better.

In addition to these tests, the total LO cross sections for the W^+W^-Z, ZZW^+, and ZZW^- production including the leptonic decays of the three vector bosons

Higgs mass/width [GeV]	program	σ^{LO} [ab]	error [%]
$m_H = 120$	VBFNLO	29.875 ± 0.033	0.11
$\Gamma(H) = 0.004411$	HELAC	29.776 ± 0.092	0.31
$m_H = 140$	VBFNLO	49.571 ± 0.057	0.11
$\Gamma(H) = 0.008979$	HELAC	49.551 ± 0.146	0.30
$m_H = 160$	VBFNLO	62.547 ± 0.037	0.06
$\Gamma(H) = 0.077013$	HELAC	62.507 ± 0.152	0.24
$m_H = 180$	VBFNLO	52.201 ± 0.040	0.08
$\Gamma(H) = 0.598135$	HELAC	52.221 ± 0.113	0.22

Table 4.1: *Comparison of LO cross sections in* VBFNLO *and* HELAC *for the process* $pp \rightarrow W^+W^-Z + X$ *within the cuts of Eq. (4.1) and for the electroweak parameters explained in the text. Quoted cross sections effectively include branching ratios of the* W^+, W^- *and* Z *for one generation of leptons.*

Higgs mass/width [GeV]	program	σ^{LO} [ab]	error [%]
$m_H = 120$	VBFNLO	2.5159 ± 0.0045	0.18
$\Gamma(H) = 0.004411$	HELAC	2.5074 ± 0.0053	0.21
$m_H = 140$	VBFNLO	3.9962 ± 0.0047	0.12
$\Gamma(H) = 0.008979$	HELAC	3.9929 ± 0.0084	0.21
$m_H = 160$	VBFNLO	3.2911 ± 0.0033	0.10
$\Gamma(H) = 0.077013$	HELAC	3.2908 ± 0.0088	0.27
$m_H = 180$	VBFNLO	3.4339 ± 0.0031	0.09
$\Gamma(H) = 0.598135$	HELAC	3.4282 ± 0.0065	0.19

Table 4.2: *Comparison of LO cross sections in* VBFNLO *and* HELAC *for the process* $pp \rightarrow ZZW^+ + X$ *within the cuts of Eq. (4.1) and for the electroweak parameters explained in the text. Quoted cross sections effectively include branching ratios of the* W^+, W^- *and* Z *for one generation of leptons.*

Higgs mass/width [GeV]	program	σ^{LO} [ab]	error [%]
$m_H = 120$	VBFNLO	1.4444 ± 0.0023	0.16
$\Gamma(H) = 0.004411$	HELAC	1.4471 ± 0.0043	0.30
$m_H = 140$	VBFNLO	2.4337 ± 0.0036	0.15
$\Gamma(H) = 0.008979$	HELAC	2.4358 ± 0.0049	0.20
$m_H = 160$	VBFNLO	1.9388 ± 0.0031	0.16
$\Gamma(H) = 0.077013$	HELAC	1.9440 ± 0.0047	0.24
$m_H = 180$	VBFNLO	2.0219 ± 0.0029	0.14
$\Gamma(H) = 0.598135$	HELAC	2.0135 ± 0.0053	0.26

Table 4.3: *Comparison of LO cross sections in* VBFNLO *and* HELAC *for the process* $pp \to ZZW^- + X$ *within the cuts of Eq. (4.1) and for the electroweak parameters explained in the text. Quoted cross sections effectively include branching ratios of the* W^+, W^- *and* Z *for one generation of leptons.*

and all off-shell contributions have been checked against HELAC [54–56] for various Higgs masses. Results of these comparisons for the LHC are given in Tables 4.1, 4.2, and 4.3. They have been obtained using CTEQ6L1 parton distributions [62]. Standard Model parameters were set to $m_W = 80.419$ GeV, $m_Z = 91.188$ GeV, and $G_F = 1.16639 \cdot 10^{-5}$ GeV^{-2}. All other electroweak parameters have been calculated using leading order relations. Besides, the factorization scale has been set to the Z-boson mass $\mu_F = m_Z$. Furthermore, only minimal cuts on the final state leptons have been applied. Specifically, they are:

$$p_{T_\ell} > 10 \text{ GeV}, \qquad |y_\ell| < 2.5, \qquad \Delta R_{\ell\ell} > 0.4. \qquad (4.1)$$

These checks have also been performed with MADEVENT, but due to its long run time, only for one specific Higgs mass. For all three processes, the results agree within the statistical accuracy of the Monte Carlo runs (1% for MADEVENT and maximally 0.3% for HELAC).

For the LO processes with an additional jet, the complexity of the phase space and the matrix elements is much higher, which leads to an enormous increase in run time. Therefore, only a comparison with the faster of the two programs, HELAC, and only for one Higgs mass has been performed. However, also in these cases,

results agree within the accuracy of the Monte Carlo errors of about one percent.

4.2 Ward identity tests

The virtual contributions can be divided into parts proportional to the born matrix element squared, and boxline and pentline contributions, which contain boxes and pentagons, respectively. The Ward identity test, used to extract points with too low numerical precision in the pentline routine, has already been discussed in detail in the last section of the previous chapter. In this context also the comparison between the two completely different subroutines has been covered.

Similarly, for the boxline contributions, two independent codes exist, which are comparable in speed and numerical stability. The results of these two codes agree at the 10^{-8} level for almost all points checked.

However, in the case of four-point integrals, the Ward identity test is somewhat easier than in the case of pentagons, since the boxline contributions contracted with an external momentum, have to be proportional to some constant times the Born matrix element. In our implementation this constant is zero, due to the specific definition of $\tilde{M}_V$ in Eq. (3.26) and therefore the boxline contributions contracted with an external momentum have to vanish.

In the implementation into VBFNLO, this contracted box result $q_\mu J^\mu_{Box}$, weighted with the corresponding contracted Born current, is neglected when the resulting contribution is larger than a parameter δ. Specifically, phase space points are neglected for

$$\texttt{boxtest} = \frac{|q_\mu \ J^\mu_{Box}|}{\max(\ |q_0 \ J^0_{Born}|, |q_1 \ J^1_{Born}|, |q_2 \ J^2_{Born}|, |q_3 \ J^3_{Born}| \ )} > \delta. \qquad (4.2)$$

Here J^μ_{Born} gives the tree-level current corresponding to the uncontracted box contribution, i.e. the expression for the same Feynman-graphs as in the box case but without a loop.

For the parameter δ set to $\delta = 0.001$, less than 0.2% of points are discarded. Thus, only a tiny fraction of points does not pass the Ward identity test and the routine to calculate boxline contributions yields for a vast majority of points numerically stable and reliable results.

However, in order to specifically estimate the neglected cross section, the differential boxline cross section for one specific box contribution is plotted in Fig. 4.1 over the
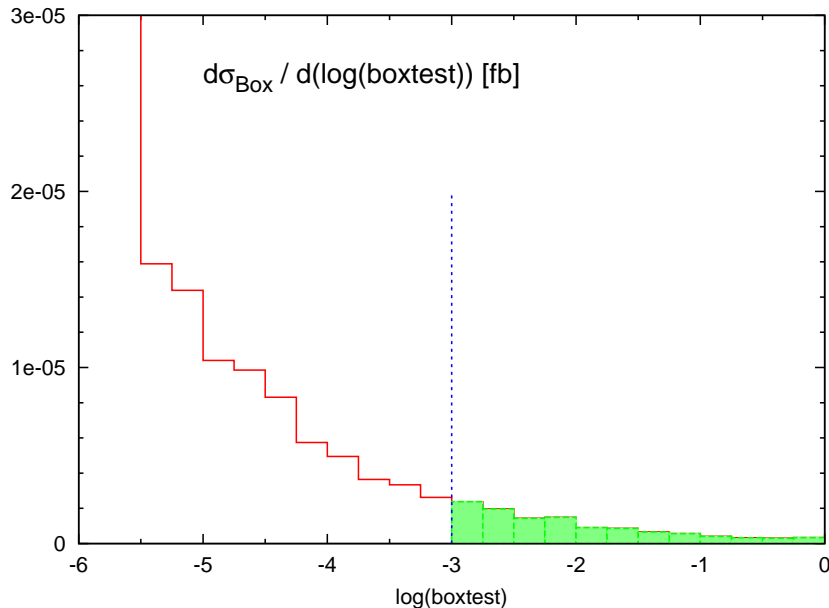
Figure 4.1: *Differential boxline cross section for one specific box contribution appearing in the calculation of the $pp \to W^+W^-Z + X$ process over the logarithm of the parameter* `boxtest`, *defined in Eq. (4.2).*

logarithm of the parameter `boxtest` defined in Eq. (4.2). For the neglected phase sp5Aace region when `boxtest` $> \delta = 0.001$, the integrated boxline cross section only amounts to less than 0.05% of the total boxline contribution for this specific case.

In the actual calculation the boxline routine is called several times for various combinations of external vector bosons and momenta. However, for all boxline contributions appearing in the tri-boson production at the LHC, the fraction of neglected points as well as of discarded cross sections is very similar as in the above case. Thus, the resultant relative error on the total box contribution is at the level of $10^{-3} - 10^{-4}$. This box contribution is about 4% of the total NLO cross section and therefore, the resultant error on σ^{NLO} is of the order of 10^{-5} or less and hence negligible.

Another very strong test of the correctness of the implementation of virtual corrections, relies on the possibility to calculate parts of the pentline contribution together with the boxline contribution. This method is used to reduce the magnitude of the true pentagon contribution, as explained in the previous chapter. It has already been pointed out in that context that the choice of the shifted polarization vectors, defined in Eqs. (3.29), (3.30) and (3.31) is ambiguous. However, the result of the

shift	contribution	cross section [ab]
	boxline contribution	-0.2667 ± 0.0012
no shift	pentline contribution	0.6641 ± 0.0014
	$\sigma^{boxline} + \sigma^{pentline}$	0.3974 ± 0.0018
	boxline contribution	0.0911 ± 0.0007
$\tilde{\epsilon}_V \cdot q_{ZZW} = 0$	pentline contribution	0.3073 ± 0.0012
	$\sigma^{boxline} + \sigma^{pentline}$	0.3985 ± 0.0014
	boxline contribution	0.1489 ± 0.0009
$\tilde{\epsilon}_V \cdot q_{ZZ} = 0$	pentline contribution	0.2497 ± 0.0012
	$\sigma^{boxline} + \sigma^{pentline}$	0.3985 ± 0.0015

Table 4.4: *In this table, the cross sections of boxline and pentline contributions and their sum are given for the ZZW^+ production within the cuts of Eq. (4.1). Three different choices for the shift of the external polarization vectors, analogous to Eqs. (3.29), (3.30) and (3.31) are listed. The total NLO cross section for the leptonic final state chosen here is $\sigma^{NLO} = 5.762 \pm 0.005$ ab.*

sum of boxline and pentline contributions on the other hand has to be the same for every choice. In Table 4.4 three different choices and the corresponding boxline and pentline cross sections are given for the ZZW^+ production within the cuts of Eq. (4.1).

The sum of boxes and pentagons agrees for all of these choices up to the accuracy of the Monte Carlo errors, which are below 0.5%. For the other processes, presented in this work, the same has been done. Also in those cases, the virtual contributions do not change for different choices of the shifted polarization vectors.

4.3   Real emission and finite collinear terms

In the formalism of Catani and Seymour the subtraction terms $d\sigma^A$ act as local counter terms. Thus, they have to exactly cancel the real emission contribution in the singular regions, that means for small energies of the emitted gluon and for collinear partons. This property of the subtracted dipoles has been tested numerically for all processes under investigation.

For the W^+W^-Z production the real emission cross section divided by the dipoles has been plotted in Fig. 4.2 over the energy of the final state gluon for about one million phase space points. As expected, for gluon energies larger than 10 GeV,

$\mu_F = \mu_R = \mu,\ \alpha_s(\mu_R)$	program	σ^{LO} [fb]	σ^{NLO} [fb]
$\mu = m_W,\ \alpha_S = 0.12028$	VBFNLO	446.30 ± 0.26	735.01 ± 0.71
	MCFM	445.87 ± 0.43	735.59 ± 0.66
$\mu = 10 \cdot m_W,\ \alpha_S = 0.088978$	VBFNLO	532.12 ± 0.31	714.64 ± 0.63
	MCFM	531.48 ± 0.44	715.57 ± 0.64

Table 4.5: *Comparison of the LO and NLO cross sections in MCFM and VBFNLO for W^+W^- production at the LHC within the cuts of Eq. (4.1).*

the real emission cross section and the dipoles differ heavily and as gluon energies become smaller, the ratio of real emission cross section over dipole cross sections approaches one.

In order to confirm the cancellation of collinear singularities, the ratio of real emission cross section over dipole cross sections has been plotted in Fig. 4.3 over the minimum of the scalar products between momentum of an initial-state parton $p_{initial}$ and the one of the final-state parton p_{final}. Again, for large values of this scalar product, cross sections differ whereas in the collinear region $p_{initial} \cdot p_{final} \to 0$, the subtraction terms exactly cancel the real emission contributions resulting in a ratio of real emission cross section divided by dipole cross sections of one.

The finite collinear terms have been checked by exploiting the fact that they are generic for all Drell-Yan type processes and hence, should be exactly the same for di-boson production. Therefore, the NLO QCD corrections for the process $pp \to W^+W^- + X$ have independently been programmed and results have been compared with the already existing parton level Monte Carlo program MCFM [30]. The results of the tests are given in Table 4.5. They have been obtained using CTEQ6L1 and CTEQ6M [62] pdfs for the calculation of LO and NLO cross sections. The strong coupling constant has been chosen to be $\alpha_s(m_Z) = 0.118$. In addition to that, the electroweak parameters, already described in the comparison with HELAC and the cuts of Eq. (4.1) have been used. The comparison has been performed for two different factorization and renormalization scales. For both of them the two Monte Carlo programs agree within the error of the Monte Carlo runs, which is for LO and NLO cross sections below 0.1%.
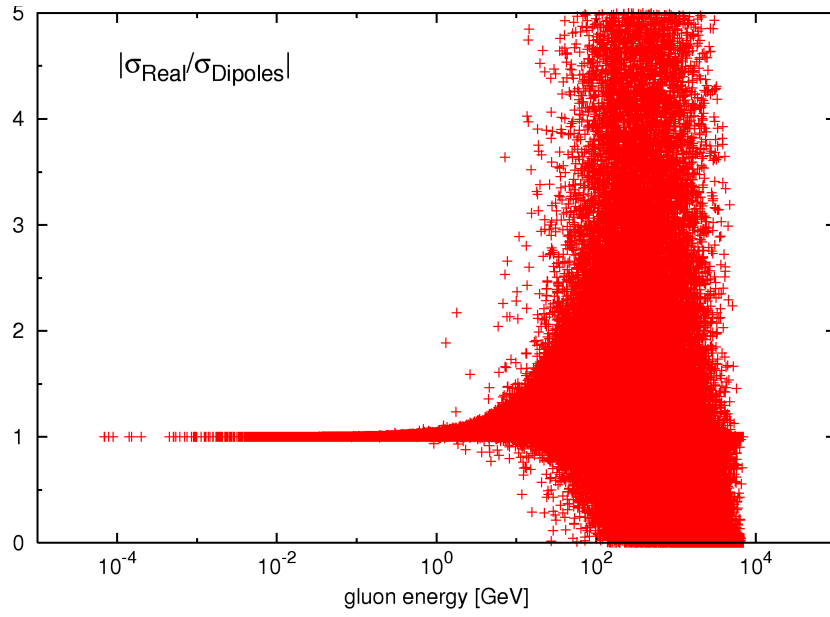
Figure 4.2: *Ratio of real emission cross section over cross section of the subtraction terms for different values of the gluon energy.*
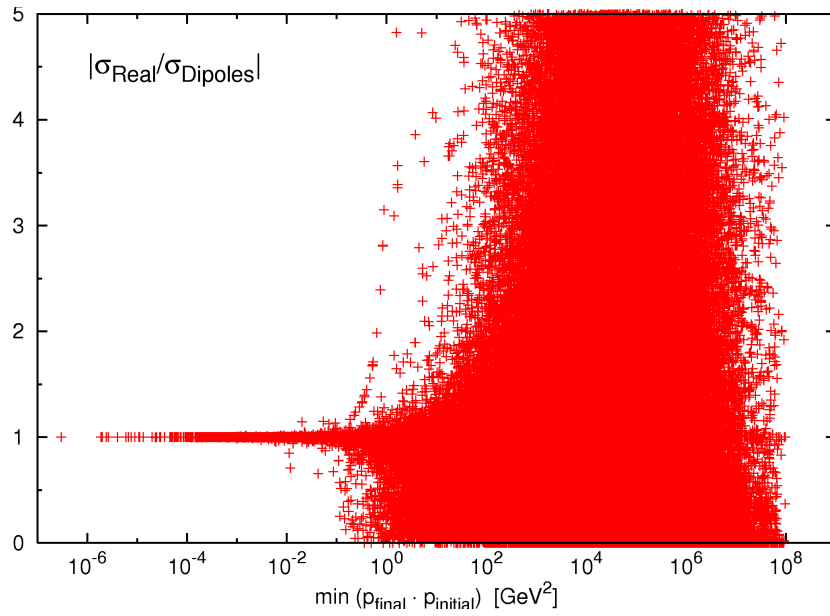

Figure 4.3: *Same as in Fig. 4.2 but for different values of the minimum of scalar products between final-state parton momentum p_{final} and initial-state parton momentum $p_{initial}$.*

4.4 Relation between m- and (m+1)-particle phase space

A further check takes advantage of the fact that it is possible to integrate terms proportional to the Born matrix element either together with the real emission part, by integration over the (m+1)-particle phase space, or together with the virtual part, by integrating over the m-particle phase space.

Specifically, the constant terms, `creal` of Eq. (3.22) and `cvirt` of Eq. (3.28) can be chosen arbitrarily, and only their sum,

$$\mathtt{csum} = \mathtt{creal} + \mathtt{cvirt} = \frac{\pi^2}{3} - 5 + 2 = \frac{\pi^2}{3} - 3, \tag{4.3}$$

has to stay the same. That means, parts of the virtual calculation can be shifted to the calculation of finite collinear terms or the other way around. For all processes under investigation, various combinations of `cvirt` and `creal` have been tested and results for the subtracted real emission cross section, the virtual cross section and the total NLO cross section are given in Table. 4.6 for the three choices,

$$\mathtt{cvirt} = \frac{2\,\pi^2}{3} - 3, \qquad \mathtt{creal} = -\frac{\pi^2}{3}, \qquad \Rightarrow \mathtt{csum} = \frac{\pi^2}{3} - 3, \tag{4.4}$$

$$\mathtt{cvirt} = 20 + \frac{\pi^2}{3} - 3, \qquad \mathtt{creal} = -20, \qquad \Rightarrow \mathtt{csum} = \frac{\pi^2}{3} - 3, \tag{4.5}$$

$$\mathtt{cvirt} = -20 + \frac{\pi^2}{3} - 3, \qquad \mathtt{creal} = +20, \qquad \Rightarrow \mathtt{csum} = \frac{\pi^2}{3} - 3. \tag{4.6}$$

The resulting cross sections for all three cases agree within the accuracy of the Monte Carlo run and are thus independent of the specific choice of `cvirt` and `creal` but only depend on their sum.

The purpose of this check is twofold. First, it confirms the relation between the m- and the (m+1)-particle phase space given in Eq. (3.23). Thus the implementation of finite collinear terms are tested. Second, it ensures, that in the virtual and the real emission calculation all parameters like α_s and the color factors are chosen in the same way. Therefore this is a very powerful test, since it checks two completely independent parts of the computer program against each other.

process	creal, cvirt	σ^{real} [ab]	σ^{virtual} [ab]	σ^{NLO} [ab]
W^+W^-Z	Eq. (4.4)	15.78 ± 0.05	44.63 ± 0.10	60.41 ± 0.11
	Eq. (4.5)	4.79 ± 0.10	55.53 ± 0.16	60.32 ± 0.19
	Eq. (4.6)	37.21 ± 0.18	23.02 ± 0.08	60.24 ± 0.20
ZZW^+	Eq. (4.4)	1.998 ± 0.005	3.760 ± 0.010	5.758 ± 0.011
	Eq. (4.5)	1.089 ± 0.012	4.671 ± 0.019	5.760 ± 0.023
	Eq. (4.6)	3.760 ± 0.012	1.999 ± 0.007	5.759 ± 0.014
ZZW^-	Eq. (4.4)	1.277 ± 0.005	2.159 ± 0.008	3.436 ± 0.010
	Eq. (4.5)	0.762 ± 0.005	2.667 ± 0.005	3.429 ± 0.007
	Eq. (4.6)	2.294 ± 0.004	1.134 ± 0.002	3.429 ± 0.005

Table 4.6: *Comparison of NLO cross sections for the three choices of* `creal` *and* `cvirt` *given in Eqs. (4.4)-(4.6). The variables* `creal` *and* `cvirt` *are defined in Eqs. (3.22) and (3.28). Quoted cross sections effectively include branching ratios of the* W^+*,* W^- *and Z for one generation of leptons.*

4.5 $pp \to \text{ZZW}$ vs. $\bar{p}\bar{p} \to \text{ZZW}$

In the program VBFNLO, not only cross sections and distributions for proton induced processes $pp \to VVV + X$, but also for antiproton induced processes of the form $\bar{p}\bar{p} \to VVV + X$, can be calculated. This feature of the program can be used for another very important test of the ZZW production. The processes $pp \to ZZW^+ + X$ and $\bar{p}\bar{p} \to ZZW^- + X$ should give the same results for the LO and the NLO cross sections and the same is also valid for the two processes $pp \to ZZW^- + X$ and $\bar{p}\bar{p} \to ZZW^+ + X$. This statement is not only true for total cross sections, but allows to test every individual part such as the real emission contribution and the different virtual contributions. For the cuts given in Eq. (4.1) and the parameters defined for the comparison with HELAC in Section 4.1, the results for the comparison are given in Table. 4.7 for a Higgs mass of $m_H = 120$ GeV.

For all individual contributions to the cross section listed here, results agree within the statistical errors of the Monte Carlo runs, which are well below 1%.

4.6 Comparison with independent calculations

During 2007 and 2008, several publications on next-to-leading order QCD corrections to triple vector boson production at the LHC have appeared. The content of two of

process	σ^{LO} [ab]	$\sigma^{\mathrm{virtual}}$ [ab]	σ^{real} [ab]	σ^{NLO} [ab]
$pp \to \mathrm{ZZW}^+$	2.524 ± 0.004	3.562 ± 0.008	2.142 ± 0.008	5.703 ± 0.011
$\bar{p}\bar{p} \to \mathrm{ZZW}^-$	2.517 ± 0.005	3.575 ± 0.010	2.157 ± 0.019	5.732 ± 0.022
$pp \to \mathrm{ZZW}^-$	1.444 ± 0.002	2.064 ± 0.005	1.429 ± 0.007	3.493 ± 0.009
$\bar{p}\bar{p} \to \mathrm{ZZW}^+$	1.443 ± 0.004	2.046 ± 0.006	1.421 ± 0.007	3.468 ± 0.009

Table 4.7: *Comparison of the LO and NLO cross sections for $pp \to ZZW^\pm + X$ and $\bar{p}\bar{p} \to ZZW^\pm + X$ within the cuts of Eq. (4.1). Quoted cross sections effectively include branching ratios of the W^+, W^- and Z for one generation of leptons.*

them, Refs. [9,14], is described in this PhD thesis and in the diploma thesis by Stefan Prestel. Besides, in Ref. [5], NLO QCD corrections for the process $pp \to ZZZ + X$ are presented by A. Lazopoulos, K. Melnikov and F. Petriello, albeit without further decay of the leptons and neglecting any Higgs contributions. Furthermore, a paper on on-shell $W^+W^-W^+$, W^+W^-Z, ZZZ, and ZZW^+ production has been published by T. Binoth, G. Ossola, C. G. Papadopoulos and R. Pittau [11]. In this paper, as in the previous one, Higgs contributions have been neglected.

In order to be able to compare LO and NLO cross sections with the other two groups, some modifications of the VBFNLO code were necessary. First, since both of them did not include Higgs contributions and leptonic decays, all Feynman graphs, except the ones also appearing in their calculations, had to be neglected. This leaves us with 15 diagrams for WWZ production and 13 diagrams for ZZW production at LO. In addition, the results in narrow width approximation divided by the branching ratios had to be multiplied with suitable symmetry factors. They arise when identical particles, as for instance two Z-bosons, appear in the final state.

Although Ref. [5] only provides results for the process $pp \to ZZZ + X$, many of the critical elements of the calculation performed in the work presented here also appear in this related process. Therefore, the VBFNLO code has been modified to describe ZZZ instead of WWZ production and has been checked against the results of Ref. [5]. Using the same pdfs and $\alpha_s (m_Z) = 0.119$ at NLO the numbers completely agree for all of the given renormalization and factorization scales.

As a final and very important test, a comparison with the results of Ref. [11] has been realized. In Tables 4.8 and 4.9 the results are shown for different factorization and renormalization scale choices, here taken to be equal. The NLO results agree at the one percent level, which is satisfactory given the same level of agreement for the LO cross sections and the size of the Monte Carlo errors.

scale	program	σ^{LO} [fb]	σ^{NLO} [fb]
$\mu_F = \mu_R = 2 \cdot m_W + m_Z$	VBFNLO	97.5 ± 0.1	186.5 ± 0.3
	Ref. [11]	96.8 ± 0.6	185.5 ± 0.8

Table 4.8: *Comparison between results of Ref. [11] and the ones obtained with* VBFNLO *for the process* $pp \to W^+ W^- Z + X$. *All parameters and settings are taken from Ref. [11].*

scale	program	σ^{LO} [fb]	σ^{NLO} [fb]
$\mu_F = \mu_R = \frac{1}{2} \times (3\ m_Z)$	VBFNLO	20.42 ± 0.03	43.02 ± 0.08
	Ref. [11]	20.2 ± 0.1	43.0 ± 0.2
$\mu_F = \mu_R = 2 \cdot m_Z + m_W$	VBFNLO	20.30 ± 0.03	39.87 ± 0.08
	Ref. [11]	20.2 ± 0.1	40.4 ± 0.2
$\mu_F = \mu_R = (3\ m_Z)$	VBFNLO	20.24 ± 0.03	39.86 ± 0.07
	Ref. [11]	20.0 ± 0.1	39.7 ± 0.2
$\mu_F = \mu_R = 2 \times (3\ m_Z)$	VBFNLO	20.03 ± 0.03	37.39 ± 0.07
	Ref. [11]	19.7 ± 0.1	37.8 ± 0.2

Table 4.9: *Comparison between results of Ref. [11] and the ones obtained with* VBFNLO *for the process* $pp \to ZZW^+ + X$. *All parameters and settings are taken from Ref. [11].*

Chapter 5:

Cross sections and distributions

The complete next-to-leading order calculations for the W^+W^-Z, the ZZW^+, and the ZZW^- production cross sections have been implemented in the framework of a fully flexible parton-level Monte-Carlo program, VBFNLO, which has been used to determine the QCD corrections for these triple vector boson production processes at the LHC, i.e. for a proton-proton collider with 14 TeV center of mass energy.

The chapter at hand presents the results. In the first section, the default values for the electroweak parameters, scales, and cuts are introduced. Next, the Higgs mass dependence of the different processes is discussed. Section 5.3 covers the scale dependence of the NLO cross section, which is often used as an indication of the uncertainty of the results. Subsequently, the strong phase space dependence of NLO results is proven by means of differential distributions and K-factors. The chapter is finally closed by an estimate on the pdf uncertainties entering in the calculation of the cross section.

5.1   Cuts, scales and parameters

For the generation of results the electroweak parameters have been chosen in the following way:

$$
m_W = 80.398 \text{ GeV}, \qquad\qquad m_Z = 91.1876 \text{ GeV},
$$
$$
G_F = 1.16637 \cdot 10^{-5} \text{ GeV}^{-2}.
$$
(5.1)

The other electroweak parameters, $\alpha^{-1} = 132.3407$ and $\sin^2(\theta_W) = 0.22246$, are calculated in the program by using LO electroweak relations. The default value for the Higgs mass is $m_H = 120$ GeV. Furthermore, in the prediction of the Higgs mass dependence of the cross section, the top quark mass is needed for Higgs masses
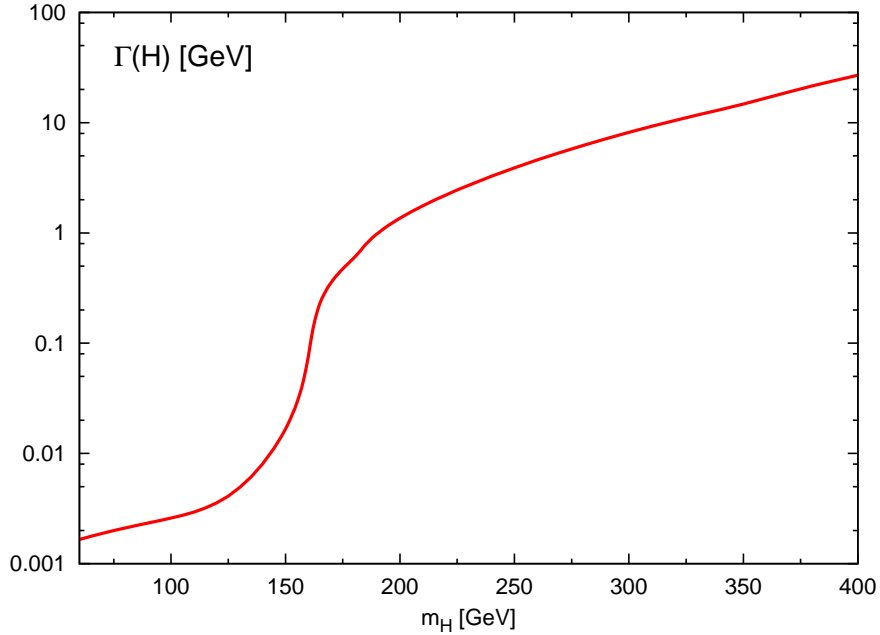
Figure 5.1: *Total Higgs width under variation of the Higgs mass. The plot has been generated with* VBFNLO.

above the top-quark pair threshold. It is set to 172.4 GeV according to the current world average [38].

The W- and Z-boson widths have been calculated in the program via tree-level formulas with one-loop QCD corrections for the hadronic partial widths. For Higgs boson decays, approximate formulas are used which incorporate running bottom-quark mass effects and off-shell effects in Higgs decays to weak bosons. However, Higgs boson widths computed in VBFNLO have been checked against results from HDECAY, a program which calculates Higgs widths and branching ratios including all higher order QED and QCD corrections available at the moment [63, 64]. The widths agree up to a Higgs mass of 300 GeV at the few percent level and even for $m_H = 400$ GeV results only differ by 8%. The total Higgs decay widths and also the branching ratios used for the following plots are given in Figs. 5.1 and 5.2. In particular for $m_H = 120$ GeV, the resulting widths for all massive vector bosons are

$$\Gamma_W = 2.0994 \text{ GeV} , \qquad \Gamma_Z = 2.5096 \text{ GeV} , \qquad \Gamma_H = 0.004411 \text{ GeV} . \qquad (5.2)$$

As default value for the renormalization and factorization scale the fixed scale, $\mu = \mu_F = \mu_R = 3 \cdot m_W$ has been chosen. If not specified otherwise, CTEQ6M
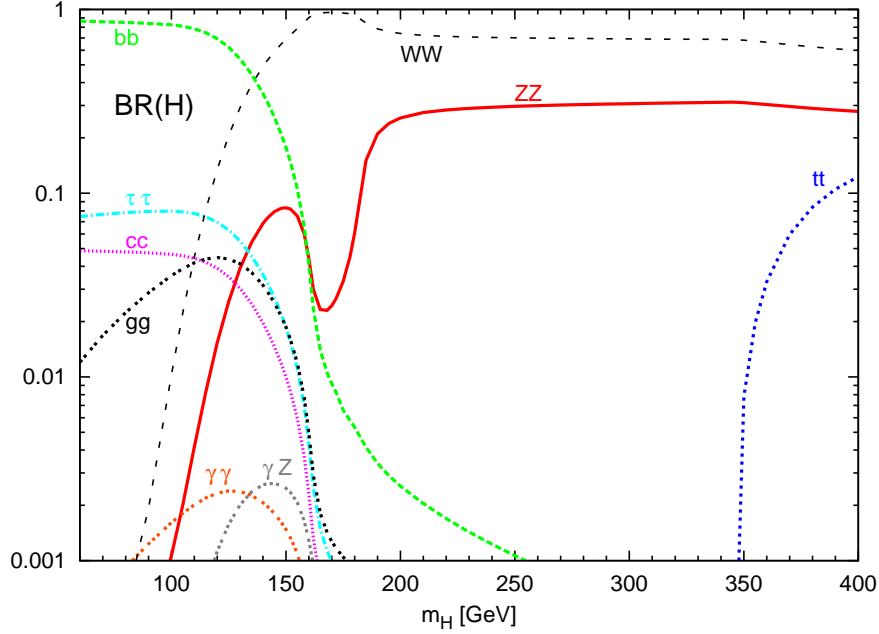
Figure 5.2: *Higgs branching ratios under variation of the Higgs mass. The plot has been generated with* VBFNLO.

parton distributions with $\alpha_s(m_Z) = 0.118$ have been applied for the NLO calculation and CTEQ6L1 pdfs have been used for LO predictions [62]. All fermions are treated as massless and contributions involving bottom and top quarks are not considered. The CKM matrix is approximated by a unit matrix throughout, which is appropriate when neglecting fermion mass effects in a neutral Drell-Yan type process, as has been pointed out in Chapter 3.

In order to keep most of the cross section only minimal cuts have been applied to the final state leptons. This means that besides a cut on the minimal transverse momentum and the maximal rapidity of the charged leptons, it is only required that the invariant di-lepton mass, $m_{\ell^+\ell^-}$, of any combination of oppositely charged leptons is larger than 15 GeV. Thus virtual photon singularities in $\gamma^* \to \ell^+\ell^-$ at low $m_{\ell^+\ell^-}$ are avoided. Specifically,

$$p_{T_\ell} > 10 \text{ GeV}, \qquad |y_\ell| < 2.5, \qquad m_{\ell^+\ell^-} > 15 \text{ GeV}, \qquad (5.3)$$

is required in all subsequent figures.

All results given here have been calculated for three different lepton families in the final state, i.e. interference terms due to identical particles have been neglected. Phenomenologically more interesting are the cases of final states with electrons and/or muons.

In the case of WWZ production, there are eight different final states with leptons of the first two families only,

$$
\begin{aligned}
pp &\rightarrow \nu_e \, e^+ \, e^- \, \bar{\nu}_e \, e^- \, e^+ + \mathrm{X}, \\
pp &\rightarrow \nu_e \, e^+ \, e^- \, \bar{\nu}_e \, \mu^- \, \mu^+ + \mathrm{X}, \\
pp &\rightarrow \nu_e \, e^+ \, \mu^- \, \bar{\nu}_\mu \, e^- \, e^+ + \mathrm{X}, \\
pp &\rightarrow \nu_e \, e^+ \, \mu^- \, \bar{\nu}_\mu \, \mu^- \, \mu^+ + \mathrm{X}, \\
pp &\rightarrow \nu_\mu \, \mu^+ \, e^- \, \bar{\nu}_e \, e^- \, e^+ + \mathrm{X}, \\
pp &\rightarrow \nu_\mu \, \mu^+ \, e^- \, \bar{\nu}_e \, \mu^- \, \mu^+ + \mathrm{X}, \\
pp &\rightarrow \nu_\mu \, \mu^+ \, \mu^- \, \bar{\nu}_\mu \, e^- \, e^+ + \mathrm{X}, \\
pp &\rightarrow \nu_\mu \, \mu^+ \, \mu^- \, \bar{\nu}_\mu \, \mu^- \, \mu^+ + \mathrm{X}.
\end{aligned}
\tag{5.4}
$$

Neglecting interference terms due to identical particles in the final state, the cross section for all of these processes is the same. Therefore, results for the WWZ production have been multiplied with a combinatorial factor of eight in all figures. In the case of the ZZW^+ process, six different final states with electrons and muons in the final state are possible,

$$
\begin{aligned}
pp &\rightarrow e^- \, e^+ \, e^- \, e^+ \, \nu_e \, e^+ + \mathrm{X}, \\
pp &\rightarrow e^- \, e^+ \, e^- \, e^+ \, \nu_\mu \, \mu^+ + \mathrm{X}, \\
pp &\rightarrow e^- \, e^+ \, \mu^- \, \mu^+ \, \nu_e \, e^+ + \mathrm{X}, \\
pp &\rightarrow e^- \, e^+ \, \mu^- \, \mu^+ \, \nu_\mu \, \mu^+ + \mathrm{X}, \\
pp &\rightarrow \mu^- \, \mu^+ \, \mu^- \, \mu^+ \, \nu_e \, e^+ + \mathrm{X}, \\
pp &\rightarrow \mu^- \, \mu^+ \, \mu^- \, \mu^+ \, \nu_\mu \, \mu^+ + \mathrm{X}.
\end{aligned}
\tag{5.5}
$$

However, for both Z-bosons decaying to electrons or both decaying to muons, the cross sections only amount to one half of the cross section of processes with three
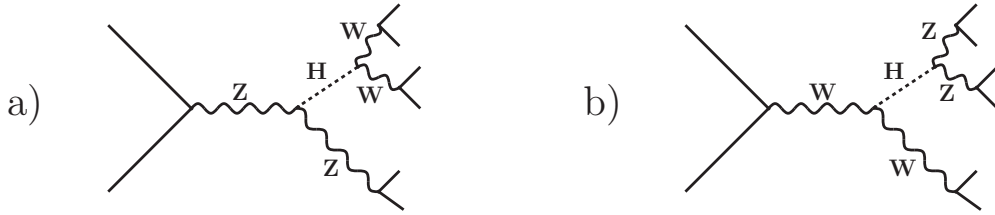
Figure 5.3: *Feynman graphs for the Higgs contribution in a) the WWZ production and b) the ZZW production.*

different families in the final state. The same is true for the ZZW$^-$ production. Hence, results for the ZZW processes have been multiplied with a combinatorial factor of four in all figures. A more detailed explanation for these combinatorial factors is given in Appendix B.

5.2 Higgs mass dependence of the cross sections

The cross sections of the processes discussed here heavily depend on the assumed Higgs mass. Since the mass of all fermions has been set to zero in the calculations and Higgs-fermion-fermion couplings in the SM are proportional to the fermion mass itself, Feynman graphs involving $Hq\bar{q}$ and $H\ell^+\ell^-$ vertices do not contribute to the cross sections. Concerning vector bosons, only HWW and HZZ couplings, which are proportional to the vector boson mass squared, appear at the leading order. Therefore, the only diagrams with an intermediate Higgs boson are those given in Fig. 5.3a for WWZ and in Fig. 5.3b for ZZW production.

In Fig. 5.3a, the Higgs boson decays into two W-bosons, and in Fig. 5.3b into two Z-bosons. For a Higgs mass above twice the vector boson mass, these vector bosons can become on-shell. Thus, for the W$^+$W$^-$Z case, one expects a maximum of the cross sections slightly above $m_H = 2 \cdot m_W$ and slightly above $m_H = 2 \cdot m_Z$ for the ZZW$^-$ and ZZW$^+$ production modes. For low Higgs masses, on the other hand, i.e. $m_H < m_V$, almost no contribution of the Higgs graph is anticipated, because neither of the two vector bosons can be produced on-shell, hence the probability to find two vector bosons with very small invariant masses is quite low. With increasing Higgs mass, one vector boson can become on-shell, leading to larger and larger effects of the Higgs graph, until both vector bosons can become on-shell. However, once the Higgs mass has passed the vector boson pair threshold, the importance of Higgs contributions decreases again with increasing Higgs masses. This behavior is due to

the fact that the Higgsstrahlung cross section $\sigma(q\bar{q} \rightarrow HV)$, itself decreases as the Higgs mass goes further up. Finally, for very large Higgs masses almost no Higgs contribution is expected.

In Fig. 5.4 exactly this behavior is confirmed for the W^+W^-Z cross section: For small Higgs masses below $m_H \leq m_W$, no effect of the Higgs graph is observed. As the Higgs mass becomes larger, the LO and NLO cross sections increase. At about 160 GeV there is a pronounced maximum and for even larger Higgs masses the cross section decreases again. Finally, at the upper end of the plotted curve at $m_H = 400$ GeV, the impact of the Higgs contribution is almost zero.

Although the two curves for the LO and the NLO cross sections show qualitatively the same features, quantitatively there is a difference between them. This discrepancy is visualized in Fig. 5.5, where the corresponding K-factor, defined as the ratio of NLO cross section divided by LO cross section, is plotted. For very small and very large Higgs masses with virtually zero Higgs contribution, the K-factor is maximal and amounts to K $\simeq 2.1$. Around the maximum of the cross section, on the other hand, Higgs graphs lead to a sizeable enhancement of the cross section, but the K-factor is minimal with K $\simeq 1.5$. These large differences result from the fact that the QCD corrections to the Higgs contribution itself are only in the range of 30% of the LO cross section [65–69]. Thus, the more dominant the Higgs contribution, the closer is the K-factor to K $\simeq 1.3$.

In the case of the ZZW processes, a somewhat different Higgs mass dependence of the LO as well as NLO cross sections is observed. The new features arising thereby are illustrated in Fig. 5.6 by means of the ZZW^+ production. Although the overall shape is the same as already shown for W^+W^-Z production, besides the global maximum at about $m_H = 2 \cdot m_Z$ a local minimum slightly above a Higgs mass of 160 GeV is found. This minimum is connected with a rise in the total Higgs decay width. At 160 GeV, the $H \rightarrow WW$ partial decay width becomes large, because both W-bosons can then be on-shell. Thus, the total decay width is strongly enhanced as depicted in Fig. 5.1. Since the Higgs width enters in the calculation of the ZZW^+ cross section in the denominator, a large Higgs width leads to a smaller cross section. However, exactly the same shape is observed for the $H \rightarrow ZZ$ branching ratio, plotted in Fig. 5.2. In fact, the cross section for the Higgs contribution to the on-shell ZZW production could be reproduced by calculating the process $pp \rightarrow HW$ and multiplying the result with the branching ratio of $H \rightarrow ZZ$. Regarding it that way, the shape of the Higgs mass dependence is not astonishing.

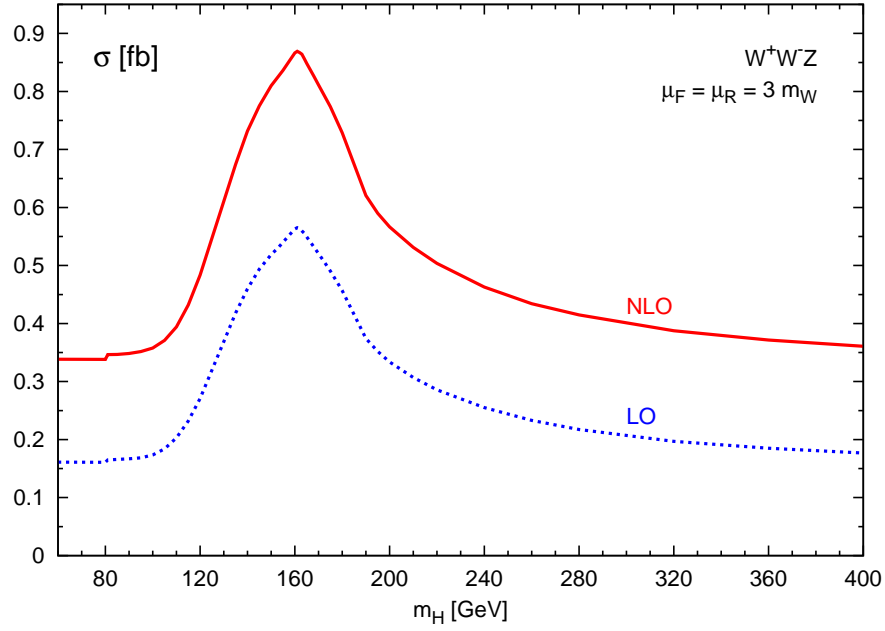Concerning K-factors, the features already observed in WWZ production also hold

Figure 5.4: *Higgs mass dependence of the cross section at LO and NLO for the* W^+W^-Z *production at the LHC within the cuts of Eq. (5.3). The plotted cross sections effectively include the branching ratios of the W- and Z-bosons for decays into electrons and/or muons.*
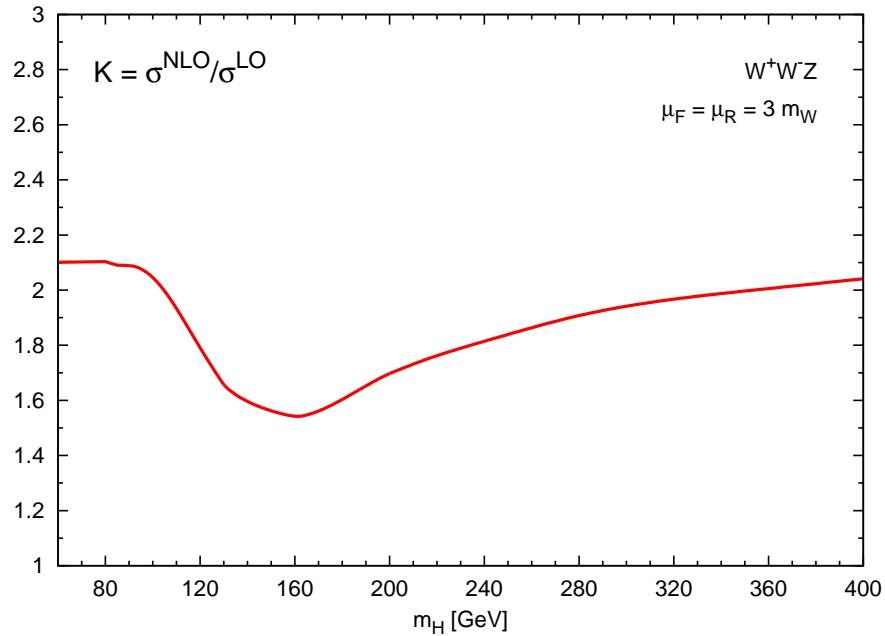

Figure 5.5: *Higgs mass dependence of the K-factor for* W^+W^-Z *production at the LHC within the cuts of Eq. (5.3).*
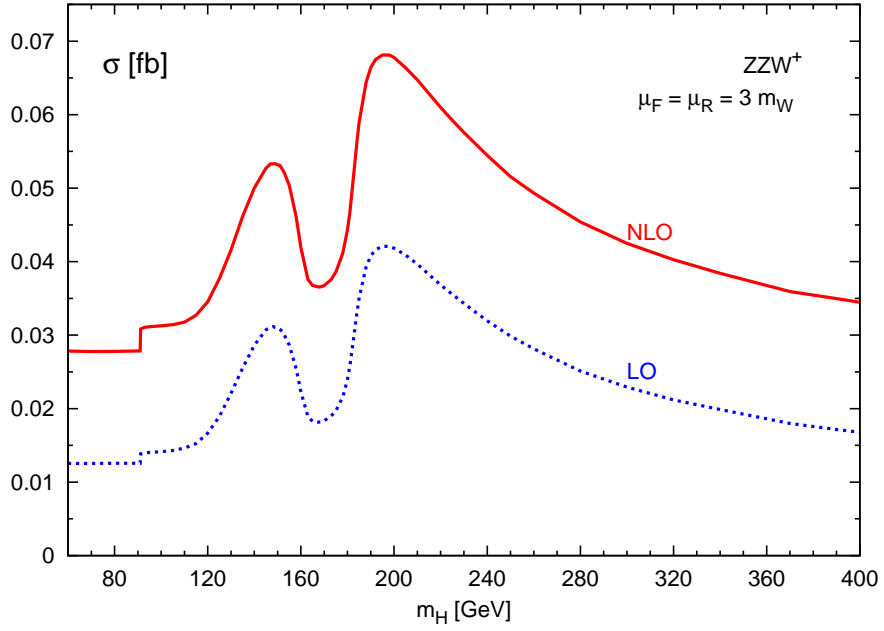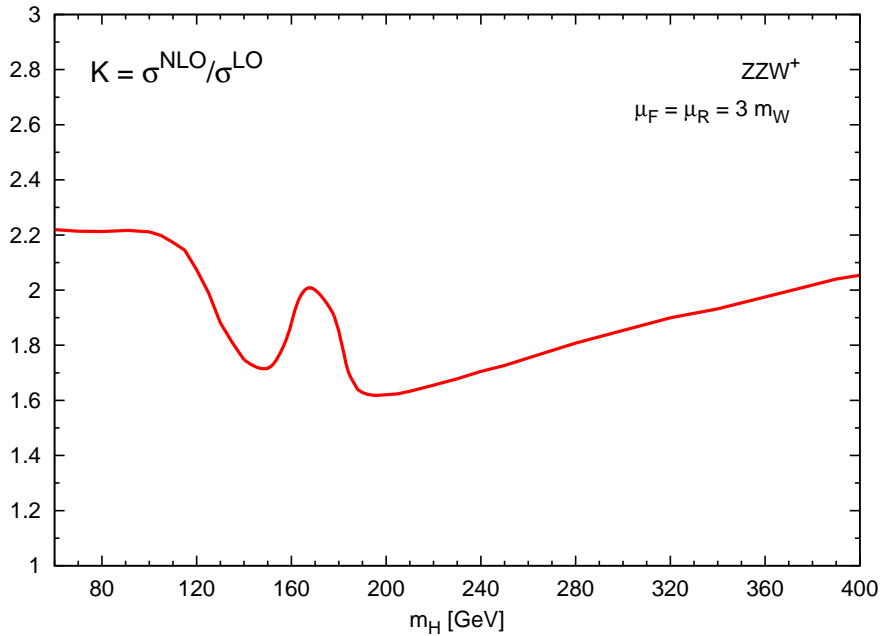
Figure 5.6: *Higgs mass dependence of the cross section at LO and NLO for the ZZW$^+$ production at the LHC within the cuts of Eq. (5.3). The plotted cross sections effectively include the branching ratios of the W- and Z-bosons for decays into electrons and/or muons.*

Figure 5.7: *Higgs mass dependence of the K-factor for ZZW$^+$ production at the LHC within the cuts of Eq. (5.3).*

for the ZZW processes as shown in Fig. 5.7. In more detail, in the ZZW$^+$ production, the maximal K-factor for Higgs masses with almost no Higgs contribution to the cross section is K $\simeq$ 2.2. For large cross sections, i.e. large Higgs graph effects, on the other side, the K-factor is minimal and only amounts to K $\simeq$ 1.6. Therefore, K-factors for ZZW$^+$ production are in total a little bit larger compared to the ones in the WWZ production.

Being a related process, the behavior found for the ZZW$^-$ production is very similar to the one found in ZZW$^+$ production concerning cross sections as well as K-factors. Specifically, the LO and NLO cross sections reflect the Higgs branching ratio of $H \to ZZ$ and the Higgs contribution leads to a reduction of the K-factor.

5.3   Scale dependence

A very important topic in the calculation of NLO corrections is the estimate of the remaining theoretical uncertainties due to higher order corrections. In the majority of calculations, the difference of the cross section under variation of the factorization and renormalization scale is considered since these scales are unphysical and the real cross section should not depend on the choice of them. In the ideal case, the scale dependence of the leading order cross section is larger than the scale dependence of the next-to-leading order cross section, which is larger than the scale dependence of the next-to-next-to-leading order cross section and so on. In this sense, the scale dependence can, thus, be taken as a measure of the precision of the prediction. Unfortunately, this estimate merely gives an indication and by no means can be regarded as the true theoretical uncertainty on the cross section and other observables. Nonetheless, it is worthwhile to analyze the scale dependence for the NLO cross section and try to give at least a rough picture on the remaining uncertainty due to neglected higher order corrections. This will be done in this section for both the ZZW and the WWZ production modes.

In Figs. 5.8, 5.9, and 5.10, the factorization (μ_F) and renormalization scale (μ_R) dependence of the LO and the total NLO cross section is shown for all the different processes under investigation. At LO, triple vector boson production is a purely electroweak process and hence no renormalization scale dependence appears in the calculation. Therefore, the scale variation is only due to the variation of the factorization scale in the parton distribution functions. The small variation at LO can thus be explained by the fact that the pdfs are determined in a Feynman-x range of small factorization scale dependence. At NLO, the dependence on the scales is more complicated. Since the factorization scale dependence is quite small, the dependence
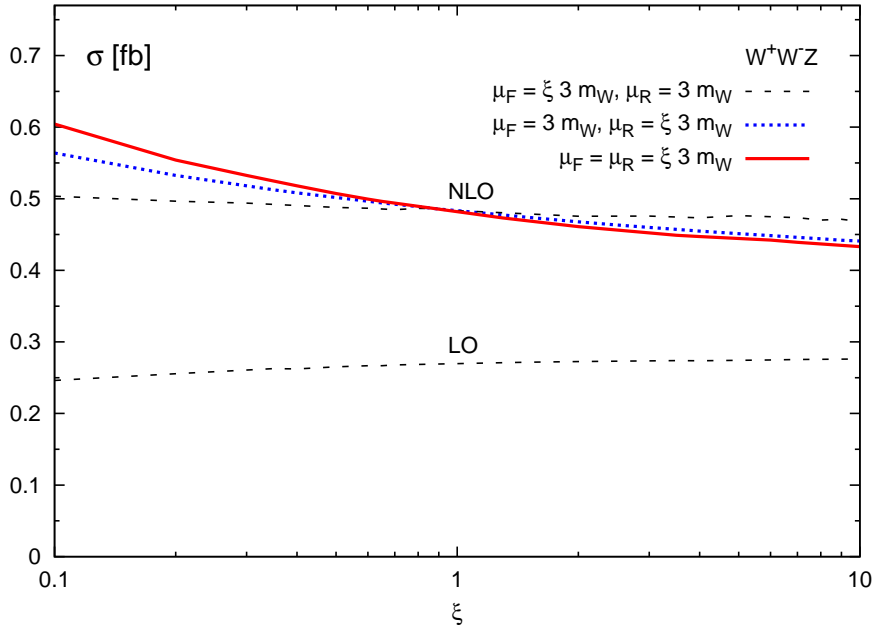
Figure 5.8: Scale dependence of the LO and NLO cross section for 4-lepton final states within the cuts of Eq. (5.3). Variation of the renormalization and/or the factorization scale for the W^+W^-Z production.

under variation of $\mu = \mu_R = \mu_F$ is almost completely dominated by the dependence on the renormalization scale and shows the expected $\alpha_s(\mu_R)$ dependence, which means that for large scales cross sections are smaller.

For a more detailed analysis, the different contributions to the total NLO cross section are shown in Figs. 5.11 and 5.12 for the example of $W^+W^-Z + X$ production. A qualitatively similar behavior is found for all triple vector boson processes investigated here. In Fig. 5.11, the finite part of the virtual contributions (the $\tilde{M}_V$ term in Eq. (3.27)), combined with the Born squared terms (including the LO contribution), shows a remarkably small dependence under simultaneous variation of the renormalization and the factorization scale. This can be understood by a comparison with the factorization scale induced LO variation given in Fig. 5.9. Under variation of μ_F, the virtual contribution shows the same behavior as the LO cross section, which means that the cross section decreases for small scales. Under variation of μ_R, on the other hand, the finite part of the virtual contribution increases for small scales, due to the increase in α_s. These two opposing behaviors cancel to some extent and lead to the observed curve in Fig. 5.11.

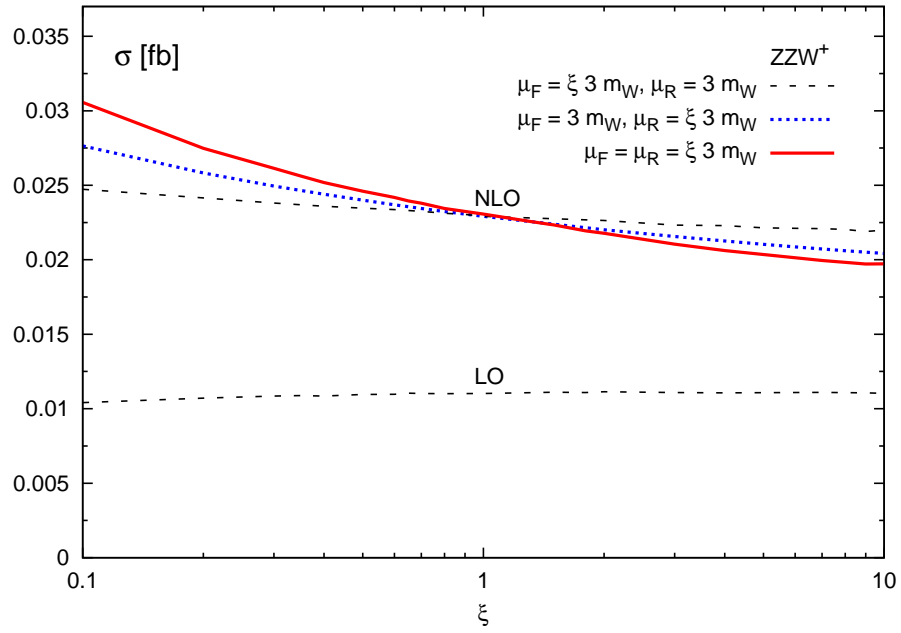For the subtracted real emission contributions and the finite collinear remnants,

Figure 5.9: Scale dependence of the LO and NLO cross section for 5-lepton final states within the cuts of Eq. (5.3). Variation of the renormalization and/or the factorization scale for the ZZW$^+$ production.
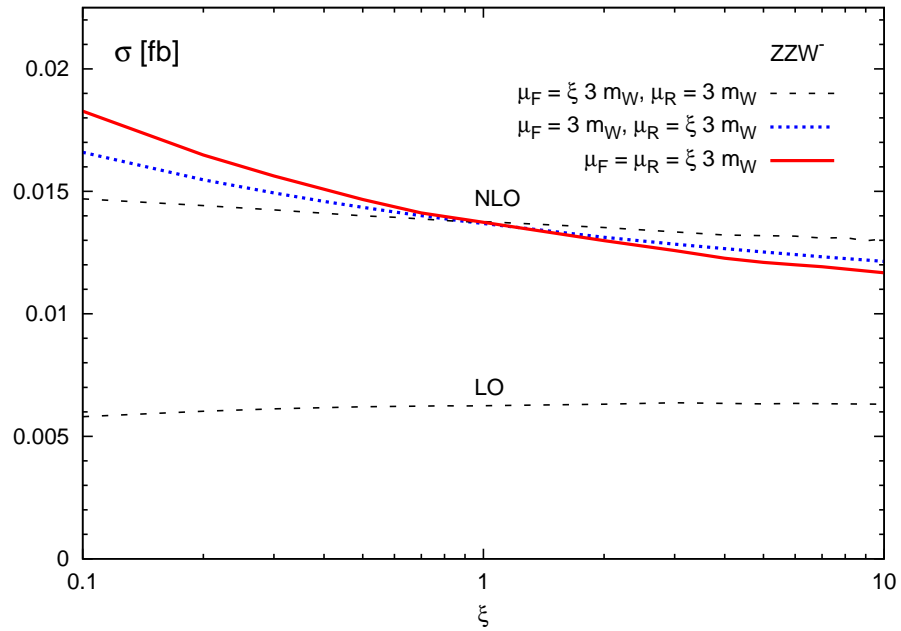

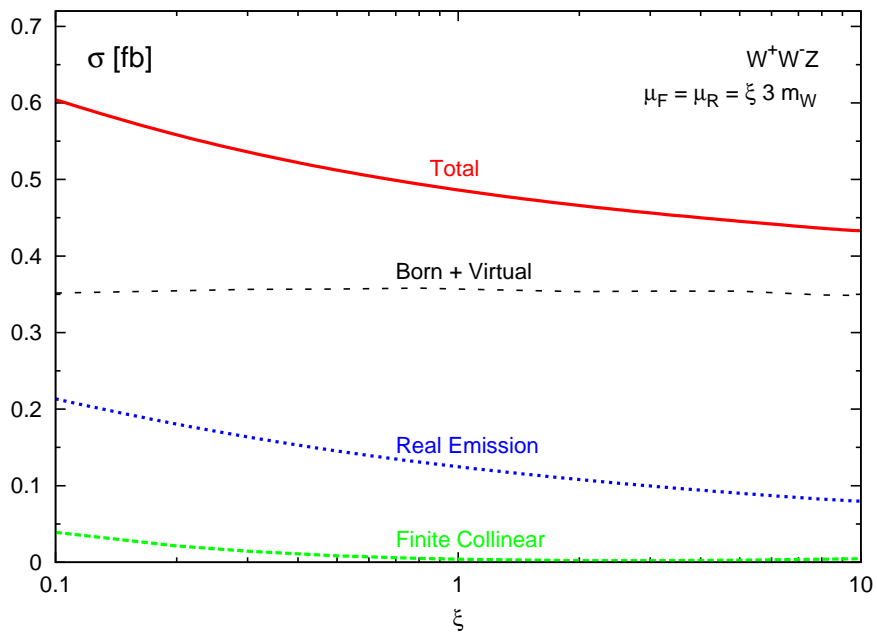Figure 5.10: Same as in Fig. 5.9 but for the ZZW$^-$ production.

Figure 5.11: Scale dependence of the different contributions to the NLO cross section for $pp \rightarrow W^+W^-Z + X$ production at the LHC within the cuts of Eq. (5.3). The plotted cross sections effectively include the branching ratios of the W- and Z-bosons for decays into electrons and/or muons.
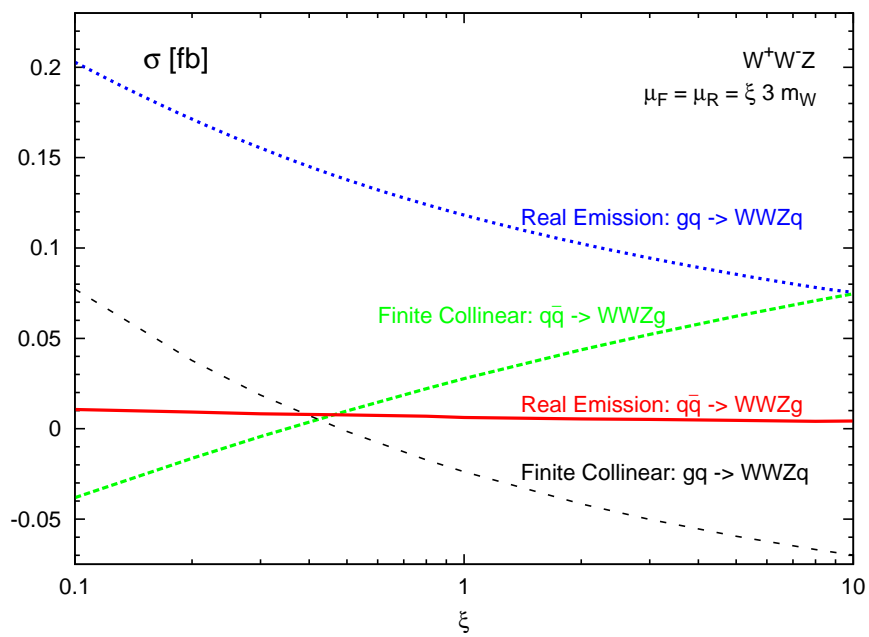
Figure 5.12: Scale dependence of the subtracted real emission and additional finite collinear contributions to the NLO cross section for $pp \rightarrow W^+W^-Z + X$ production at the LHC within the cuts of Eq. (5.3). The plotted cross sections effectively include the branching ratios of the W- and Z-bosons for decays into electrons and/or muons.

the analysis of the scale dependence is somewhat more involved, since the finite collinear terms depend non-trivially both on the factorization and on the renormalization scale. Moreover, these contributions include gluon-induced subprocesses like $ug \to \mathrm{WWZ}\,u$ in addition to the quark-induced ones such as $u\bar{u} \to \mathrm{WWZ}\,g$. The gluon-induced finite collinear terms are exactly given by the A(x) terms in the modified parton distribution functions in Eq. (3.25). In Fig. 5.12, the real emission contributions and the finite collinear remnants are separately shown for each of these classes of subprocesses. The variable `creal` entering the formulas of the quark induced finiter collinear remnants in Eq. (3.25) is chosen as $\texttt{creal} = \frac{\pi^2}{3} - 5$.

In the finite collinear terms, the quark- and gluon-induced contributions show opposite behavior under variation of the scale. Due to these cancellations, the resulting scale dependence and the size of their overall contribution is quite small. However, the real emission contributions arising from the quark-induced subprocesses are almost constant for the scales shown here, while a comparatively large scale variation is observed in the real emission terms of the gluon-induced contributions. These are responsible for the large scale dependence of the overall real emission term in Fig. 5.11. This is not surprising since gluon-initiated subprocesses open up for the first time at NLO, and therefore, a LO-type scale dependence is expected.

Gluon-induced subprocesses are also responsible for a large fraction of the K-factor. For instance, the K-factor for ZZW^+ production at $\mu_F = \mu_R = 3\,m_W$ is K = 2.1, whereas the K-factor without gluon-initiated subprocesses only amounts to K = 1.5.

In the analysis presented here also other scale choices, as for example the invariant three vector boson mass and the minimal E_T of the three vector bosons have been tested. However, neither in the cross section nor in the distributions an improved scale dependence has been found. This again can be understood since the dominating scale dependence comes from the gluon-induced subprocesses, which have to be considered as LO processes.

5.4   Phase space dependence of the K-factor

In the program described in this thesis, observables for real final state particles, i.e. charged leptons and jets, are calculated. These are available in form of differential distributions. Neutrinos on the other hand, can not directly be detected in a detector and lead to missing transverse momentum. For all processes studied, the size of NLO QCD corrections shows a strong phase-space dependence. Thus differential K-factors, defined as the NLO differential cross section divided by the LO differential cross section,
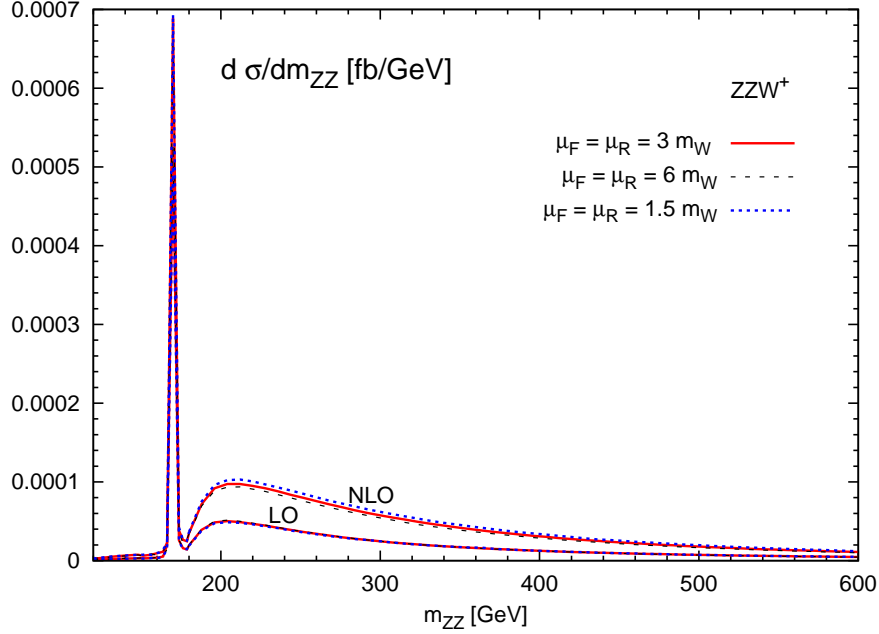
Figure 5.13: *Differential cross section for the $\ell^+\ell^-\,\ell^+\ell^-$ invariant mass for $\mu_F = \mu_R = \frac{1}{2} \times (3\,m_W)$, $(3\,m_W)$, and $2 \times (3\,m_W)$ in ZZW$^+$ production at the LHC. The Higgs boson mass used in the plot is $m_H = 170$ GeV. The plotted cross sections effectively include the branching ratios of the W- and Z-bosons for decays into electrons and/or muons.*

$$\mathrm{K}(x) = \frac{d\sigma^{NLO}/dx}{d\sigma^{LO}/dx}, \tag{5.6}$$

can show a considerable variation.

The Higgs contribution is one reason for such a strong phase space dependence. In Fig. 5.13, for instance, the invariant ZZ mass distribution in ZZW$^+$ production is shown for a Higgs boson mass of $m_H = 170$ GeV. For all three different scale choices $\mu_F = \mu_R = \frac{1}{2} \times (3\,m_W)$, $(3\,m_W)$, and $2 \times (3\,m_W)$, the same characteristic shape of differential distributions is observed. In particular, the Higgs boson contribution gives rise to the narrow peak at about $m_{ZZ} = 170$ GeV. At tree-level, the only Feynman graph with a Higgs boson exchange is the one depicted in Fig. 5.3b, where the Higgs boson decays into two Z-bosons. This graph dominates near $m_{ZZ} = m_H$, i.e. when the intermediate Higgs boson becomes on-shell. At LO the different curves
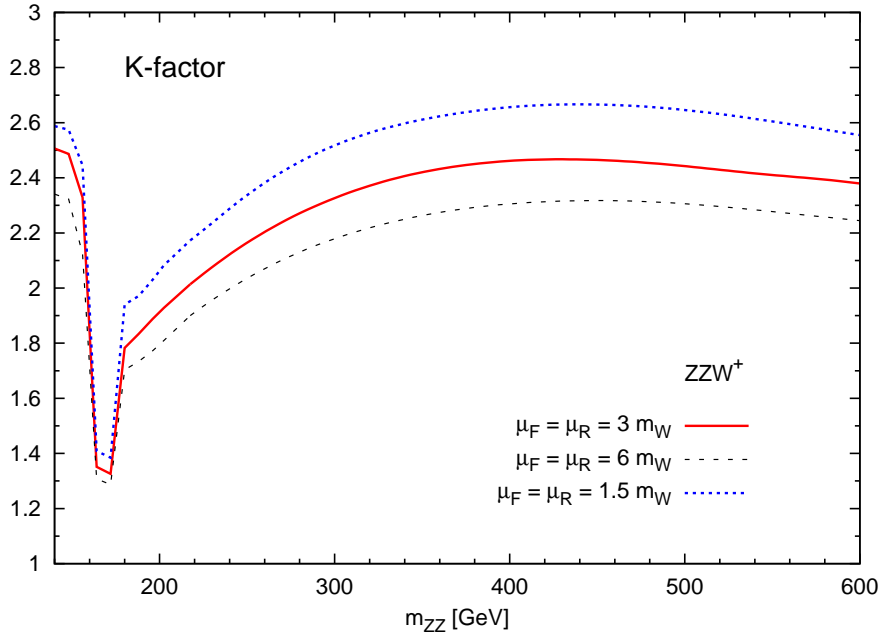
Figure 5.14: *The differential K-factor ratio as defined in Eq. (5.6) is shown for three different scale choices.*

corresponding to the three scale choices lie almost on top of each other and scale variations are at the level of a few percent only. At NLO however, the variation with the three different scales depends on the phase space region. For values of m_{ZZ} near the Higgs resonance, the scale dependence is around 1% and thus very small. For large values of m_{ZZ} on the other hand, increasing and lowering the scale by a factor of two can even lead to changes in the differential cross section of about 10%. Hence, the scale dependence at NLO is reduced in the regions where the Higgs graph dominates.

In Fig. 5.14, the differential K-factor is plotted. Since the QCD corrections to the Higgs boson contribution itself increase the cross section only by about 30% [65–69], there is a pronounced dip in the differential K-factor at about the Higgs boson mass. At this point the K-factor is, as anticipated, between 1.3 and 1.4 depending on the scale choice. In other phase space regions, where the Higgs graph is less important, the K-factor is almost twice as large. This influence of the NLO QCD corrections on the shape of differential distributions is a very strong reason for the necessity to include Higgs contributions into the calculations. Furthermore it gives a first hint that for triple vector boson production at the LHC, leading order distributions can not simply be multiplied by an overall K-factor to obtain NLO distributions.

70

In Figs. 5.15, 5.16, 5.17 and 5.18, two more examples of the phase-space dependence of the NLO corrections are given for W^+W^-Z production at $m_H = 120$ GeV. Figs. 5.15 and 5.16 show the transverse-momentum distribution and the K-factor of the highest-p_T charged lepton while in Figs. 5.17 and 5.18 the same for the charged lepton of lowest-p_T is depicted. Variations of the K-factor of almost 100% are observed for the highest-p_T lepton while for the lowest-p_T lepton we have variations up to 30% when considering "inclusive" event samples.

This p_T-dependence of the K-factors can be traced to the kinematics of the real emission contributions. The rise is mostly due to events with high p_T jets which are recoiling against the leptons. Imposing a veto on jets with $p_T > 50$ GeV leads to a fairly flat K-factor which, in addition, is close to unity for the lepton p_T distributions (curves labeled "with jet veto" in Figs. 5.16 and 5.18). Similar effects had previously been observed for vector boson pair production at the LHC [24–27].

5.5   Pdf uncertainties

Another type of uncertainties apart from those coming from neglected higher order corrections in the QCD perturbation series are due to the parton distribution functions. In this work, the best fits from the CTEQ collaboration have been used for LO and NLO calculations.

In the fit of the NLO pdfs twenty free parameters enter. In order to get an estimate on the uncertainty of these sets of parton distribution functions, the CTEQ collaboration has provided forty pdf sets which correspond to the 1σ endpoints of the principal axes of the twenty dimensional error ellipsoid, in the twenty dimensional parameter space. The estimated error on the total cross section can then be obtained from the forty pdf sets via the formula

$$\Delta\sigma = \frac{1}{2}\sqrt{\sum_{i=1}^{20}\big(\sigma(2i-1) - \sigma(2i)\big)^2}. \tag{5.7}$$

In Fig. 5.19 the results for the LO and the NLO cross section obtained with the best fit pdfs are plotted together with the uncertainty derived from runs with the forty different pdf sets according to Eq. (5.7). This error estimate has been performed for five different scales and leads to a few per cent inaccuracy. Thus the remaining pdf uncertainty at NLO is not negligible but well below the scale uncertainty of the NLO cross section.
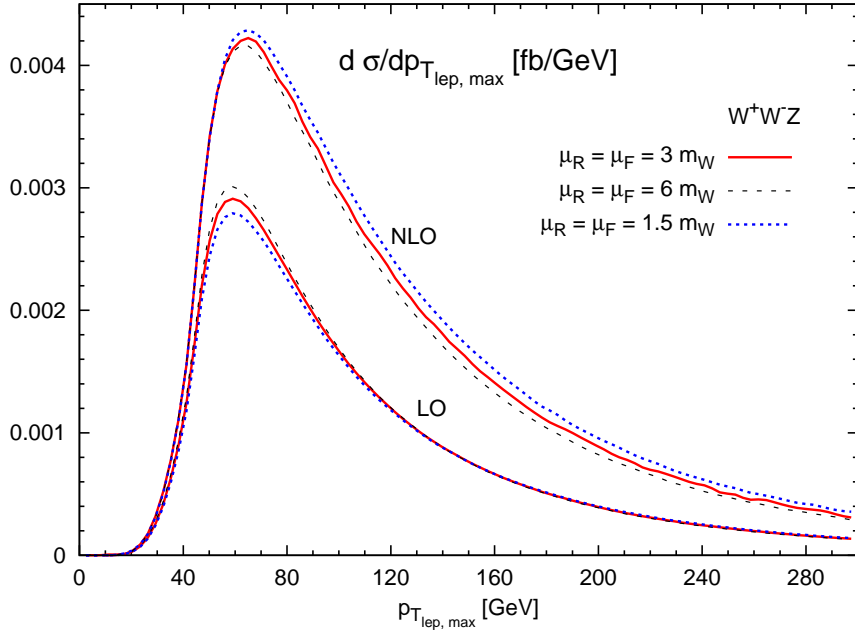
Figure 5.15: *Differential cross section for the highest-p_T lepton for $\mu_R = \mu_F = 3\,m_W$, $\mu_R = \mu_F = 2 \cdot (3\,m_W)$, and $\mu_R = \mu_F = 0.5 \cdot (3\,m_W)$ in W^+W^-Z production at the LHC. The plotted cross sections effectively include the branching ratios of the W- and Z-bosons for decays into electrons and/or muons.*
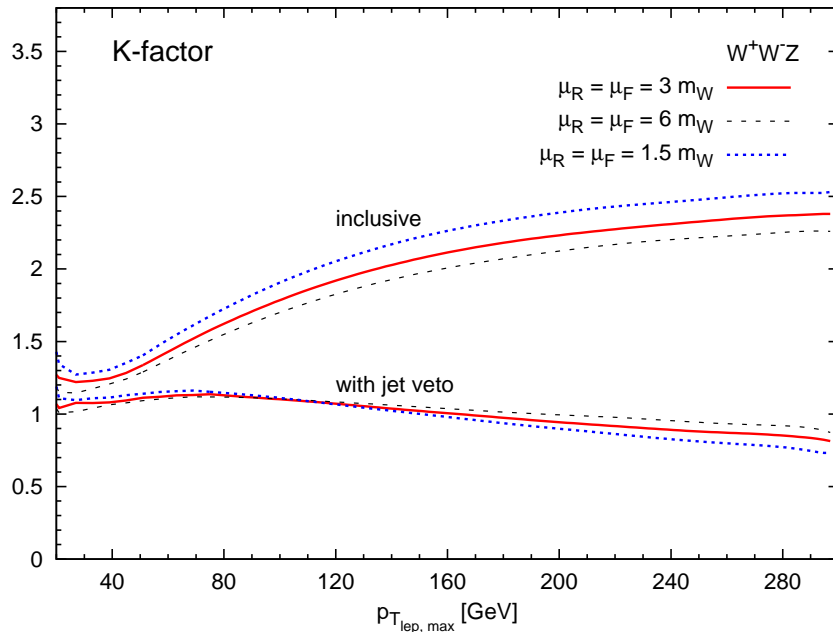

Figure 5.16: *Differential K-factor, as defined in Eq. (5.6) for inclusive events without jet cuts and also for a veto on jets with $p_{T,\text{jet}} > 50$ GeV.*

Figure 5.17: *Differential cross section for the lowest-p_T lepton for $\mu_R = \mu_F = 3\,m_W$, $\mu_R = \mu_F = 2 \cdot (3\,m_W)$, and $\mu_R = \mu_F = 0.5 \cdot (3\,m_W)$ in W^+W^-Z production at the LHC. The plotted cross sections effectively include the branching ratios of the W- and Z-bosons for decays into electrons and/or muons.*

Figure 5.18: *Differential K-factor, as defined in Eq. (5.6) for inclusive events without jet cuts and also for a veto on jets with $p_{T,\mathrm{jet}} > 50$ GeV.*
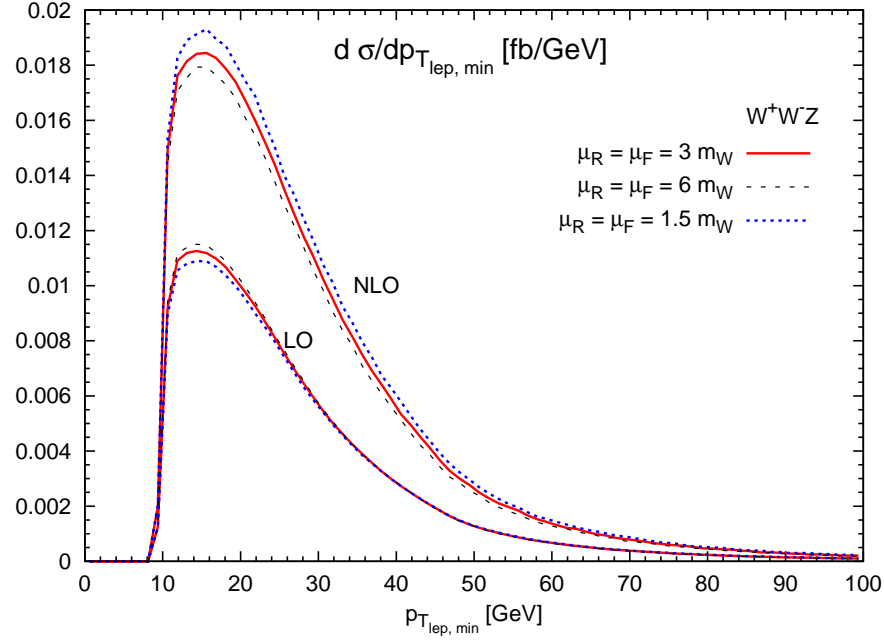
Figure 5.19: *Estimate on the uncertainty induced by the pdfs for the W^+W^-Z production at the LHC. The data obtained in this figure has been produced with the variables and cuts given in Eqs. (5.1) and (5.3). The plotted cross sections effectively include the branching ratios of the W- and Z-bosons for decays into electrons and/or muons.*

Chapter 6:

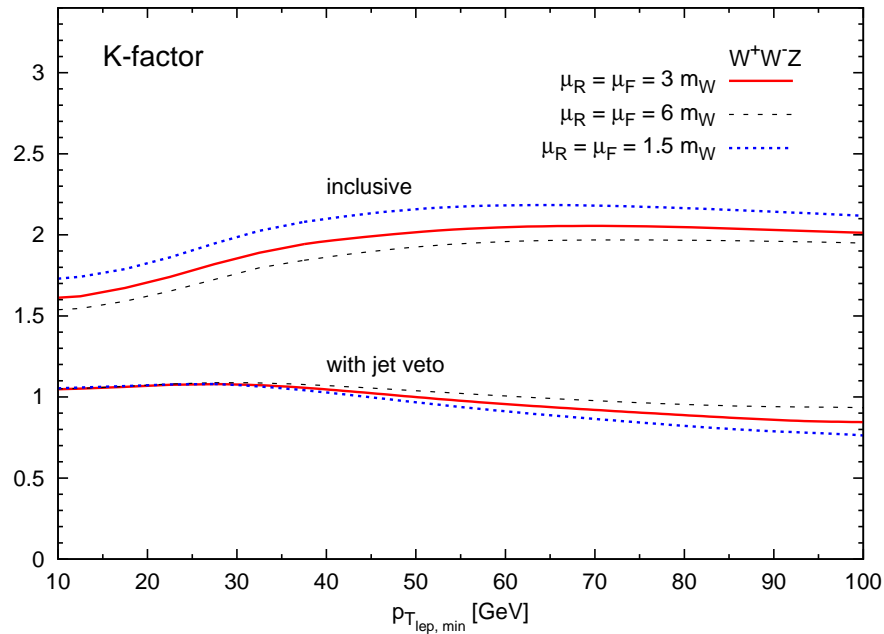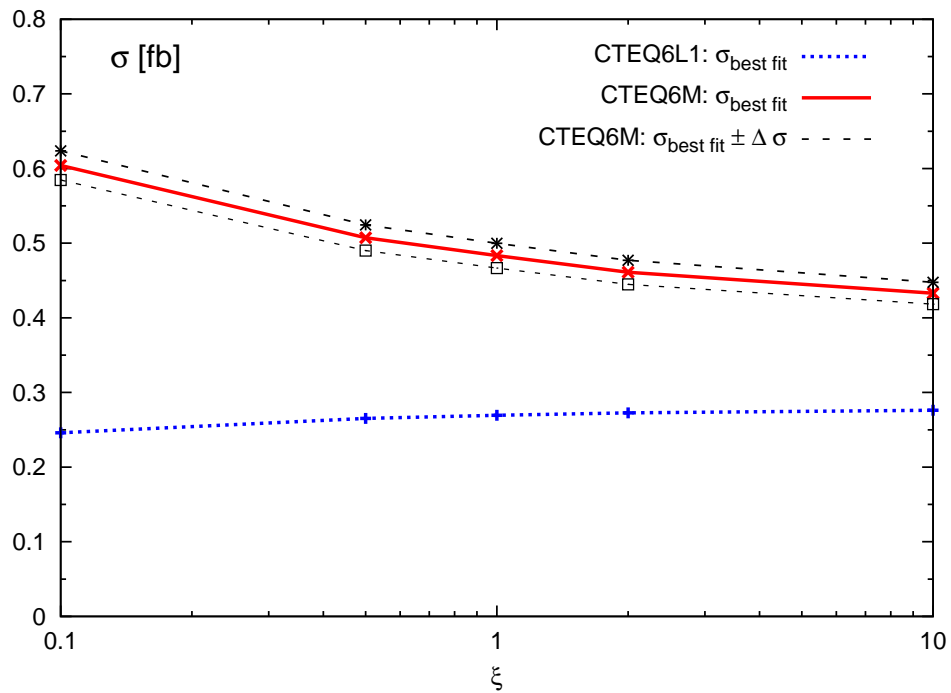# Conclusions and Outlook

With the start of the LHC a trove of new data is anticipated, which can be used to search for new physics and also to further probe the Standard Model. For the interpretation of these data, precise predictions for both the desired signal processes and backgrounds are needed, and this necessitates the calculation of next-to-leading order QCD corrections. In order to determine cross sections for non-trivial acceptance cuts, it is most useful to cast these NLO calculations into fully flexible Monte-Carlo programs which can calculate cross sections as well as distributions.

The simulation of triple vector boson production at the LHC is important for two reasons. These processes are a Standard Model background for new-physics searches which are characterized by multi-lepton final states, and secondly they are sensitive to quartic electroweak couplings.

In this thesis the results on the NLO QCD corrections to the full $2 \to 6$ processes $pp \to \nu_e \, e^+ \, \mu^- \, \bar{\nu}_\mu \, \tau^- \, \tau^+$, $pp \to e^- \, e^+ \, \mu^- \, \mu^+ \, \nu_\tau \, \tau^+$, and $pp \to e^- \, e^+ \, \mu^- \, \mu^+ \, \tau^- \, \bar{\nu}_\tau$ or any other combination of leptons from three distinct families are presented. All resonant and non-resonant matrix elements including intermediate Higgs contributions as well as the spin correlations of the final state leptons are considered in the calculation. For simplicity, any identical lepton effects which might appear when using the results for final states with leptons from one or two generations only, are neglected. Furthermore, the CKM matrix has been approximated by the unit matrix and any fermion mass effects are neglected. However, the resulting error on the total NLO cross section made by these approximations is estimated to be of the order of a few percent only.

In order to deal with infrared divergencies arising in the real emission and the virtual contribution, the Catani-Seymour subtraction algorithm [47, 48] has been applied. Virtual contributions are calculated using Fortran subroutines derived in Ref. [14, 57]. The four-point integrals are computed using the usual Passarino-Veltman tensor reduction [58], whereas five-point integrals necessitate the recursion relations elaborated by Denner and Dittmaier in Refs. [59, 60] in order to give numerically stable

results. Moreover, since the evaluation of one-loop diagrams with five external legs is quite time consuming, a trick has been applied to reduce the magnitude of the pentagon contribution to a numerically less challenging level.

Concerning the subtracted real emission contribution, efficiency also is an issue. In the WWZ production, the total number of real emission Feynman diagrams which need to be calculated for one specific phase space point amounts to 4992 and to 3276 in the ZZW production modes. In addition, Born matrix elements appearing in the subtracted dipoles are evaluated for two different kinematics. Summing them up, 1440 graphs are computed in the WWZ case and 836 in the ZZW processes for each phase space point. However, the time needed for the evaluation of these huge numbers of Feynman graphs can be reduced considerably by identifying building blocks which appear in various diagrams and only calculate them once per phase space point.

All parts of the code have been carefully checked. In particular, LO cross sections and distributions have been compared with MADEVENT [51–53] and HELAC [54–56] for various Higgs masses. Furthermore, Ward identity tests for the virtual contributions have been implemented and the cancellation of divergences in the real emission against the counter-terms, as given by Catani and Seymour [47,48] has been checked. As a final and very important test, a comparison with the already published results for the production of on-shell gauge bosons without leptonic decays of Ref. [11] has been performed.

Although, in principle, VBFNLO allows for the calculation of observables for the Tevatron as well as for the LHC, in this thesis only results for the LHC have been presented due to the smallness of cross sections at the Tevatron center of mass energy. First determinations of cross sections, distributions and K-factors for the LHC are then given in Chapter 5.

The scale dependence of the NLO cross section is substantially larger than the variation observed for the LO results. This can be quantified by increasing and lowering the renormalization and factorization scale by a factor of two around $\mu = 3 \cdot m_W$ as central value. At LO the scale dependence is very small with a variation of less than $\pm 1\%$, whereas at NLO variations of $\pm 5\%$ appear. The NLO uncertainties which are indicated by the scale dependence are, thus, typical for a NLO QCD prediction, while the LO case must be considered as anomalously small, due to the absence of initial-state gluon-induced subprocesses. Indeed, the tri-boson cross sections provide another example where the scale variation of a LO cross section does not give a good estimate for the corrections due to higher order effects.

The large K-factors (of order K = 2 and even larger in some phase space regions) demonstrate the importance of including the NLO QCD corrections on top of the LO predictions.

The differential K-factors for several distributions for both of these processes are highly dependent on the Higgs boson mass. In general it is observed that the larger the contributions from the Higgs boson are, the smaller is the K-factor. In the case of the W^+W^-Z production, with $\mu_F = \mu_R = 3\, m_W$ for instance, the K-factor decreases from K = 1.6 for a Higgs boson mass of 120 GeV to K = 1.4 for a Higgs boson mass of 150 GeV. At the same time the LO cross section increases by more than a factor of two. Therefore, in all simulations, the Higgs boson contribution has to be taken into account in order to obtain a valid prediction for the cross sections and the K-factors. Besides these large K-factors, also a strong phase space dependence of the size of the NLO corrections has been found which shows that a mere multiplication of distributions by an overall K-factor is not sufficient.

Another source of uncertainties besides the ones from higher order corrections enter the calculation in form of the parton distribution functions. In order to estimate these uncertainties, forty different pdf sets are provided by the CTEQ collaboration. Performing the error analysis as suggested in Ref. [62], an uncertainty of around 5% is expected for the total NLO cross sections due to pdf errors.

Summarizing, the cross sections at NLO QCD accuracy for $pp \rightarrow W^+W^-Z + X$, $pp \rightarrow ZZW^+ + X$, and $pp \rightarrow ZZW^- + X$ processes at the LHC are of the order of 15 fb (ZZW^-) to 150 fb (W^+W^-Z). Including the decays of the vector bosons this corresponds to cross sections of $\sigma(pp \rightarrow \ell_1^- \ell_1^+ \ell_2^- \ell_2^+ \ell_3^- \bar{\nu}_{\ell_3}) = 0.015$ fb, $\sigma(pp \rightarrow \ell_1^- \ell_1^+ \ell_2^- \ell_2^+ \nu_{\ell_3} \ell_3^+) = 0.023$ fb, and $\sigma(pp \rightarrow \nu_{\ell_1} \ell_1^+ \ell_2^- \bar{\nu}_{\ell_2} \ell_3^- \ell_3^+) = 0.5$ fb with $\ell_i = e, \mu$. Hence, for an integrated luminosity of 300 fb^{-1} these results translate into a few to a few hundred clean leptonic events. The estimated uncertainty on these numbers stemming from approximations in the calculation, neglected higher order effects, and parton distribution functions are in the range of 10% and thus modest.

However, due to the sizeable K-factors as large as K = 2 the effects of higher order corrections still remain somewhat unclear. The only hint of the real size of these corrections comes from the known next-to-next-to-leading order results for the Drell-Yan production [70–74]. These suggest in most phase space regions modest modifications of the NLO results at the few percent level.

77

Appendix A:

Catani-Seymour algorithm for tri-boson production

In order to deal with the collinear and soft divergencies arising in the computation of the real emission and virtual contributions to the total NLO cross section, the Catani-Seymour algorithm presented in Refs. [47, 48] is used. A general outline of this method is already given in Section 3.2.1. The purpose of this chapter, however, is to present detailed information and exact expressions for the dipoles, the integrated dipoles and the finite collinear terms as needed for the actual implementation into a numerical computer program. Results are comprised in Sections A.1 through A.3. In addition, Section A.4 lists the integrals used for the derivation of the finite collinear terms in Section A.3.

A.1 Real emission and Catani-Seymour dipoles

In the program VBFNLO, the real emission calculation is divided into six pieces, which correspond to six different types of subprocesses. Two of them are subprocesses with a final-state gluon and there are four subprocesses with an initial-state gluon. Since all of them are related by crossing symmetries only one subroutine to calculate the matrix elements is needed. The different subprocesses of the real emission calculation are listed in the first paragraph of this section.

Furthermore, Born matrix elements with different kinematics are needed in the calculation of the dipoles acting as local counter terms for the real emission contribution. Part 2 of this section lists all necessary dipoles and covers the relevant Born matrix elements as well as some details on the tilde kinematics. Finally, at the end of this section a brief description on the actual implementation of the subtracted real emission cross sections is given.
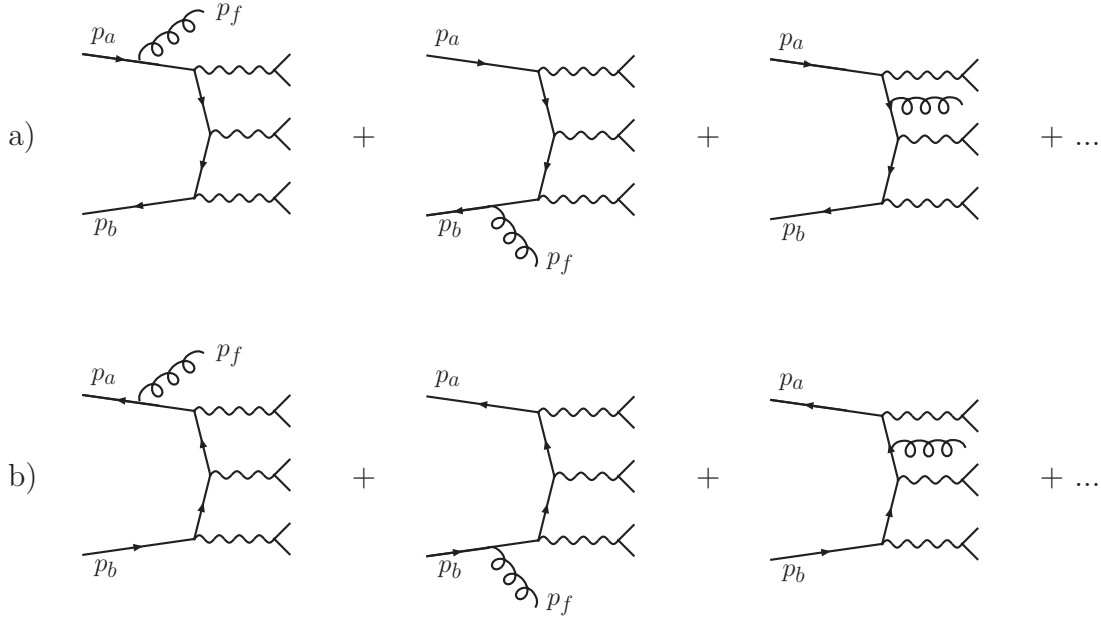
Figure A.1: *Illustration of the two quark induced subprocesses of the real emission calculation.*

A.1.1 The subprocesses in the real emission calculation

The cross section of the real emission contribution is a sum of different subprocesses. Each of them consists of 546 Feynman diagrams in the ZZW case and 416 Feynman diagrams in the WWZ case, respectively.

There are two kinds of subprocesses with a gluon in the final state:

a) In the first subprocess, $q(p_a)\,\bar{Q}(p_b) \to \text{VVV} + g(p_f)$, a quark from the first proton with momentum $p_a = x_a P_1$ and an antiquark from the second proton with momentum $p_b = x_b P_2$ interact, producing six leptons and one gluon. This final-state gluon can either be emitted from the initial-state quark $q(p_a)$, the initial-state antiquark $\bar{Q}(p_b)$, or from an internal quark line. Examples for all three possibilities are given in Fig. A.1a. The last case does not lead to any divergencies, whereas a counter term is needed for each of the two other cases.

b) Some sample diagrams for the second subprocess with a gluon in the final state, $\bar{Q}(p_a)\,q(p_b) \to \text{VVV} + g(p_f)$, are depicted in Fig. A.1b. In this case, the initial- and final-state particles are the same as before. The only difference is that the antiquark $\bar{Q}(p_a)$, is part of the first proton, whereas the quark $q(p_b)$ is emitted from the second proton. The matrix elements of this subprocess

can easily be calculated with the same routine as before by interchanging the momenta of the initial-state particles. For the cross section, however, it is of fundamental importance, that the antiquark with momentum p_a is part of the first proton and the quark with momentum p_b is part of the second proton.

The other subprocesses are gluon induced processes with a quark or an antiquark in the final state. Here, the gluon can either be part of the first or the second proton. Further, the second initial-state parton can either be a quark or an antiquark. Therefore, there are four different types of subprocesses with a gluon in the initial state:

c) The first gluon induced subprocess $g(p_a) \, q(p_b) \rightarrow \mathrm{VVV} + Q(p_f)$ is schematically given in Fig. A.2c. Here a gluon $g(p_a)$ stemming from the first proton interacts with a quark $q(p_b)$ coming from the second proton. The final-state quark can become collinear to the initial-state gluon. This is the only source of infrared divergencies for this class of diagrams. Therefore, only one dipole is needed as counter term. The matrix elements of this subprocess can be obtained by crossing from the matrix elements of the processes with a final-state gluon. These matrix elements are then folded with the corresponding gluon and quark distribution functions.

d) The second subprocess with an initial-state gluon, $g(p_a) \, \bar{Q}(p_b) \rightarrow \mathrm{VVV} + \bar{q}(p_f)$, has similar features as the previous one. The only difference is that the quark $q(p_b)$ is replaced by an antiquark $Q(p_b)$ (See Fig. A.2d). Again, only one counter term is needed to absorb the infrared divergencies and the matrix elements can be obtained with the same subroutine as above by a simple crossing.

e) Sample diagrams for the third subprocess with a gluon in the initial state, $q(p_a) \, g(p_b) \rightarrow \mathrm{VVV} + Q(p_f)$ are given in Fig. A.2e. In this case the gluon is part of the second proton and the quark stems from the first proton. All other features of this process are the same as for the gluon induced subprocesses described before.

f) The last subprocess, $\bar{Q}(p_a) \, g(p_b) \rightarrow \mathrm{VVV} + \bar{q}(p_f)$, again needs only one dipole to absorb infrared divergencies. Compared to the previous subprocess, the quark $q(p_a)$ is replaced by an antiquark $\bar{Q}(p_a)$. Some sample diagrams for this case are shown in Fig. A.2f.

The total cross section of the real emission contribution is obtained by summing over all different subprocesses. These consist of the subprocesses given in Figs. A.1 and
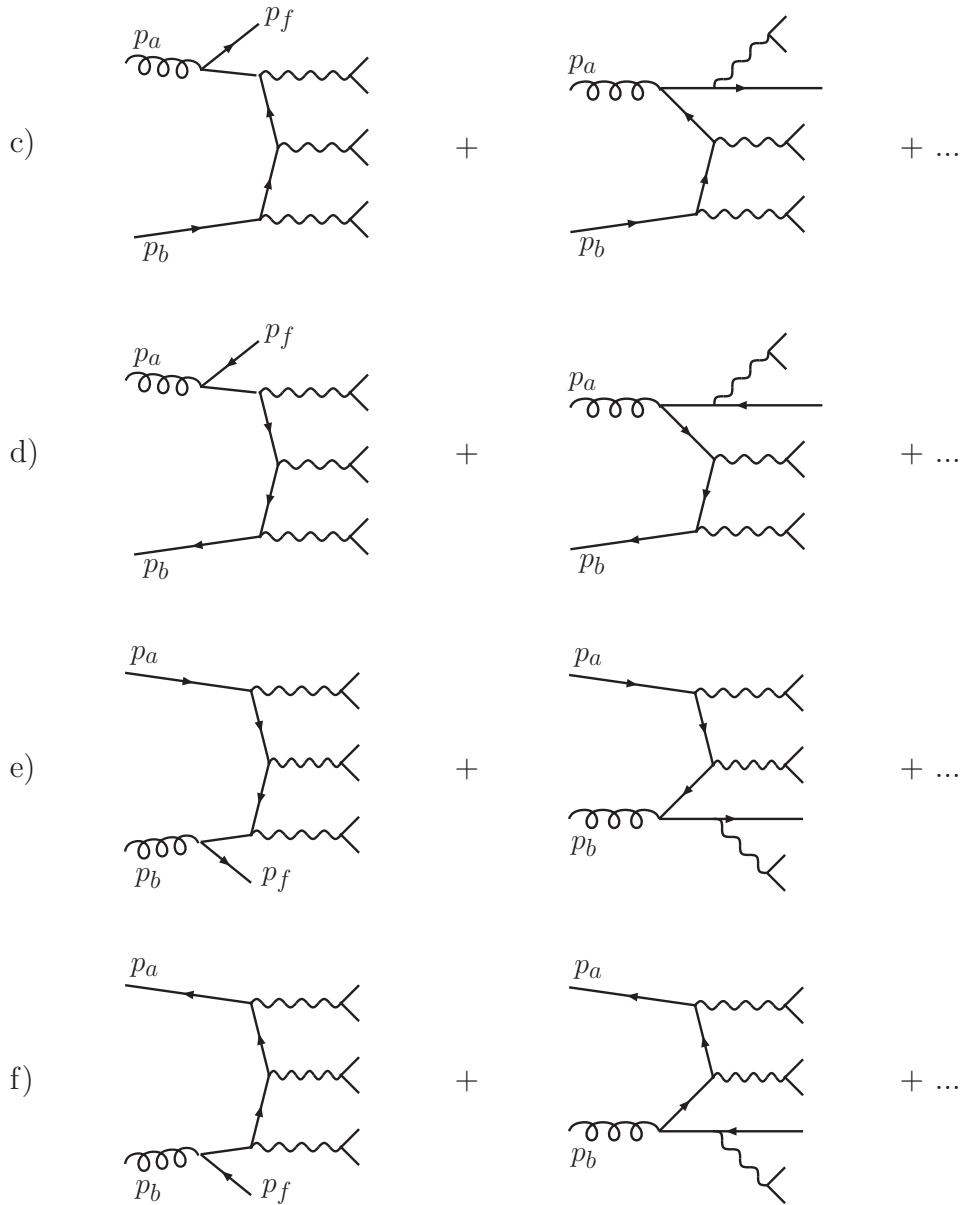
Figure A.2: *Illustration of the four gluon induced subprocesses of the real emission calculation.*

A.2, if all possible flavor combinations are taken into account. Choosing the CKM matrix to be the unit matrix and only taking into account light quarks, where the massless approximation is reasonable, we find for the W^+W^-Z production $q = Q$ with $q = u, d, c, s$. For the two charged triple vector boson processes on the other hand, the flavor changes once along the quark line, thus, $q = u, c$ and $Q = d, s$ for the ZZW^+ production and $q = d, s$ and $Q = u, c$ for the ZZW^- production. Hence, there are in total 12 subprocesses for the ZZW processes and 24 in case of the WWZ production.

A.1.2 Catani-Seymour dipoles

For all different types of subprocesses, there are corresponding dipoles. The subprocesses depicted in Fig. A.1 need two dipoles absorbing their infrared divergencies. For the subprocesses illustrated in Fig. A.2, i.e. the ones with a gluon in the initial state, one counter term is sufficient. The corresponding dipoles for the different types of subprocesses discussed in the previous section are then given below:

a) $q(p_a)\,\bar{Q}(p_b) \to \mathrm{VVV} + g(p_f)$

The first subprocess given in Fig. A.1a, has several sources of infrared divergencies. First, the gluon can become soft and second it can be collinear to the quark or the antiquark. Hence, two counter terms corresponding to emission of the gluon from the upper incoming quark or the lower incoming antiquark are needed.

The dipole for the quark being the emitter and the antiquark the so-called spectator, is given by:

$$
\begin{aligned}
\mathcal{D}^{q(p_a)g(p_f),\bar{Q}(p_b)} =& \frac{1}{2p_a \cdot p_f}\,\frac{1}{x}\,8\pi\,\alpha_s\,C_F\,\delta_{ss'}\,\left[\frac{2}{1-x} - (1+x)\right] \\
&\cdot \left|\,M_{Born}^{q\bar{Q}}(\tilde{k}_1, ... \tilde{k}_6; \tilde{p}_a, p_b)\,\right|^2.
\end{aligned}
\tag{A.1}
$$

Here, $C_F = \frac{4}{3}$ is the color factor, α_s the strong coupling constant, and the Born matrix element appearing here is the one with a quark stemming from the first proton and the antiquark from the second proton, i.e. $M(q(\tilde{p}_a)\,\bar{Q}(p_b) \to \mathrm{VVV})$. It is evaluated with a special tilde kinematic, which transforms an (m+1)-particle phase space into an m-particle phase space. This is achieved by choosing,

$$x = 1 - \frac{p_f \cdot (p_a + p_b)}{p_a \cdot p_b}, \qquad \tilde{p}_a = xp_a, \qquad \tilde{p}_b = p_b, \qquad \tilde{p}_f = 0, \tag{A.2}$$

with p_f being the momentum of the final-state gluon as indicated in Fig. A.1a. In addition to that, all the momenta of the final-state leptons $k_1, ..., k_6$ have to be transformed in order to guarantee energy momentum conservation:

$$\tilde{k}_j^\mu = k_j^\mu - \frac{2k_j \cdot (K + \tilde{K})}{(K + \tilde{K})^2} (K + \tilde{K})^\mu + \frac{2k_j \cdot K}{K^2} \tilde{K}^\mu \tag{A.3}$$

with K and $\tilde{K}$ defined as,

$$K^\mu = p_a^\mu + p_b^\mu - p_1^\mu, \qquad \tilde{K}^\mu = \tilde{p}_a^\mu + p_b^\mu. \tag{A.4}$$

In the case of the antiquark being the emitter and the quark being the spectator, the dipole is given by:

$$\begin{aligned}
\mathcal{D}^{\bar{Q}(p_b)g(p_f),q(p_a)} =& \frac{1}{2p_b \cdot p_f} \frac{1}{x} \, 8\pi\alpha_s \, C_F \, \delta_{ss'} \left[\frac{2}{1-x} - (1+x) \right] \\
& \cdot \left| \, M_{Born}^{q\bar{Q}}(\tilde{k}_1, ...\tilde{k}_6; p_a, \tilde{p}_b) \, \right|^2 .
\end{aligned} \tag{A.5}$$

Here the parameter x is the same as above, since it is invariant under interchange of p_a with p_b. However, the matrix element appearing in Eq. (A.5) has to be evaluated with a different tilde kinematic, defined by choosing

$$\tilde{p}_a = p_a, \qquad \tilde{p}_b = xp_b. \tag{A.6}$$

In addition, all the other momenta of the final-state particles have to be rescaled according to Eq. (A.3) but with a different $\tilde{K}$, given by:

$$\tilde{K}^{\mu} = p_a^{\mu} + \tilde{p}_b^{\mu}. \tag{A.7}$$

The two different kinematics defined until now are the only ones appearing in the calculation of dipoles for Drell-Yan type processes such as the tri-boson production.

b) $\bar{Q}(p_a)\,q(p_b) \to \text{VVV} + g(p_f)$

The second subprocess with a final-state gluon is sketched in Fig. A.1b. The anti-quark is in this case a constituent of the first proton and the quark stems from the second proton. As in the previous case two dipoles are needed to absorb infrared divergencies arising in the calculation of matrix elements with emission of a gluon from either the upper incoming antiquark or the lower incoming quark. Specifically, they are:

$$\mathcal{D}^{\bar{Q}(p_a)g(p_f),q(p_b)} = \frac{1}{2p_a \cdot p_f}\,\frac{1}{x}\,8\pi\,\alpha_s\,C_F\,\delta_{ss'}\,\left[\frac{2}{1-x} - (1+x)\right]$$
$$\cdot \left|\, M_{Born}^{\bar{Q}q}(\tilde{k}_1, ..., \tilde{k}_6; \tilde{p}_a, p_b)\,\right|^2 \tag{A.8}$$

and

$$\mathcal{D}^{q(p_b)g(p_f),\bar{Q}(p_a)} = \frac{1}{2p_b \cdot p_f}\,\frac{1}{x}\,8\pi\,\alpha_s\,C_F\,\delta_{ss'}\,\left[\frac{2}{1-x} - (1+x)\right]$$
$$\cdot \left|\, M_{Born}^{\bar{Q}q}(\tilde{k}_1, ..., \tilde{k}_6; p_a, \tilde{p}_b)\,\right|^2. \tag{A.9}$$

They only differ from the ones given in Eqs. (A.1) and (A.5) by the matrix elements. In contrast to the Born matrix elements above, here the ones with an antiquark coming from the first proton and a quark from the second proton $M(\bar{Q}(\tilde{p}_a)\,q(p_b) \to \text{VVV})$ and $M(\bar{Q}(p_a)\,q(\tilde{p}_b) \to \text{VVV})$, are needed. The tilde kinematics are exactly the same already calculated before. That is, if a gluon is emitted from the upper line, the first transformation, Eqs. (A.2, A.3, A.4), is the one needed, whereas, if a gluon is emitted from the lower line, the second, Eqs. (A.6, A.7), is needed.

c) $g(p_a) \, q(p_b) \to \text{VVV} + Q(p_f)$

The first subprocess with a gluon in the initial state is sketched in Fig. A.2a. Here, only one dipole is necessary to match the singular behavior. Evaluating the formulas given in Refs. [47, 48] for the triple vector boson production at hadron colliders, one obtains:

$$
\begin{aligned}
\mathcal{D}^{g(p_a)Q(p_f),q(p_b)} = {} & \frac{1}{2p_a \cdot p_f} \, \frac{1}{x} \, 8\pi \, \alpha_s \, T_R \, \delta_{ss'} \, \left[1 - 2x \left(1 - x \right) \right] \\
& \cdot \left| \, M_{Born}^{\bar{Q}q}(\tilde{k}_1, ..., \tilde{k}_6; \tilde{p}_a, p_b) \, \right|^2 ,
\end{aligned}
\tag{A.10}
$$

with $T_R = \frac{1}{2}$. The dipole is again proportional to the Born matrix elements, appearing already in Eq. (A.8). In order to speed up the calculation, the numerical results for these matrix elements are stored and can then be reused for the evaluation of this dipole.

d) $g(p_a) \, \bar{Q}(p_b) \to \text{VVV} + \bar{q}(p_f)$

The counter term for the subprocess, depicted in Fig. A.2d is given by:

$$
\begin{aligned}
\mathcal{D}^{g(p_a)\bar{q}(p_f),\bar{Q}(p_b} = {} & \frac{1}{2p_a \cdot p_f} \, \frac{1}{x} \, 8\pi \, \alpha_s \, T_R \, \delta_{ss'} \, \left[1 - 2x \left(1 - x \right) \right] \\
& \cdot \left| \, M_{Born}^{q\bar{Q}}(\tilde{k}_1, ... \tilde{k}_6; \tilde{p}_a, p_b) \, \right|^2 .
\end{aligned}
\tag{A.11}
$$

The Born matrix elements needed here have already been calculated for the dipole in Eq.(A.1).

e) $q(p_a) \, g(p_b) \to \text{VVV} + Q(p_f)$

The dipole taking care of divergencies arising in graphs like Fig. A.2e is given by:

$$
\begin{aligned}
\mathcal{D}^{g(p_b)Q(p_f),q(p_a)} = {} & \frac{1}{2p_b \cdot p_f} \, \frac{1}{x} \, 8\pi \, \alpha_s \, T_R \, \delta_{ss'} \, \left[1 - 2x \left(1 - x \right) \right] \\
& \cdot \left| \, M_{Born}^{q\bar{Q}}(\tilde{k}_1, ... \tilde{k}_6; p_a, \tilde{p}_b) \, \right|^2 .
\end{aligned}
\tag{A.12}
$$

It is very similar to the one above. Since the gluon now is part of the second proton, the tilde kinematic with $\tilde{p}_a = p_a$ and $\tilde{p}_b = x\, p_b$ is needed. Again, the Born matrix elements already appeared before in the calculation of Eq. (A.5) and are reused.

f) $\bar{Q}(p_a)\, g(p_b) \rightarrow \text{VVV} + \bar{q}(p_f)$

Finally, the dipole to get rid of divergencies appearing in the subprocess shown in Fig. A.2f, can be obtained from the one given in Eq. (A.10) by interchanging $a \leftrightarrow b$:

$$
\mathcal{D}^{g(p_b)\bar{q}(p_f),\bar{Q}(p_a)} = \frac{1}{2p_b \cdot p_f}\, \frac{1}{x}\, 8\pi\, \alpha_s\, T_R\, \delta_{ss'}\, [1 - 2x\,(1-x)]
$$
$$
\cdot \left| M_{Born}^{\bar{Q}q}(\tilde{k}_1, ...\tilde{k}_6; p_a, \tilde{p}_b) \right|^2 .
$$
(A.13)

The Born matrix elements already appeared in Eq. (A.9) and are not reevaluated for this dipole. By always storing and reusing matrix elements, a quite significant increase in speed is achieved in the program.

A.1.3 Implementation of the real emission and subtraction terms

The cross section of the subtracted real emission contribution is obtained by integrating the difference between the real emission matrix elements and the corresponding dipole terms over the phase space. That means for the example of the first subprocess, the subtracted real emission cross section is given by:

$$
\sigma^{Real} \left(q(p_a)\, \bar{Q}(p_b) \rightarrow \text{VVV} + g(p_f) \right)
$$
$$
= \int_0^1 dx_a \int_0^1 dx_b \int d\phi_7(p_a + p_b \rightarrow k_1, ...k_6, p_f)\, \frac{1}{\hat{s}}
$$
$$
\cdot f_{q/P}\left(x_a; \mu_F^2\right) f_{\bar{Q}/P}\left(x_b; \mu_F^2\right)
$$
$$
\cdot \left[\left| M\left(q(p_a)\, \bar{Q}(p_b) \rightarrow \text{VVV} + g(p_f)\right) \right|^2 \right.
$$
$$
\left. - \mathcal{D}^{q(p_a)g(p_f),\bar{Q}(p_b)} - \mathcal{D}^{\bar{Q}(p_b)g(p_f),q(p_b)} \right].
$$
(A.14)

As has already been pointed out, two dipole terms are needed here. For the $\bar{Q}q$-initiated subprocesses the formula for the subtracted real emission cross section is very similar.

In the case of the gluon induced subprocesses, the contribution is alike, but only one counter term has to be subtracted from the real emission matrix element squared. The subtracted real emission cross section for the first gluon induced subprocess is then given by:

$$
\begin{aligned}
\sigma^{Real} &\left(g(p_a)\, q(p_b) \rightarrow \text{VVV} + Q(p_f) \right) \\
&= \int_0^1 dx_a \int_0^1 dx_b \int d\phi_7(p_a + p_b \rightarrow k_1, ...k_6, p_f)\, \frac{1}{\hat{s}} \\
&\quad \cdot f_{g/P}\left(x_a; \mu_F^2\right)\, f_{\bar{Q}/P}\left(x_b; \mu_F^2\right) \\
&\quad \cdot \left[\, \left| M\left(g(p_a)\, q(p_b) \rightarrow \text{VVV} + Q(p_f) \right) \right|^2 - \mathcal{D}^{g(p_a)Q(p_f),q(p_b)} \,\right].
\end{aligned}
\tag{A.15}
$$

Again, analogous expressions are obtained for the other gluon induced subprocesses.

Up to now, only the calculation of subtracted real emission cross sections for proton-proton interactions has been discussed. However, the procedure described in this Section is completely general in the way, that by simple taking antiproton parton distribution functions instead of proton pdfs, the protons can be interchanged by their antiparticles.

A.2 Virtual contribution and the integrated dipole

The infrared divergencies of the virtual contribution are analytically canceled against the integrated dipole. In the notation of Catani and Seymour this cancellation reads,

$$
\begin{aligned}
\sigma_{ab}^{NLO,\{6-particles\}}&(p_a, p_b) \\
&= \int d\Phi_6 \left[\, d\sigma_{ab}^V(p_a, p_b) + d\sigma_{ab}^B(p_a, p_b) \otimes \mathbf{I} \,\right]_{\epsilon=0} \\
&= \int d\Phi_6 \left(\, 2\,\text{Re}\left[\, M_{1-loop}\, M_{Born}^* \,\right] + \langle\, p_a, p_b\, |\mathbf{I}(\epsilon)\, |\, p_a, p_b\, \rangle \right),
\end{aligned}
\tag{A.16}
$$

with the insertion operator $\mathbf{I}$ defined as:

$$\mathbf{I}(p_a, p_b; \epsilon) = -\frac{\alpha_s}{2\pi} \frac{1}{\Gamma(1-\epsilon)} \sum_I \frac{1}{T_I^2} V_I(\epsilon) \sum_{J \neq I} T_I \cdot T_J \left(\frac{4\pi\mu^2}{2p_I \cdot p_J} \right)^\epsilon$$

$$= -\frac{\alpha_s}{2\pi} \frac{1}{\Gamma(1-\epsilon)} \left[\frac{1}{T_a^2} V_a(\epsilon) (T_b \cdot T_a) \left(\frac{4\pi\mu^2}{2p_b \cdot p_a} \right)^\epsilon \right. \qquad (A.17)$$

$$\left. + \frac{1}{T_b^2} V_b(\epsilon) (T_b \cdot T_a) \left(\frac{4\pi\mu^2}{2p_b \cdot p_a} \right)^\epsilon \right].$$

Here, indices a and b refer to the (anti) quarks in the initial state. No gluons in the initial state appear in this expressions for the virtual counter term.

Thus, inserting

$$V_q(\epsilon) = V_{\bar{q}}(\epsilon) = T_q^2 \left(\frac{1}{\epsilon^2} - \frac{\pi^2}{3} \right) + \gamma_q \frac{1}{\epsilon} + \gamma_q + K_q + \mathcal{O}(\epsilon) \qquad (A.18)$$

with γ_q and K_q defined as

$$\gamma_q = \gamma_{\bar{q}} = \frac{3}{2} C_F, \qquad\qquad K_q = K_{\bar{q}} = \left(\frac{7}{2} - \frac{\pi^2}{6} \right) C_F, \qquad (A.19)$$

the final result for the insertion operator in dimensional regularization up to $\mathcal{O}(\epsilon)$ is then given by:

$$\langle p_a, p_b \mid \mathbf{I}(\epsilon) \mid p_a, p_b \rangle$$

$$= \frac{\alpha_s}{2\pi} \frac{1}{\Gamma(1-\epsilon)} C_F \left(\frac{4\pi\mu^2}{Q^2} \right)^\epsilon \left[\frac{2}{\epsilon^2} + \frac{3}{\epsilon} - \pi^2 + 10 \right] \cdot |M_B|^2$$

$$= \frac{\alpha_s}{2\pi} C_F \left(\frac{4\pi\mu^2}{Q^2} \right)^\epsilon \Gamma(1+\epsilon) \left[\frac{2}{\epsilon^2} + \frac{3}{\epsilon} - \pi^2 + 10 - \frac{\pi^2}{3} \right] \cdot |M_B|^2 \qquad (A.20)$$

$$= \frac{\alpha_s}{2\pi} C_F \left(\frac{4\pi\mu^2}{Q^2} \right)^\epsilon \Gamma(1+\epsilon) \left[\frac{2}{\epsilon^2} + \frac{3}{\epsilon} + 8 - \frac{4\pi^2}{3} + \mathtt{cvirt} \right] \cdot |M_B|^2.$$

In these expressions, the partonic center of mass energy squared $Q^2 = (p_a + p_b^2) = 2p_a \cdot p_b$ is used and $|M_B|^2$ denotes the full Born matrix element squared, i.e. the sum of $q\bar{Q}$-initiated matrix elements and $\bar{Q}q$-initiated ones squared. The variable `cvirt` depends on the regularization procedure. In dimensional regularization it is given by `cvirt = 2` and in dimensional reduction this factor is given by `cvirt = 1`. The ϵ-poles in Eq. (A.20) are then canceled against the virtual contributions given in Eq. (3.27) as described in Section 3.2.4.

A.3 Additional finite collinear terms

Collinear divergencies, arising if the angle between emitted parton and initial-state parton becomes too small, are absorbed into the parton distribution functions leaving a finite remainder. In the algorithm proposed by Catani and Seymour, they are collected in the formula:

$$
\begin{aligned}
\int_0^1 & dx \left[\hat{\sigma}_{ab}^{NLO,\{0\}}(x, xp_a, p_b; \mu_F^2) + \hat{\sigma}_{ab}^{NLO,\{0\}}(x, p_a, xp_b; \mu_F^2) \right] \\
&= \sum_{a'} \int_0^1 dx \left[d\sigma_{a'b}^B(xp_a, p_b) \otimes (\mathbf{K} + \mathbf{P})^{aa'}(x) \right] \\
&+ \sum_{b'} \int_0^1 dx \left[d\sigma_{ab'}^B(p_a, xp_b) \otimes (\mathbf{K} + \mathbf{P})^{bb'}(x) \right] \\
&= \sum_{a'} \int_0^1 dx \; \langle \, xp_a, p_b \, | (\mathbf{K}^{aa'}(x) + \mathbf{P}^{aa'}(xp_a, x; \mu_F^2)) \, | \, xp_a, p_b \, \rangle \\
&+ \sum_{b'} \int_0^1 dx \; \langle \, p_a, xp_b \, | (\mathbf{K}^{bb'}(x) + \mathbf{P}^{bb'}(xp_b, x; \mu_F^2)) \, | \, p_a, xp_b \, \rangle.
\end{aligned}
\tag{A.21}
$$

For all the different types of subprocesses given in Section A.1, the corresponding finite collinear terms are developed in this section. At the end of the section compact formulas of these additional finite collinear contributions are given.

A.3.1 Quark induced subprocesses

Both types of subprocesses with emission of a gluon from the quark lines necessitate two different dipoles in order to absorb their divergencies. Correspondingly two finite collinear terms need to be calculated. For the first type of diagrams with a gluon

90

emitted from the upper line, $q(p_a) \bar{Q}(p_b) \to \mathrm{VVV} + g(p_f)$, the general expression for the finite remainder in the notation of Catani and Seymour is:

$$
\begin{aligned}
&\langle\, xp_a, p_b \mid \left(\mathbf{K}^{qq}(x) + \mathbf{P}^{qq}(xp_a, x; \mu_F^2) \right) \mid xp_a, p_b \,\rangle \\
&= \frac{\alpha_s}{2\pi}\, C_F\, \langle\, xp_a, p_b \mid xp_a, p_b \,\rangle \cdot \left\{\, 1 - x - (1+x)\, \ln\left(\frac{(1-x)^2}{x}\right) \right. \\
&+ \delta(1-x)\, \left(\frac{2\pi^2}{3} - 5\right) + \left(\frac{2}{1-x}\, \ln\left(\frac{1-x}{x}\right)\right)_+ \\
&\left. + \left(\frac{2}{1-x}\, \ln\left(1-x\right)\right)_+ - \left(\frac{1+x^2}{1-x}\right)_+\, \ln\left(\frac{\mu_F^2}{2xp_a \cdot p_b}\right) \,\right\}.
\end{aligned}
\tag{A.22}
$$

Taking the convolution with the parton distribution functions into account and performing a variable substitution $(z = xx_a)$ one obtains:

$$
\begin{aligned}
&\int_0^1 dx_a \int_0^1 dx_b\, f_{q/p}\left(x_a; \mu_F^2\right)\, f_{\bar{Q}/p}\left(x_b; \mu_F^2\right) \\
&\quad \int_0^1 dx\, \langle\, xp_a, p_b \mid xp_a, p_b \,\rangle\, \frac{\alpha_s}{2\pi}\, C_F\, \left\{...\right\} \\
&= \int_0^1 dx_b \int_0^1 dz\, f_{\bar{Q}/p}\left(x_b; \mu_F^2\right)\, \langle\, zP_{1,in}, p_b \mid zP_{1,in}, p_b \,\rangle \\
&\quad \int_0^1 \frac{dx}{x}\, f_{q/p}\left(\frac{z}{x}; \mu_F^2\right)\, \frac{\alpha_s}{2\pi}\, C_F\, \left\{\, 1 - x - (1+x)\, \ln\left(\frac{(1-x)^2}{x}\right) \right. \\
&+ \delta(1-x)\, \left(\frac{2\pi^2}{3} - 5\right) + \left(\frac{2}{1-x}\, \ln\left(\frac{1-x}{x}\right)\right)_+ \\
&\left. + \left(\frac{2}{1-x}\, \ln\left(1-x\right)\right)_+ - \left(\frac{1+x^2}{1-x}\right)_+\, \ln\left(\frac{\mu_F^2}{Q^2}\right) \,\right\} \theta(x-z)
\end{aligned}
\tag{A.23}
$$

The variable Q^2 appearing in this expression is the partonic center of mass energy in the new variables $Q^2 = 2\, z\, P_{1,in} \cdot p_b$. The x-integration can then partly be carried out and the $+$ - distributions defined as

$$\int_0^1 dx \; g(x) \; f(x)_+ \; \theta(x - z)$$
$$= \int_z^1 dx \; (\; g(x) - g(1) \;) \; f(x) - \int_0^z dx \; g(1) \; f(x) \tag{A.24}$$

can be eliminated using Eqs. (A.41), (A.43), and (A.44) in Section A.4,

$$\int_0^1 \frac{dx}{x} \; f_{q/p}\left(\frac{z}{x}; \mu_F^2\right) \left\{ 1 - x - (1 + x) \; \ln\left(\frac{(1 - x)^2}{x}\right) \right.$$
$$+ \delta(1 - x) \left(\frac{2\pi^2}{3} - 5\right) + \left(\frac{2}{1 - x} \; \ln\left(\frac{1 - x}{x}\right)\right)_+$$
$$+ \left(\frac{2}{1 - x} \; \ln(1 - x)\right)_+ - \left(\frac{1 + x^2}{1 - x}\right)_+ \; \left. \ln\left(\frac{\mu_F^2}{Q^2}\right) \right\} \theta(x - z)$$
$$= \int_z^1 \frac{dx}{x} \; \left(f_{q/p}\left(\frac{z}{x}; \mu_F^2\right) - x \; f_{q/p}\left(z; \mu_F^2\right)\right)$$
$$\left[\frac{2}{1 - x} \; \ln(1 - x)^2 + \frac{2}{1 - x} \; \ln\left(\frac{Q^2}{\mu_F^2}\right)\right] \tag{A.25}$$
$$+ \int_z^1 \frac{dx}{x} \; f_{q/p}\left(\frac{z}{x}; \mu_F^2\right) \left[\frac{2}{1 - x} \; \ln(1 - x)^2 + \frac{2}{1 - x} \; \ln\left(\frac{Q^2}{\mu_F^2}\right)\right]$$
$$+ f_{q/p}\left(z; \mu_F^2\right) \left[\frac{3}{2} \ln\left(\frac{Q^2}{\mu_F^2}\right) + 2 \ln(1 - z) \ln\left(\frac{Q^2}{\mu_F^2}\right)\right.$$
$$\left. + 2 \ln^2(1 - z) + \frac{\pi^2}{3} - 5\right].$$

For the emission of a gluon from the lower line, the expression which has to be computed is

$$\langle\, p_a, xp_b \mid \left(\mathbf{K}^{\bar{Q}\bar{Q}}(x) + \mathbf{P}^{\bar{Q}\bar{Q}}(xp_b, x; \mu_F^2) \right) \mid p_a, xp_b \,\rangle$$

$$= \frac{\alpha_s}{2\pi}\, C_F\, \langle\, p_a, xp_b \mid p_a, xp_b \,\rangle \cdot \left\{\, 1 - x - (1+x)\, \ln\left(\frac{(1-x)^2}{x}\right)\right.$$

$$+ \delta(1-x)\left(\frac{2\pi^2}{3} - 5\right) + \left(\frac{2}{1-x}\, \ln\left(\frac{1-x}{x}\right)\right)_+ \tag{A.26}$$

$$\left. + \left(\frac{2}{1-x}\, \ln\,(1-x)\right)_+ - \left(\frac{1+x^2}{1-x}\right)_+ \ln\left(\frac{\mu_F^2}{2\,p_a\cdot x\,p_b}\right)\,\right\}.$$

Thus the relevant Born matrix element is different. Otherwise the expression is the same as before. Taking the convolution with the parton distribution functions into account and performing a variable substitution $(\bar{z} = xx_b)$ one obtains:

$$\int_0^1 dx_a \int_0^1 dx_b\, f_{q/p}\,(x_a; \mu_F^2)\, f_{\bar{Q}/p}\,(x_b; \mu_F^2)$$

$$\int_0^1 dx\, \langle\, p_a, xp_b \mid p_a, xp_b \,\rangle\, \frac{\alpha_s}{2\pi}\, C_F\, \{...\}$$

$$= \int_0^1 dx_a \int_0^1 d\bar{z}\, f_{q/p}\,(x_a; \mu_F^2)\, \langle\, p_a, \bar{z}P_{2,in} \mid p_a, \bar{z}P_{2,in} \,\rangle \tag{A.27}$$

$$\int_0^1 \frac{dx}{x}\, f_{\bar{Q}/p}\left(\frac{\bar{z}}{x}; \mu_F^2\right)\, \frac{\alpha_s}{2\pi}\, C_F\, \{...\}\, \theta(x - \bar{z}).$$

The x-integration is exactly the same already performed in Eq. (A.25) with z replaced by $\bar{z}$ and $2\tilde{p}_a\cdot p_b$ replaced by $2p_a\cdot\tilde{p}_b$.

In a completely analogous way the finite collinear expressions for the second subprocess $\bar{Q}(p_a)\,q(p_b) \to \text{VVV} + g(p_f)$ are determined.

A.3.2 Subprocesses with an initial-state gluon

For the subprocess depicted in Fig. A.2c a gluon splits into a quark and an antiquark. This splitting causes collinear divergencies, which are absorbed into the parton distribution functions and leads to finite collinear remnants. In the notation of Catani and Seymour we get:

$$
\langle\, xp_a, p_b\, |(\mathbf{K}^{gq}(x) + \mathbf{P}^{gq}(xp_a, x; \mu_F^2))\,|\, xp_a, p_b\,\rangle
$$
$$
= \frac{\alpha_s}{2\pi}\, T_R\,\langle\, xp_a, p_b\, |\, xp_a, p_b\,\rangle
$$
$$
\left\{ 2x(1-x) + (x^2 + (1-x)^2)\,\left(\ln\left(\frac{(1-x)^2}{x}\right) - \ln\left(\frac{\mu_F^2}{2xp_a \cdot p_b}\right)\right)\right\}. \tag{A.28}
$$

In the same way as before, a variable transformation $(z = xx_a)$ is performed, which can directly be evaluated since no complicated $+$ - distributions appear,

$$
\int_0^1 dx_a\,\int_0^1 dx_b\, f_{g/p}\,(x_a; \mu_F^2)\, f_{\bar{Q}/p}\,(x_b; \mu_F^2)
$$
$$
\int_0^1 dx\,\langle\, xp_a, p_b\, |\, xp_a, p_b\,\rangle\,\frac{\alpha_s}{2\pi}\, T_R\,\{...\}
$$
$$
= \int_0^1 dx_b\, f_{\bar{Q}/p}\,(x_b; \mu_F^2)\int_0^1 dz\,\langle\, zP_{1,in}, p_b\, |\, zP_{1,in}, p_b\,\rangle \tag{A.29}
$$
$$
\int_z^1 \frac{dx}{x}\, f_{g/p}\,\left(\frac{z}{x}; \mu_F^2\right)\,\frac{\alpha_s}{2\pi}\, T_R\,\Big\{2x\,(1-x)
$$
$$
+ (x^2 + (1-x)^2)\,\ln\left(\frac{(1-x)^2\,Q^2}{x\mu_F^2}\right)\Big\}.
$$

For all the other subprocesses with a gluon in the initial state the expressions are very much alike, hence they won't be calculated here in detail.

A.3.3 Compact expressions and implementation

Collecting all the expressions for the finite collinear remnants, one obtains:

$$
\sigma_{coll}^{NLO} = \int_0^1 dx_a \int_0^1 dx_b \int d\Phi_6 \left(k_1, ..., k_6; p_a + p_b \right) \frac{1}{\hat{s}}
$$
$$
\cdot \left[f_{q/p}^c \left(x_a; \mu_F^2 \right) f_{\bar{Q}/p} \left(x_b; \mu_F^2 \right) + f_{q/p} \left(x_a; \mu_F^2 \right) f_{\bar{Q}/p}^c \left(x_b; \mu_F^2 \right) \right]
$$
$$
\cdot \left| M_{Born}^{q\bar{Q}}(k_1, ..., k_6; p_a, p_b) \right|^2 .
$$
$$
+ \int_0^1 dx_a \int_0^1 dx_b \int d\Phi_6 \left(k_1, ..., k_6; p_a + p_b \right) \frac{1}{\hat{s}}
$$
$$
\cdot \left[f_{\bar{Q}/p}^c \left(x_a; \mu_F^2 \right) f_{q/p} \left(x_b; \mu_F^2 \right) + f_{\bar{Q}/p} \left(x_a; \mu_F^2 \right) f_{q/p}^c \left(x_b; \mu_F^2 \right) \right]
$$
$$
\cdot \left| M_{Born}^{\bar{Q}q}(k_1, ..., k_6; p_a, p_b) \right|^2 .
$$

(A.30)

where the terms calculated in Eqs. (A.25) and (A.29) have been absorbed into the modified pdfs,

$$
f_{Q_i/p}^c \left(x_i; \mu_F^2 \right) = \frac{\alpha_s}{2\,\pi} \int_{x_i}^1 \frac{dx}{x} \left\{ f_{g/p} \left(\frac{x_i}{x}; \mu_F^2 \right) \; A(x) \right.
$$
$$
+ \left[f_{Q_i/p} \left(\frac{x_i}{x}; \mu_F^2 \right) - x\, f_{Q_i/p} \left(x_i, \mu_F^2 \right) \right] \; B(x)
$$
$$
\left. + f_{Q_i/p} \left(\frac{x_i}{x}; \mu_F^2 \right) \; C(x) \right\} + \frac{\alpha_s}{2\,\pi}\, f_{Q_i/p} \left(x_i; \mu_F^2 \right) \; D(x_i),
$$

(A.31)

with integration kernels,

$$
A(x) = T_R \left[2\,x\,(1-x) + \left(x^2 + (1-x)^2 \right) \cdot \ln \left(\frac{(1-x)^2\,Q^2}{x\,\mu_F^2} \right) \right]
$$
$$
B(x) = C_F \left[\frac{2}{1-x} \; \ln \left(\frac{Q^2\,(1-x)^2}{\mu_F^2} \right) \right]
$$
$$
C(x) = C_F \left[1 - x - \frac{2}{1-x} \; \ln\,(x) - (1+x) \; \ln \left(\frac{Q^2\,(1-x)^2}{x\,\mu_F^2} \right) \right]
$$
$$
D(x_i) = C_F \left[\frac{3}{2} \; \ln \left(\frac{Q^2}{\mu_F^2} \right) + 2 \; \ln\,(1-x_i) \; \ln \left(\frac{Q^2}{\mu_F^2} \right) \right.
$$
$$
\left. + 2 \; \ln^2\,(1-x_i) \right] + \frac{\pi^2}{3} - 5 \Big] .
$$

(A.32)

Though, in principal these expressions can be integrated over the m-particle phase space, in the actual implementation of a NLO Monte Carlo program, it is optimal, if these terms are calculated together with the real emission and subtraction terms. In order to do that, the relation between the 7-particle phase space and the 6-particle tilde kinematics given in Eqs. (3.23),

$$\frac{1}{2\,p_a \cdot p_b}\,d\phi_7\,(p_g, k_1, ..., k_6; p_a + p_b) =$$
$$\int_0^1 dx \int_0^{1-x} dv\, \frac{1}{2\,\tilde{p}_a \cdot p_b}\,\frac{Q^2}{8\,\pi^2}\,d\phi_6\,(\tilde{k}_1, ..., \tilde{k}_6; \tilde{p}_a + p_b),$$

(A.33)

is an essential ingredient. The parameter v needed in this expression is defined as

$$v = \frac{p_a \cdot p_g}{p_a \cdot p_b} \qquad \text{or} \qquad (p_a \leftrightarrow p_b).$$

(A.34)

The finite collinear terms can then be reformulated as part of the 7-particle phase space. In the case of the quark induced subprocesses, the additional finite collinear terms are then given by:

$$\sigma_{coll}^{NLO}\,(q(p_a)\,\bar{Q}(p_b) \to 6\ell + g(p_g))$$
$$= \int_0^1 dx_a \int_0^1 dx_b\, \frac{1}{2\,p_a \cdot p_b}\,d\Phi_7(k_1, ..., k_6, p_g; p_a + p_b)$$
$$\cdot \left\{ \frac{4\,\pi\,\alpha_s}{Q^2}\,f_{\bar{Q}/p}\,(x_b; \mu_F^2)\,\left|\,M_{Born}^{q\bar{Q}}(\tilde{k}_1, ...\tilde{k}_6; \tilde{p}_a, p_b)\,\right|^2 \cdot \frac{1}{1-x} \right.$$
$$\cdot \left[f_{q/p}\,(x_a; \mu_F^2)\,(B(x) + C(x)) + x\,f_{q/p}\,(xx_a; \mu_F^2)\,\left(\frac{D(xx_a)}{1-xx_a} - B(x)\right) \right]$$
$$+ \frac{4\,\pi\,\alpha_s}{Q^2}\,f_{q/p}\,(x_a; \mu_F^2)\,\left|\,M_{Born}^{q\bar{Q}}(\tilde{k}_1, ...\tilde{k}_6; p_a, \tilde{p}_b)\,\right|^2 \cdot \frac{1}{1-x}$$
$$\left. \cdot \left[f_{\bar{Q}/p}\,(x_b; \mu_F^2)\,(B(x) + C(x)) + x\,f_{\bar{Q}/p}\,(xx_b; \mu_F^2)\,\left(\frac{D(xx_b)}{1-xx_b} - B(x)\right) \right] \right\}$$

(A.35)

for the collinear terms proportional to the $q\bar{Q}$-type Born matrix elements, and

$$
\sigma_{coll}^{NLO} \left(\bar{Q}(p_a)\, q(p_b) \to 6\ell + g(p_g) \right)
$$

$$
= \int_0^1 dx_a \int_0^1 dx_b \, \frac{1}{2\, p_a \cdot p_b} \, d\Phi_7(k_1, ..., k_6, p_g; p_a + p_b)
$$

$$
\cdot \left\{ \frac{4\,\pi\,\alpha_s}{Q^2} \, f_{q/p}\left(x_b; \mu_F^2\right) \, \left| \, M_{Born}^{\bar{Q}q}(\tilde{k}_1, ...\tilde{k}_6; \tilde{p}_a, p_b) \, \right|^2 \cdot \frac{1}{1-x} \right.
$$

$$
\cdot \left[f_{\bar{Q}/p}\left(x_a; \mu_F^2\right)\,\left(B(x) + C(x)\right) + x\, f_{\bar{Q}/p}\left(x x_a; \mu_F^2\right) \left(\frac{D(x x_a)}{1 - x x_a} - B(x) \right) \right]
$$

$$
+ \frac{4\,\pi\,\alpha_s}{Q^2} \, f_{\bar{Q}/p}\left(x_a; \mu_F^2\right) \, \left| \, M_{Born}^{\bar{Q}q}(\tilde{k}_1, ...\tilde{k}_6; p_a, \tilde{p}_b) \, \right|^2 \cdot \frac{1}{1-x}
$$

$$
\left. \cdot \left[f_{q/p}\left(x_b; \mu_F^2\right)\,\left(B(x) + C(x)\right) + x\, f_{q/p}\left(x x_b; \mu_F^2\right) \left(\frac{D(x x_b)}{1 - x x_b} - B(x) \right) \right] \right\}
$$

$$(A.36)$$

for terms proportional to $\bar{Q}q$-induced Born matrix elements. For the gluon induced subprocesses, the corresponding expressions are:

$$
\sigma_{coll}^{NLO} \left(g(p_a)\, q(p_b) \to 6\ell + Q(p_g) \right)
$$

$$
= \int_0^1 dx_a \int_0^1 dx_b \, \frac{1}{2\, p_a \cdot p_b} \, d\Phi_7(k_1, ..., k_6, p_g; p_a + p_b)
$$

$$
\frac{4\,\pi\,\alpha_s}{Q^2} \, f_{q/p}\left(x_b; \mu_F^2\right) \, \left| \, M_{Born}^{\bar{Q}q}(\tilde{k}_1, ...\tilde{k}_6; \tilde{p}_a, p_b) \, \right|^2
$$

$$
\cdot \left[f_{g/p}\left(x_a; \mu_F^2\right)\, A(x) \right] \cdot \frac{1}{1-x},
$$

$$(A.37)$$

$$
\sigma_{coll}^{NLO} \left(g(p_a)\, \bar{Q}(p_b) \to 6\ell + \bar{q}(p_g) \right)
$$

$$
= \int_0^1 dx_a \int_0^1 dx_b \, \frac{1}{2\, p_a \cdot p_b} \, d\Phi_7(k_1, ..., k_6, p_g; p_a + p_b)
$$

$$
\frac{4\,\pi\,\alpha_s}{Q^2} \, f_{\bar{Q}/p}\left(x_b; \mu_F^2\right) \, \left| \, M_{Born}^{q\bar{Q}}(\tilde{k}_1, ...\tilde{k}_6; \tilde{p}_a, p_b) \, \right|^2
$$

$$
\cdot \left[f_{g/p}\left(x_a; \mu_F^2\right)\, A(x) \right] \cdot \frac{1}{1-x},
$$

$$(A.38)$$

$$\sigma_{coll}^{NLO}\left(q(p_a)\,g(p_b) \to 6\ell + Q(p_g)\right)$$

$$= \int_0^1 dx_a \int_0^1 dx_b \, \frac{1}{2\,p_a \cdot p_b} \, d\Phi_7(k_1, ..., k_6, p_g; p_a + p_b)$$

$$\frac{4\,\pi\,\alpha_s}{Q^2} \, f_{q/p}\left(x_a; \mu_F^2\right) \, \left|\, M_{Born}^{q\bar{Q}}(\tilde{k}_1, ...\tilde{k}_6; p_a, \tilde{p}_b)\,\right|^2$$

$$\cdot \left[f_{g/p}\left(x_b; \mu_F^2\right) \, A(x)\right] \cdot \frac{1}{1-x}, \tag{A.39}$$

$$\sigma_{coll}^{NLO}\left(\bar{Q}(p_a)\,g(p_b) \to 6\ell + \bar{q}(p_g)\right)$$

$$= \int_0^1 dx_a \int_0^1 dx_b \, \frac{1}{2\,p_a \cdot p_b} \, d\Phi_7(k_1, ..., k_6, p_g; p_a + p_b)$$

$$\frac{4\,\pi\,\alpha_s}{Q^2} \, f_{\bar{Q}/p}\left(x_a; \mu_F^2\right) \, \left|\, M_{Born}^{\bar{Q}q}(\tilde{k}_1, ...\tilde{k}_6; p_a, \tilde{p}_b)\,\right|^2$$

$$\cdot \left[f_{g/p}\left(x_b; \mu_F^2\right) \, A(x)\right] \cdot \frac{1}{1-x}. \tag{A.40}$$

Inserting Eq. (3.23) into these expression, the original finite collinear term given in Eq. (A.30) can then be obtained. In VBFNLO, for all the different subprocesses, the formulae given in Eqs. (A.35)- (A.40) are implemented and are integrated together with the subtracted real emission terms.

A.4   List of relevant integrals

In the calculation of the finite collinear remnants according to the formalism developed by Catani and Seymour, various non-trivial integrals arise. Those, which are needed for the calculation presented here are listed in the following.

The first integral needed in Eq. (A.25) is:

$$\int_0^1 \frac{dx}{x} \, f\left(\frac{z}{x}\right) \left(\frac{1}{1-x} \ln\left(\frac{1-x}{x}\right)\right)_+ \theta(x-z)$$

$$= \int_z^1 \frac{dx}{x} \left(f\left(\frac{z}{x}\right) - x \, f(z)\right) \left(\frac{1}{1-x} \ln\left(\frac{1-x}{x}\right)\right)$$

$$- \int_0^z dx \, f(z) \left(\frac{1}{1-x} \ln\left(\frac{1-x}{x}\right)\right)$$

$$= \int_z^1 \frac{dx}{x} \left(f\left(\frac{z}{x}\right) - x \, f(z)\right) \frac{\ln(1-x)}{1-x} - \int_z^1 \frac{dx}{x} \, f\left(\frac{z}{x}\right) \frac{\ln(x)}{1-x} \qquad \text{(A.41)}$$

$$+ f(z) \int_0^1 dx \, \frac{\ln(x)}{1-x} - f(z) \int_0^z dx \, \frac{\ln(1-x)}{1-x}$$

$$= \int_z^1 \frac{dx}{x} \left(f\left(\frac{z}{x}\right) - x \, f(z)\right) \frac{\ln(1-x)}{1-x} - \int_z^1 \frac{dx}{x} \, f\left(\frac{z}{x}\right) \frac{\ln(x)}{1-x}$$

$$+ f(z) \left(\frac{1}{2} \ln^2(1-z) - \frac{\pi^2}{6}\right).$$

In the last step,

$$\int_0^1 dx \, \frac{\ln(x)}{1-x} \, \ln(x) = -\int_1^0 du \, \frac{\ln(1-u)}{u} = -\operatorname{Li}_2(1) = -\frac{\pi^2}{6} \qquad \text{(A.42)}$$

has been used. The second integral, which is used in Eq. (A.25) is given by:

$$\int_0^1 \frac{dx}{x} \, f\left(\frac{z}{x}\right) \left(\frac{1}{1-x} \ln(1-x)\right)_+ \theta(x-z)$$

$$= \int_z^1 \frac{dx}{x} \left(f\left(\frac{z}{x}\right) - x \, f(z)\right) \frac{\ln(1-x)}{1-x} - \int_0^z dx \, f(z) \frac{\ln(1-x)}{1-x} \qquad \text{(A.43)}$$

$$= \int_z^1 \frac{dx}{x} \left(f\left(\frac{z}{x}\right) - x \, f(z)\right) \frac{\ln(1-x)}{1-x} + f(z) \frac{1}{2} \ln^2(1-z).$$

Finally, the last +-distribution appearing in Eq. (A.25) can be solved in the following way:

$$\int_0^1 \frac{dx}{x} \, f\left(\frac{z}{x}\right) \, \left(\frac{1+x^2}{1-x}\right)_+ \, \theta(x-z)$$

$$= \int_z^1 \frac{dx}{x} \, \left(f\left(\frac{z}{x}\right) - x \, f(z)\right) \, \left(\frac{1+x^2}{1-x}\right) - f(z) \int_0^z dx \, \left(\frac{1+x^2}{1-x}\right)$$

$$= \int_z^1 \frac{dx}{x} \, \left(f\left(\frac{z}{x}\right) - x \, f(z)\right) \, \frac{2}{1-x} + \int_z^1 \frac{dx}{x} \, f\left(\frac{z}{x}\right) \, (-1-x)$$

$$+ f(z) \int_z^1 \frac{dx}{x} \, (1+x) + f(z) \, \left(z + \frac{1}{2}z^2 + 2 \, \ln\left(1-z\right)\right)$$

$$= \int_z^1 \frac{dx}{x} \, \left(f\left(\frac{z}{x}\right) - x \, f(z)\right) \, \frac{2}{1-x} + \int_z^1 \frac{dx}{x} \, f\left(\frac{z}{x}\right) \, (-1-x)$$

$$+ f(z) \, \left(\frac{3}{2} + 2 \, \ln\left(1-z\right)\right).$$

(A.44)

Appendix B:

Symmetry factors

In the calculation of tri-boson processes in VBFNLO, three different lepton families are assumed for the decay products of the vector bosons, i.e. the processes

$$\text{W}^+\text{W}^-\text{Z} : \qquad pp \to \nu_e\, e^+\, \mu^-\, \bar{\nu}_\mu\, \tau^-\, \tau^+ + \text{X},$$

$$\text{ZZW}^+ : \qquad pp \to e^-\, e^+\, \mu^-\, \mu^+\, \nu_\tau\, \tau_3^+ + \text{X},$$

$$\text{ZZW}^- : \qquad pp \to e^-\, e^+\, \mu^-\, \mu^+\, \tau^-\, \bar{\nu}_\tau + \text{X},$$

are implemented. Phenomenologically more interesting are the cases of final states with electrons and/or muons. All possible subprocesses with only leptons of the first two families in the final state are given in Eq. (5.4) for the WWZ production and in Eq. (5.5) for the ZZW production modes. The majority of those subprocesses has identical leptons in the final state. Thus symmetry factors need to be taken into account. In the chapter at hand, they are derived for the WWZ and the ZZW production, separately.

B.1   WWZ production

In the WWZ production the two W-bosons always lead to distinguishable final state leptons. Therefore, identical leptons can only appear if either one W-boson and the Z-boson decay to the same lepton family or if all three vector bosons decay to electrons and the corresponding neutrinos or if all of them decay to muons and muon-neutrinos.

As an example for the first case, the subprocess $pp \to \nu_e e^+\, \mu^-\, \bar{\nu}_\mu\, e^-e^+ + \text{X}$ is examined in more detail. Since there are two positrons e^+ in the final state, the cross section for this subprocess has to be multiplied by a symmetry factor of $\frac{1}{2}$. However, this symmetry factor is compensated by twice the number of Feynman graphs compared

$$\sigma\left(pp \to \nu_e\, e^+ \, \mu^- \, \bar{\nu}_\mu \, \tau^- \, \tau^+\right) \sim \left| \begin{array}{c} \text{(diagram)} \end{array} \right|^2$$

$$\sigma\left(pp \to \nu_e\, e_1^+ \, \mu^- \, \bar{\nu}_\mu \, e^- \, e_2^+\right) \sim \left| \begin{array}{c} \text{(diagram 1)} \end{array} + \begin{array}{c} \text{(diagram 2)} \end{array} \right|^2$$

Figure B.1: *Sketch of the different Feynman-graphs contributing to the WWZ cross section with and without identical leptons in the final state.*

to the case of three different lepton families in the final state. In Fig. B.1 an example Feynman-graph for the case of electrons, muons and tau leptons in the final state as well as the case of the W^+ and the Z-boson both decaying to leptons of the first generation is given. In the latter case, the two electrons can swap their places in the Feynman-graph. Since this holds not only for the special diagram given in Fig. B.1 but for all graphs appearing in the calculation, two times the number of diagrams have to be taken into account in the calculation of the matrix elements.

Since for the calculation of the cross section, the matrix elements squared is the relevant quantity, in addition to the matrix elements squared of the first and the second graph, also interferences between them appear,

$$|M_1 + M_2|^2 = |M_1|^2 + |M_2^2| + (M_1 \cdot M_2^*) + (M_1^* \cdot M_2). \tag{B.1}$$

However, due to the resonance structure of the Feynman graphs, the two different momentum configurations can not lead simultaneously to big contributions. Therefore the interference terms are expected to be small. Neglecting these contributions, the cross section for the subprocess with one W-boson and the Z-boson decaying to the same type of leptons is therefore,

$$\sigma(pp \to \nu_e e^+ \, \mu^- \bar{\nu}_\mu \, e^- e^+ + \text{X}) = \frac{1}{2} \cdot 2 \cdot \sigma(pp \to \nu_e e^+ \, \mu^- \bar{\nu}_\mu \, \tau^- \tau^+ + \text{X}) \tag{B.2}$$

and thus the same as in the case of three different lepton families in the final state. In a very similar way one can also show that also the case with all vector bosons decaying to the same lepton family yields the same cross section. Results for the sum of all eight subprocesses given in Eq. (5.4) thus are given by multiplying cross sections and differential cross sections obtained for the process $pp \to \nu_e e^+ \; \mu^- \bar{\nu}_\mu \; \tau^- \tau^+ + X$ by a factor of eight.

B.2 ZZW production

In the ZZW production modes, the decay products of the two Z-bosons can be interchanged in the Feynman-graphs without altering the final state. Thus, two different orderings of the leptons are possible. Both of them are taken into account in the calculation implemented in VBFNLO and for both of them an example diagram symbolizing the sum of all possible matrix elements is drawn in Fig. B.2.

If only one of the W-bosons and one Z-boson would lead to identical particles in the final state, the argumentation applied in the WWZ case can be adapted and the symmetry factors are exactly absorbed into twice the number of Feynman graphs, yielding cross sections,

$$
\begin{aligned}
\sigma(pp \to e^- e^+ \mu^- \mu^+ \nu_e e^+) &= \sigma(pp \to e^- e^+ \mu^- \mu^+ \nu_\tau \tau^+) \\
\sigma(pp \to e^- e^+ \mu^- \mu^+ \nu_\mu \mu^+) &= \sigma(pp \to e^- e^+ \mu^- \mu^+ \nu_\tau \tau^+).
\end{aligned}
\tag{B.3}
$$

For the case of both Z-bosons decaying for instance to electrons, the relevant Feynman diagrams are shown in Fig. B.2. Here, only twice the number of graphs is possible without double counting. The symmetry factor for two electrons and two positrons in the final state, however is $\frac{1}{4}$. Thus, neglecting any interference effects due to identical particles in the final state, the cross section of both Z-bosons decaying to electrons or both of them decaying to muons is only half of the cross section with no identical leptons in the final state. A similar argumentation can also be applied to the case with all vector boson decaying to the same lepton generation.

In total, the sum of all subprocesses contributing to the $5\ell + \not{p}_T$ final state with $\ell = e, \mu$ yield a cross section, which is four times larger than the cross section calculated in the program. Therefore, all results for the ZZW production modes presented in Chapter 5 are multiplied with this combinatorial factor of four.

$$\sigma\left(pp \to e^- e^+ \mu^- \mu^+ \nu_\tau \tau^+\right) \sim \left| \text{} \right|^2$$

$$\sigma\left(pp \to e_1^- e_1^+ e_2^- e_2^+ \nu_\mu \mu^+\right) \sim \left| \text{} \right|^2$$

Figure B.2: *Sketch of the different Feynman-graphs contributing to the ZZW^+ cross section with and without identical leptons in the final state.*

Bibliography

[1] C. Buttar *et al.*, *Les Houches physics at TeV colliders 2005, standard model, QCD, EW, and Higgs working group: Summary report*, arXiv:hep-ph/0604120.

[2] B. Jager, C. Oleari and D. Zeppenfeld, *Next-to-leading order QCD corrections to $W^+ W^-$ production via vector-boson fusion*, JHEP **0607** (2006) 015 [arXiv:hep-ph/0603177].

[3] B. Jager, C. Oleari and D. Zeppenfeld, *Next-to-leading order QCD corrections to Z boson pair production via vector-boson fusion*, Phys. Rev. D **73** (2006) 113006 [arXiv:hep-ph/0604200].

[4] G. Bozzi, B. Jager, C. Oleari and D. Zeppenfeld, *Next-to-leading order QCD corrections to W+Z and W-Z production via vector-boson fusion*, Phys. Rev. D **75** (2007) 073004 [arXiv:hep-ph/0701105].

[5] A. Lazopoulos, K. Melnikov and F. Petriello, *QCD corrections to tri-boson production*, Phys. Rev. D **76** (2007) 014001 [arXiv:hep-ph/0703273].

[6] S. Dittmaier, S. Kallweit and P. Uwer, *NLO QCD corrections to WW+jet production at hadron colliders*, Phys. Rev. Lett. **100** (2008) 062003 [arXiv:0710.1577 [hep-ph]]. [7]

[7] J. M. Campbell, R. Keith Ellis and G. Zanderighi, *Next-to-leading order predictions for WW + 1 jet distributions at the LHC*, JHEP **0712** (2007) 056 [arXiv:0710.1832 [hep-ph]].

[8] T. Figy, V. Hankele and D. Zeppenfeld, *Next-to-leading order QCD corrections to Higgs plus three jet production in vector-boson fusion*, JHEP **0802** (2008) 076 [arXiv:0710.5621 [hep-ph]].

[9] V. Hankele and D. Zeppenfeld, *QCD corrections to hadronic WWZ production with leptonic decays*, Phys. Lett. B **661** (2008) 103 [arXiv:0712.3544 [hep-ph]].

[10] Z. Bern *et al.* [NLO Multileg Working Group], *The NLO multileg working group: summary report*, arXiv:0803.0494 [hep-ph].

[11] T. Binoth, G. Ossola, C. G. Papadopoulos and R. Pittau, *NLO QCD corrections to tri-boson production*, arXiv:0804.0350 [hep-ph].

[12] G. Sanguinetti and S. Karg, *NLO QCD corrections to the production of a weak boson pair associated by a hard jet*, arXiv:0806.1394 [hep-ph].

[13] A. Bredenstein, A. Denner, S. Dittmaier and S. Pozzorini, *NLO QCD corrections to top anti-top bottom anti-bottom production at the LHC: 1. quark-antiquark annihilation*, JHEP **0808** (2008) 108 [arXiv:0807.1248 [hep-ph]].

[14] F. Campanario, V. Hankele, C. Oleari, S. Prestel and D. Zeppenfeld, *QCD corrections to charged triple vector boson production with leptonic decay*, Phys. Rev. D **78** (2008) 094012 arXiv:0809.0790 [hep-ph].

[15] R. K. Ellis, W. T. Giele, Z. Kunszt, K. Melnikov and G. Zanderighi, *One-loop amplitudes for W+3 jet production in hadron collisions*, arXiv:0810.2762 [hep-ph].

[16] J. Alcaraz *et al.* [ALEPH Collaboration], *A combination of preliminary electroweak measurements and constraints on the standard model*, arXiv:hep-ex/0612034.

[17] M. Golden and S. R. Sharpe, *Three weak gauge boson production at the Ssc*, Nucl. Phys. B **261** (1985) 217.

[18] V. D. Barger and T. Han, Triple gauge boson production at e$^+$ e$^-$ and p p supercolliders, Phys. Lett. B **212** (1988) 117.

[19] T. Han and R. Sobey, *Triple electroweak gauge boson productions at Fermilab Tevatron energies*, Phys. Rev. D **52** (1995) 6302 [arXiv:hep-ph/9507409].

[20] P. J. Dervan, A. Signer, W. J. Stirling and A. Werthenbach, *Anomalous triple and quartic gauge boson couplings*, J. Phys. G **26** (2000) 607 [arXiv:hep-ph/0002175].

[21] O. J. P. Eboli, M. C. Gonzalez-Garcia, S. M. Lietti and S. F. Novaes, *Anomalous quartic gauge boson couplings at hadron colliders*, Phys. Rev. D **63** (2001) 075008 [arXiv:hep-ph/0009262].

[22] D. Green, *Triple vector boson production at the LHC*, arXiv:hep-ex/0310004.

[23] J. Ohnemus, *An order alpha-s calculation of hadronic W- W+ production*, Phys. Rev. D **44** (1991) 1403.

[24] J. Ohnemus, *An order alpha-s calculation of hadronic W+- Z production*, Phys. Rev. D **44** (1991) 3477.

[25] J. Ohnemus, *Hadronic Z Z, W- W+, and W+- Z production with QCD corrections and leptonic decays*, Phys. Rev. D **50** (1994) 1931 [arXiv:hep-ph/9403331].

[26] U. Baur, T. Han and J. Ohnemus, *W Z production at hadron colliders: Effects of nonstandard W W Z couplings and QCD corrections*, Phys. Rev. D **51** (1995) 3381 [arXiv:hep-ph/9410266].

[27] U. Baur, T. Han and J. Ohnemus, *QCD corrections and nonstandard three vector boson couplings in W+ W- production at hadron colliders*, Phys. Rev. D **53** (1996) 1098 [arXiv:hep-ph/9507336].

[28] L. J. Dixon, Z. Kunszt and A. Signer, *Vector boson pair production in hadronic collisions at O(alpha(s)): Lepton correlations and anomalous couplings*, Phys. Rev. D **60** (1999) 114037 [arXiv:hep-ph/9907305].

[29] L. J. Dixon, Z. Kunszt and A. Signer, *Helicity amplitudes for O(alpha(s)) production of W+ W-, W+- Z, Z Z, W+-gamma, or Z gamma pairs at hadron colliders*, Nucl. Phys. B **531** (1998) 3 [arXiv:hep-ph/9803250].

[30] J. M. Campbell and R. K. Ellis, *An update on vector boson pair production at hadron colliders*, Phys. Rev. D **60** (1999) 113006 [arXiv:hep-ph/9905386].

[31] K. Arnold *et al.*, *VBFNLO: A parton level Monte Carlo for processes with electroweak bosons*, arXiv:0811.4559 [hep-ph].

[32] F. Halzen and A. D. Martin, *Quarks and leptons: an introductory course in modern particle physics*, *New York, Usa: Wiley (1984) 396p*

[33] M. E. Peskin and D. V. Schroeder, *An introduction to quantum field theory*, *Reading, USA: Addison-Wesley (1995) 842 p*

[34] R. K. Ellis, W. J. Stirling and B. R. Webber, *QCD and collider physics*, Camb. Monogr. Part. Phys. Nucl. Phys. Cosmol. **8** (1996) 1.

[35] G. Dissertori, I. G. Knowles and M. Schmelling, *High energy experiments and theory*, *Oxford, UK: Clarendon (2003) 538 p*

[36] M. Bohm, A. Denner and H. Joos, *Gauge theories of the strong and electroweak interaction*, *Stuttgart, Germany: Teubner (2001) 784 p*

[37] C. Amsler *et al.* [Particle Data Group], *Review of particle physics*, Phys. Lett. B **667** (2008) 1.

[38] C. Schwanenberger [for the CDF and D0 Collaborations], *Top quark mass in lepton + jets decays at the Tevatron*, arXiv:0812.1529 [hep-ex].

[39] A. D. Martin, R. G. Roberts and W. J. Stirling, *Precision analysis of Lambda (MS) and the gluon distribution and its implication for jet and top quark cross-sections*, Phys. Rev. D **43** (1991) 3648.

[40] K. Abe *et al.* [VENUS Collaboration], *Determination of the QCD scale parameter Lambda (ms) with QCD cascade on the basis of the next-to-leading logarithmic approximation*, Phys. Lett. B **240** (1990) 232.

[41] P. Z. Quintas *et al.*, *A measurement af Lambda (MS) from muon-neutrino - Fe nonsinglet structure functions at the Fermilab Tevatron*, Phys. Rev. Lett. **71** (1993) 1307.

[42] D. J. Gross and F. Wilczek, *Ultraviolet behaviour of non-Abelian gauge theories*, Phys. Rev. Lett. **30** (1973) 1343.

[43] H. D. Politzer, *reliable perturbative results for strong interactions?*, Phys. Rev. Lett. **30** (1973) 1346.

[44] V. N. Gribov and L. N. Lipatov, *Deep inelastic ep scattering in perturbation theory*, Sov. J. Nucl. Phys. **15** (1972) 438 [Yad. Fiz. **15** (1972) 781].

[45] G. Altarelli and G. Parisi, *Asymptotic freedom in parton language*, Nucl. Phys. B **126** (1977) 298.

[46] Y. L. Dokshitzer, *Calculation of the structure functions for deep inelastic scattering and e^+e^- annihilation by perturbation theory in Quantum Chromodynamics. (in Russian)*, Sov. Phys. JETP **46** (1977) 641 [Zh. Eksp. Teor. Fiz. **73** (1977) 1216].

[47] S. Catani and M. H. Seymour, *The dipole formalism for the calculation of QCD jet cross sections at next-to-leading order*, Phys. Lett. B **378** (1996) 287 [arXiv:hep-ph/9602277].

[48] S. Catani and M. H. Seymour, *A general algorithm for calculating jet cross sections in NLO QCD*, Nucl. Phys. B **485** (1997) 291 [Erratum-ibid. B **510** (1998) 503] [arXiv:hep-ph/9605323].

[49] K. Hagiwara and D. Zeppenfeld, *Helicity amplitudes for heavy lepton production in e^+e^- annihilation*, Nucl. Phys. B **274** (1986) 1.

[50] K. Hagiwara and D. Zeppenfeld, *Amplitudes for multiparton processes involving a current at e^+e^-, e^+p and hadron colliders*, Nucl. Phys. B **313** (1989) 560.

[51] T. Stelzer and W. F. Long, *Automatic generation of tree level helicity amplitudes*, Comput. Phys. Commun. **81** (1994) 357 [arXiv:hep-ph/9401258].

[52] F. Maltoni and T. Stelzer, *MadEvent: Automatic event generation with MadGraph*, JHEP **0302** (2003) 027 [arXiv:hep-ph/0208156].

[53] J. Alwall *et al.*, *MadGraph/MadEvent v4: The New Web Generation* JHEP **0709** (2007) 028 [arXiv:0706.2334 [hep-ph]].

[54] A. Cafarella, C. G. Papadopoulos and M. Worek, *Helac-Phegas: a generator for all parton level processes*, arXiv:0710.2427 [hep-ph].

[55] C. G. Papadopoulos and M. Worek, *Multi-parton cross sections at hadron colliders*, Eur. Phys. J. C **50** (2007) 843 [arXiv:hep-ph/0512150].

[56] A. Kanaki and C. G. Papadopoulos, *HELAC: A package to compute electroweak helicity amplitudes*, Comput. Phys. Commun. **132** (2000) 306 [arXiv:hep-ph/0002082].

[57] C. Oleari and D. Zeppenfeld, *Next-to-leading order QCD corrections to W and Z production via vector-boson fusion*, Phys. Rev. D **69** (2004) 093004 [arXiv:hep-ph/0310156].

[58] G. Passarino and M. J. G. Veltman, *One loop corrections for $e^+ e^-$ annihilation into $\mu^+ \mu^-$ in the Weinberg model*, Nucl. Phys. B **160** (1979) 151.

[59] A. Denner and S. Dittmaier, *Reduction of one-loop tensor 5-point integrals*, Nucl. Phys. B **658**, 175 (2003) [arXiv:hep-ph/0212259].

[60] A. Denner and S. Dittmaier, *Reduction schemes for one-loop tensor integrals*, Nucl. Phys. B **734**, 62 (2006) [arXiv:hep-ph/0509141].

[61] G. Bozzi, F. Campanario and D. Zeppenfeld, in preparation

[62] J. Pumplin, D. R. Stump, J. Huston, H. L. Lai, P. Nadolsky and W. K. Tung, *New generation of parton distributions with uncertainties from global QCD analysis*, JHEP **0207** (2002) 012 [arXiv:hep-ph/0201195].

[63] A. Djouadi, J. Kalinowski and M. Spira, *HDECAY: A program for Higgs boson decays in the standard model and its supersymmetric extension*, Comput. Phys. Commun. **108** (1998) 56 [arXiv:hep-ph/9704448].

[64] A. Djouadi, *The anatomy of electro-weak symmetry breaking. I: The Higgs boson in the standard model*, Phys. Rept. **457** (2008) 1 [arXiv:hep-ph/0503172].

[65] T. Han and S. Willenbrock, *QCD correction to the $p\,p \to W\,H$ and $Z\,H$ total cross-sections*, Phys. Lett. B **273** (1991) 167.

[66] J. Ohnemus and W. J. Stirling, *Order α_s corrections to the differential cross-section for the $W\,H$ intermediate mass Higgs signal*, Phys. Rev. D **47** (1993) 2722.

[67] H. Baer, B. Bailey and J. F. Owens, *$O\,(\alpha_s)$ Monte Carlo approach to W^+ Higgs associated production at hadron supercolliders*, Phys. Rev. D **47** (1993) 2730.

[68] M. Spira, *QCD effects in Higgs physics*, Fortsch. Phys. **46** (1998) 203 [arXiv:hep-ph/9705337].

[69] O. Brein, M. Ciccolini, S. Dittmaier, A. Djouadi, R. Harlander and M. Kramer, *Precision calculations for associated $W\,H$ and $Z\,H$ production at hadron colliders*, arXiv:hep-ph/0402003.

[70] R. Hamberg, W. L. van Neerven and T. Matsuura, *A complete calculation of the order α_s^2 correction to the Drell-Yan K factor*, Nucl. Phys. B **359** (1991) 343 [Erratum-ibid. B **644** (2002) 403].

[71] R. V. Harlander and W. B. Kilgore, *Next-to-next-to-leading order Higgs production at hadron colliders*, Phys. Rev. Lett. **88** (2002) 201801 [arXiv:hep-ph/0201206].

[72] C. Anastasiou, L. J. Dixon, K. Melnikov and F. Petriello, *High-precision QCD at hadron colliders: Electroweak gauge boson rapidity distributions at NNLO*, Phys. Rev. D **69** (2004) 094008 [arXiv:hep-ph/0312266].

[73] K. Melnikov and F. Petriello, *The W boson production cross section at the LHC through $O(\alpha(s)^2)$*, Phys. Rev. Lett. **96** (2006) 231803 [arXiv:hep-ph/0603182].

[74] K. Melnikov and F. Petriello, *Electroweak gauge boson production at hadron colliders through $O(\alpha(s)^2)$*, Phys. Rev. D **74** (2006) 114017 [arXiv:hep-ph/0609070].

[75] D. Binosi and L. Theussl, *JaxoDraw: A graphical user interface for drawing Feynman diagrams*, Comput. Phys. Commun. **161**, 76 (2004) [arXiv:hep-ph/0309015].

[76] D. Binosi, J. Collins, C. Kaufhold and L. Theussl, *JaxoDraw: A graphical user interface for drawing Feynman diagrams. Version 2.0 release notes*, arXiv:0811.4113 [hep-ph].

Acknowledgements

My special thanks go to Prof. Dr. Dieter Zeppenfeld, for giving me the opportunity to work on this interesting topic. I am particularly grateful for his advice, his interest in my work, and also for support in many respects.

I thank Prof. Dr. Johann H. Kühn for agreeing to be the second referee for my dissertation.

Throughout my time at the Institute for Theoretical Physics in Karlsruhe I have always enjoyed the friendly atmosphere. Many thanks to all colleagues.
In this context I want to especially thank my room mates, Gunnar Klämke and Manuel Bähr for the inspiring scientific as well as personal discussions throughout this thesis.

Special thanks go to Gunnar Klämke, Christoph Englert, Stefan Prestel, Christian Trück, and Heidi Rzehak for carefully reading parts of the manuscript.

I want to thank the Graduiertenkolleg "Hochenergiephysik und Teilchenastrophysik" for its financial support during the whole thesis.

Mein ganz besonderer Dank geht an meine Eltern und meine Schwiegereltern, die es mir durch ihre liebevolle Betreuung meines Sohnes ermöglicht haben guten Gewissens diese Arbeit zu schreiben. Außerdem konnte ich immer, wenn Not am Mann war auf Ihre Unterstützung zählen.

Als letzte und wichtigste Personen möchte ich meinem Mann Jörg und meinem Sohn Daniel danken, die mir in jeder Hinsicht eine wunderbare Hilfe waren und die im Laufe der Jahre manche Entbehrung haben hinnehmen müssen um mir diese Arbeit zu ermöglichen.